

University of Stuttgart
Germany

Ultrafast Nonlinear Plasmonics

From Dipole Nanoantennas to Hybrid Complex Plasmonic Structures

Von der Fakultät Mathematik und Physik der Universität Stuttgart
zur Erlangung der Würde eines Doktors der
Naturwissenschaften (Dr. rer. nat.) genehmigte Abhandlung

vorgelegt von
Bernd Metzger
aus Stuttgart

Hauptberichter: Prof. Dr. H. Giessen
Mitberichter: Prof. Dr. P. Michler
Vorsitzender: Prof. Dr. G. Wunner

Tag der mündlichen Prüfung: 6.11.2014

4. Physikalisches Institut der Universität Stuttgart

September 2014

Bernd Metzger: *Ultrafast Nonlinear Plasmonics:
From Dipole Nanoantennas to Hybrid Complex Plasmonic Structures*

I hereby certify that this dissertation is entirely my own work except where otherwise indicated. Passages and ideas from other sources have been clearly indicated.

Stuttgart, September 2014

Bernd Metzger

ABSTRACT

The aim of this thesis is to study and investigate the nonlinear optical response of complex plasmonic nanostructures under illumination with high intensity ultrashort laser pulses.

In order to perform nonlinear spectroscopy experiments we develop a new laser source for the generation of widely tunable ultrashort laser pulses. The experimental setup consists of a high-power Yb:KGW solitary mode-locked oscillator, of a nonlinear photonic crystal fiber for spectral broadening, of a prism sequence for pulse compression and a 4f Fourier transform pulse shaper for amplitude and phase modulation. This setup allows for the generation of Fourier-limited widely tunable sub-20 fs laser pulses and constitutes an ideal light source for the nonlinear optical experiments of plasmonic nanostructures.

In contrast to most previous studies of the nonlinear optical response of plasmonic nanostructures here we perform spectrally-resolved nonlinear optical spectroscopy, which means that we tune the fundamental narrow-band laser over a broad spectral range and are therefore able to measure the frequency-dependence of the nonlinear optical response of complex plasmonic nanostructure arrays.

In the nonlinear spectroscopy experiments we find that the spectral position of highest conversion efficiency for third harmonic generation in rod-type gold nanoantenna arrays is equivalent with the spectral peak position of the plasmonic near-field amplitude. The absolute conversion efficiency of nonlinear optical effects strongly depends on the linear optical response and the properties of the plasmonic modes. In particular, the resonance frequency, the linewidth and the absolute oscillator strength critically influence and determine the overall nonlinear optical response. By comparing measured linear and nonlinear spectra of complex coupled plasmonic nanostructure arrays to results of a

classical coupled oscillator model we find excellent agreement, which shows that the highly complex electrodynamic processes can even be understood in a classical intuitive fashion.

Furthermore, we investigate the enhancement of third harmonic generation in complex plasmonic nanostructure arrays, which exhibit plasmonic Fano resonances. The plasmonic Fano resonance is the result of the interference of a bright and a dark mode and due to the long lifetime of the latter it exhibits the potential to further enhance the conversion efficiency of nonlinear optical effects. In particular we find that a nonlinear near-field polarization which is generated in a dark mode does not radiate to the far-field due to destructive interference.

Beyond pure plasmonic nanostructures we study the enhancement of third harmonic generation in highly nonlinear indium tin oxide nanocrystals boosted by the intense electric near-field of plasmonic gap-antennas. When comparing corresponding hybrid and bare plasmonic gap-antenna arrays we find an enhancement in the third harmonic response by a about a factor of two. However, the origin of the higher third harmonic signal strength can be attributed to an enhanced plasmonic near-field and to the high optical nonlinearity of gold, rather than to the optical nonlinearity of the indium tin oxide.

Finally, we introduce a spectroscopic method for measuring the frequency-dependent second-order response using ultrabroadband strongly chirped laser pulses. The dispersion suppresses nonlinear frequency mixing, hence the second-order response of a material can be unambiguously retrieved. We demonstrate this method by measuring the frequency-dependent second harmonic response of the metals gold, aluminium, silver and copper in the wavelength range of about 900 to 1150 nm and compare the results to classical second harmonic spectroscopy. The second harmonic spectra indicate that interband transitions in the metals influence the overall nonlinear optical response.

ZUSAMMENFASSUNG

Das Ziel dieser Doktorarbeit ist das Studium und die Erforschung der nichtlinearen optischen Eigenschaften komplexer plasmonischer Nanostrukturen durch die Beleuchtung mit ultrakurzen Laserpulsen sehr hoher Lichtintensität.

Für die Experimente der nichtlinearen optischen Spektroskopie wurde eine neue Laserquelle entwickelt, welche es erlaubt weit durchstimmbare ultrakurze Laserpulse zu erzeugen. Dieses System besteht aus einem Hochleistungs-Yb:KGW-Lasersoszillator, einer nichtlinearen photonischen Kristallfaser für die spektrale Verbreiterung, einer Prismenstrecke zur Kompression der Laserpulse, sowie einem 4f Pulsformer, der die Modulation von Amplitude und Phase der Laserpulse ermöglicht. Mit dem Aufbau können weit durchstimmbare Fourier-limitierte sub-20 fs Laserpulse erzeugt werden, welche eine ideale Lichtquelle für die nichtlinearen spektroskopischen Experimente der plasmonischen Nanostrukturen darstellen.

Im Gegensatz zu den meisten vorherigen Untersuchungen werden in dieser Arbeit spektral aufgelöste Messungen der nichtlinearen optischen Eigenschaften von plasmonischen Nanostrukturen durchgeführt. Explizit bedeutet dies, dass ein schmalbandiger Laser über einen weiten Spektralbereich durchgestimmt wird und so die spektrale Abhängigkeit der nichtlinearen optischen Antwort der plasmonischen Nanostrukturen gemessen werden kann.

In den nichtlinearen spektroskopischen Experimenten an Nanoantennenfeldern, welche aus goldenen Dipolantennen bestehen, zeigt sich, dass die höchste Konversionseffizienz für die Erzeugung der dritten Harmonischen bei der spektralen Position zu finden ist, an der das plasmonische Nahfeld seinen höchsten Wert erreicht. Die absolute Konversionseffizienz von nichtlinearen optischen Effekten hängt stark von der linearen optischen

Antwort und den Eigenschaften der plasmonischen Moden ab. Insbesondere beeinflussen und bestimmen die spektrale Position der Resonanzfrequenz, die Linienbreite und die absolute Oszillatorstärke die nichtlineare optische Antwort. Bei dem Vergleich von gemessenen linearen und nichtlinearen Spektren von komplexen gekoppelten plasmonischen Nanostrukturen mit einem klassischen Modell von gekoppelten harmonischen Oszillatoren finden wir eine hervorragende Übereinstimmung. Diese Tatsache zeigt, dass die komplizierten elektrodynamischen Prozesse auf eine einfache und intuitive Weise verstanden und erklärt werden können.

Desweiteren untersuchen wir die Verstärkung der dritten Harmonischen in komplexen plasmonischen Nanostrukturen, die plasmonische Fano-Resonanzen aufweisen. Die Fano-Resonanz resultiert aus der Kopplung oder der Interferenz einer hellen und einer dunklen Mode und wegen der längeren Lebensdauer der Letzteren haben diese Nanostrukturen das Potential die Konversionseffizienz von nichtlinearen optischen Effekten weiter zu erhöhen. Insbesondere finden wir, dass eine nichtlineare Nahfeldpolarisation, die ihren Ursprung in der dunklen Mode hat, wegen destruktiver Interferenz nicht ins Fernfeld abstrahlen kann.

Darüber hinaus untersuchen wir die Verstärkung der Erzeugung der dritten Harmonischen in hoch nichtlinearen Indiumzinnoxidnanokristallen verstärkt durch das überhöhte elektrische Nahfeld von plasmonischen Nanogapantennen. Dabei finden wir eine Verstärkung der dritten Harmonischen um ungefähr einen Faktor von zwei, wenn wir entsprechende Hybrid-Nanoantennen mit reinen Gold-Nanoantennen vergleichen. Allerdings zeigt sich, dass der Ursprung des verstärkten dritten harmonischen Signals in einem erhöhten plasmonischen Nahfeld und in der hohen Nichtlinearität des Goldes selbst zu finden ist, und nicht von der Nichtlinearität der Indiumzinnoxidnanokristalle herrührt.

Zuletzt stellen wir eine spektroskopische Technik vor, welche es ermöglicht, die frequenzabhängige optische Antwort zweiter Ordnung zu messen, wobei ultrabreitbandige stark gechirp-te Laserpulse zum Einsatz kommen. Durch die Dispersion wird

die Summenfrequenzerzeugung unterdrückt, wodurch die nichtlineare Antwort zweiter Ordnung eines Materials eindeutig bestimmt werden kann. Wir demonstrieren diese Messmethode durch die Messung der frequenzabhängigen optischen Antwort zweiter Ordnung von den Metallen Gold, Aluminium, Silber und Kupfer im Wellenlängenbereich von 900 bis 1150 nm und vergleichen die Messergebnisse mit klassischer Spektroskopie der zweiten Harmonischen. Die Spektren der zweiten Harmonischen deuten darauf hin, dass Interbandübergänge in den Metallen einen Einfluss auf die nichtlineare optische Antwort haben.

PUBLICATIONS

Parts of this thesis have already been published:

In scientific journals:

- [1] B. METZGER, A. STEINMANN, F. HOOS, S. PRICKING, AND H. GIESSEN
“Compact laser source for high-power white light and widely tunable sub-65 fs laser pulses”
Opt. Lett **35**, 3961 (2010).
- [2] B. METZGER, A. STEINMANN, AND H. GIESSEN
“High power widely tunable sub-20 fs Gaussian laser pulses for ultrafast nonlinear spectroscopy”
Opt. Express **19**, 24354 (2011).
- [3] B. METZGER, M. HENTSCHEL, M. LIPPITZ, AND H. GIESSEN
“Third-harmonic spectroscopy and modeling of the nonlinear response of plasmonic nanoantennas”
Opt. Lett. **37**, 4741 (2012).
- [4] B. METZGER, T. SCHUMACHER, M. HENTSCHEL, M. LIPPITZ, AND H. GIESSEN
“Third Harmonic Mechanism in Complex Plasmonic Fano Structures”
ACS Photonics **6**, 471 (2014).
This article has been selected to be featured in ACS Editor’s Choice.
- [5] B. METZGER, M. HENTSCHEL, T. SCHUMACHER, M. LIPPITZ, X. YE, C. B. MURRAY, B. KNABE, K. BUSE, AND H. GIESSEN
“Doubling the efficiency of third harmonic generation by positioning ITO nanocrystals into the hot-spot of plasmonic gap-antennas”
Nano Lett. **14**, 2867 (2014).
- [6] B. METZGER, L. GUI, AND H. GIESSEN
“Ultrabroadband chirped pulse second harmonic spectroscopy: Measuring the frequency-dependent second-order response of different metal films”
Opt. Lett. **39**, 5293 (2014).

At international conferences:

Talks:

- [7] B. METZGER, F. HOOS, A. STEINMANN, AND H. GIESSEN
“Compact laser source for tunable sub 50 fs pulses with 44 Mhz repetition rate and several 10 mw of average power in the range of 900 nm to 1300 nm”

-
- Talk Q 6.2, Spring Meeting of the German Physical Society (DPG) 2010, Hannover (Germany).
- [8] B. METZGER, A. STEINMANN, G. ALBRECHT, AND H. GIESSEN
“Compact and tunable sub-20 fs laser source for ultrafast nonlinear applications”
Talk CF3.4, CLEO/Europe 2011, Munich (Germany).
- [9] B. METZGER, A. STEINMANN, M. HENTSCHEL, AND H. GIESSEN
“High-power widely tunable sub-20 fs Gaussian laser pulses and their application for nonlinear nano-plasmonic spectroscopy”
Talk Q 10.7, Spring Meeting of the German Physical Society (DPG) 2012, Stuttgart (Germany).
- [10] B. METZGER, M. HENTSCHEL, T. SCHUMACHER, AND H. GIESSEN
“Nonlinear optical response of complex plasmonic Fano structures”
Talk SAT3s.2, 4th International Topical Meeting on Nanophotonics and Metamaterials (Nanometa) 2013, Seefeld (Austria).
- [11] B. METZGER, M. HENTSCHEL, T. SCHUMACHER, AND H. GIESSEN
“Nonlinear optical response of complex plasmonic nanoantennas and Fano structures”
Talk O 7.5, Spring Meeting of the German Physical Society (DPG) 2013, Regensburg (Germany).
- [12] B. METZGER, M. HENTSCHEL, T. SCHUMACHER, M. LIPPITZ, AND H. GIESSEN
“Third harmonic spectroscopy of complex plasmonic Fano structures”
Talk II.2.1, CLEO/Europe 2013, Munich (Germany).
- [13] B. METZGER, M. HENTSCHEL, T. SCHUMACHER, M. LIPPITZ, AND H. GIESSEN
“Third harmonic spectroscopy of complex plasmonic Fano structures”
Talk QTh3E.2, CLEO/QELS 2013, San José (CA, USA).
- [14] B. METZGER, M. HENTSCHEL, T. SCHUMACHER, GELON ALBRECHT, M. LIPPITZ, AND H. GIESSEN
“Nonlinear optical spectroscopy of complex plasmonic nanoantennas”
3rd International Workshop on Ultrafast Nanooptics (UNO-3) 2013, Bad Dürkheim (Germany).
- [15] B. METZGER, M. HENTSCHEL, T. SCHUMACHER, M. LIPPITZ, AND H. GIESSEN
“Nonlinear Plasmonics”
4th Molecular Materials Meeting (M3), January 2014, Biopolis, Singapore.
- [16] B. METZGER, M. HENTSCHEL, T. SCHUMACHER, M. LIPPITZ, X. YÉ, C. B. MURRAY, B. KNABE, K. BUSE, AND H. GIESSEN
“Tailoring the third harmonic response of plasmonic nanoantennas by incorporation of dielectric nanocrystals”
Talk O 46.7, Spring Meeting of the German Physical Society (DPG) 2014, Dresden (Germany).
- [17] B. METZGER, M. HENTSCHEL, T. SCHUMACHER, M. LIPPITZ, X. YÉ, C. B. MURRAY, B. KNABE, K. BUSE, AND H. GIESSEN

“Doubling the efficiency of third harmonic generation by positioning ITO and LiNbO₃ nanocrystals into the hot-spot of plasmonic gap-antennas”
8th International Congress on Advanced Electromagnetic Materials in Microwaves and Optics, Metamaterials 2014, Copenhagen (Denmark).

Poster:

- [18] B. METZGER, A. STEINMANN, F. HOOS, S. PRICKING, AND H. GIESSEN
“Compact and widely tunable sub-50 fs laser source with 30 mW to 300 mW output power at 44 MHz repetition rate for nonlinear spectroscopy applications”
Poster ME22, 17th International Conference on Ultrafast Phenomena 2010, Snomass (CO, USA).
- [19] B. METZGER, M. HENTSCHEL, AND H. GIESSEN
“Second and third harmonic spectroscopy of complex plasmonic nanoantennas”
Poster, 12th International Conference on Near-Field Optics, Nanophotonics and Related Techniques 2012, San Sebastian (Spain).
- [20] B. METZGER, M. HENTSCHEL, T. SCHUMACHER, M. LIPPITZ, AND H. GIESSEN
“Third harmonic spectroscopy of complex plasmonic nanostructures”
Poster Tu-28-P-83, 6th International Conference on Surface Plasmon Photonics 2013, Ottawa (Canada).

Book Chapters:

- [21] B. METZGER, A. STEINMANN, F. HOOS, S. PRICKING, AND H. GIESSEN
“Compact and widely tunable sub-65 fs laser source with 13 mW to 330 mW output power at 44 MHz repetition rate for nonlinear spectroscopy applications”
Proceedings of the 17th International Conference on Ultrafast Phenomena, Oxford University Press (2011).
- [22] M. HENTSCHEL, T. UTIKAL, B. METZGER, H. GIESSEN, AND M. LIPPITZ
“Nonlinear Plasmon Optics”
2nd International Workshop on Nonlinear Nanostructures for Ultrafast Laser Applications, edited by Rüdiger Grunwald, Springer (201x).

Other scientific contributions which are not part of this thesis:

- [23] J.-P. NEGEL, R. HEGENBARTH, A. STEINMANN, B. METZGER, F. HOOS, AND H. GIESSEN
“Compact and cost-effective scheme for THz generation via optical rectification in GaP and GaAs using novel fs laser oscillators”
Appl. Phys. B **103**, 45 (2011).
- [24] M. HENTSCHEL, M. SCHÄFERLING, B. METZGER, AND H. GIESSEN
“Plasmonic Diastereomers: Adding up chiral centers”
Nano Lett. **13**, 600 (2013).
- [25] X. YIN, M. SCHÄFERLING, B. METZGER, AND H. GIESSEN
“Interpreting chiral spectra: The plasmonic Born-Kuhn model”
Nano Lett. **13**, 6238 (2013).

CONTENTS

1	INTRODUCTION	1
2	ELECTRODYNAMICS, NANOPLASMONICS, AND NON-LINEAR OPTICS	5
2.1	Basics of Electrodynamics	5
2.1.1	Maxwells Equations	5
2.1.2	The Lorentz Oscillator Model	10
2.1.3	The Drude Model and the Optical Properties of Metals	13
2.2	Nanooptics and Plasmonics	16
2.2.1	Optical Properties of Metal Nanoparticles	17
2.2.2	Complex Plasmonic Nanostructure Arrays and Their Fabrication	24
2.3	Nonlinear Optics	27
2.3.1	Nonlinear Polarization and Nonlinear Susceptibility	27
2.3.2	Nonlinear Optical Processes of Second Order	30
2.3.3	Nonlinear Optical Processes of Third Order and the Nonlinear Refractive Index	32
2.3.4	The Anharmonic Oscillator Model	36
3	ULTRASHORT LASER PULSES: FUNDAMENTAL PRINCIPLES AND EXPERIMENTAL REALIZATION	41
3.1	Yb:KGW Laser Oscillator	43
3.2	Linear and Nonlinear Fiber Optics	45
3.2.1	Tapered Fibers and Photonic Crystal Fibers	46
3.2.2	Supercontinuum Generation in Nonlinear Optical Fibers	48
3.3	Pulse Compression	52
3.3.1	Generation of Widely Tunable Sub-65 fs Laser Pulses	53

3.3.2	Pulse Stability and Recompressibility after Spectral Broadening in the Normal and the Anomalous Dispersion Regime	57
3.3.3	Nonlinear Pulse Compression with a Large Mode Area Photonic Crystal Fiber	61
3.4	Fourier Transform Pulse Shaping	63
3.4.1	Liquid Crystal Spatial Light Modulation	65
3.4.2	The Complete Experimental Pulse Shaper Setup and its Theoretical Limits	68
3.4.3	The Multiphoton Intrapulse Interference Phase Scan	71
3.4.4	Amplitude Shaping and Pulse Shaper Assisted Interferometric Frequency Resolved Optical Gating	74
3.4.5	Widely Tunable sub-20 fs Laser Pulses	76
4	NONLINEAR PLASMONICS	79
4.1	Plasmonic Nanoantenna Arrays	81
4.1.1	Linear, Second and Third Harmonic Response of Plasmonic Nanoantenna Arrays	81
4.1.2	Third Harmonic Spectroscopy of Plasmonic Nanoantenna Arrays	85
4.1.3	Linewidth, Resonance Position and Their Influence on the Effective Plasmonic Near-Field Enhancement	90
4.2	Two Coupled Plasmonic Oscillators	93
4.2.1	Linear Optical Response of Coupled Plasmonic Oscillators	94
4.2.2	Third Harmonic Spectroscopy and Modeling of the Third Order Susceptibility Tensor of Coupled Plasmonic Oscillators	102
4.3	Complex Plasmonic Fano Structures	111
4.3.1	Third Harmonic Mechanism in Dolmen-Type Complex Plasmonic Fano Structures	112
4.3.2	The Complex Coupling Coefficient in Coupled Plasmonic Systems	124

4.4	ITO Nanocrystal-Incorporated Plasmonic Gap-Antennas	128
4.5	Ultrabroadband Chirped Pulse Second Harmonic Spectroscopy	143
4.5.1	Measuring the Frequency-Dependent Second-Order Response of Different Metal Films . .	149
5	CONCLUSION AND OUTLOOK	153
A	APPENDIX	157
	BIBLIOGRAPHY	165
	Acknowledgements	187
	Curriculum Vitae	191

INTRODUCTION

Physics gets highly exciting when it comes to resonance phenomena. In mechanical systems the term “resonance” typically describes the enhanced oscillatory motion of an object, which is driven by an external force at its resonance- or eigenfrequency. For small damping this is the frequency at which the system oscillates without any external stimuli. However, resonances not only appear in mechanical systems but form in a plethora of natural and artificial environments.

Prominent examples of mechanical resonances are the bursting crystal wine glass, when it is exposed to acoustic sound waves of the right frequency, or the strongly oscillating bridge due to the periodic movement of people. Furthermore, in the human ear acoustic waves excite vibrations in auditory hair cells, which exhibit various resonance frequencies, and hence allow for separating tones [1]. More technically, resonances in the oscillations of electrical currents in integrated circuits between capacitive and inductive elements are the basis for modern electrical engineering [2]. In atomic physics resonances occur in the absorption of light if the frequency or the energy of an exciting photon matches an electronic transition [3]. Similarly, vibrations can be resonantly excited by light between the bound atoms of a molecule [4]. Beyond that, resonances even appear in our solar system for example in stationary points (Lagrangian points) of the gravitational potential of two heavy luminaries [5].

The key for understanding most resonance phenomena is the classical harmonic oscillator model system, which is nowadays

taught in the first semester in studies of natural science, or even on a basic level already at school, and it is probably also one of the most important topics in physics.

In this thesis we also study resonance phenomena, which can be observed in small metal nanoparticles. Light, which impinges on metal nanoparticles can excite collective harmonic oscillations of the conduction electrons and the emerging resonances of these oscillations are termed *localized surface plasmon resonances* [6–9]. The plasmonic oscillations mostly take place at the interface of a metal nanoparticle, and they can lead to an intense electric field enhancement in the near-surrounding and to an exceptional high electric polarization in metal nanoparticles [10–13]. Associated to this field enhancement is a strong localization of far-field radiation to the dimensions of the nanoparticles, which typically exhibit nanometer length scale. Therefore, these systems allow for confining visible and near infrared light to sub-wavelength volumes [14]. Nowadays, modern nano-fabrication technology enables the design of nanoparticles or nanostructures with pre-defined geometry and shape, and hence, allow for tailoring the optical response of a nanostructured system.

Furthermore, until the year 1960 the classical movement of bound valence electrons in matter caused by the electric field of propagating light almost perfectly corresponded to a harmonic oscillation. To that date so high electric field strength, which make electrons “feel” that they are not confined to a perfect harmonic potential, were simply not available. Then, in the year 1960 the invention of the laser by T. H. Maiman changed everything [15]. The laser suddenly delivered the necessary electric fields, which led to the breakdown of the harmonic approximation and allowed for exciting anharmonic oscillations of electrons in matter. The consequences of these nonlinear oscillations opened a total new field of research, which is the field of “*Nonlinear Optics*” [16, 17].

The strong electric fields make photons to effectively interact within matter beyond simple linear interference. As an example, in the nonlinear optical effect second harmonic generation two photons at frequency ω are "combined" and upconverted to one photon with twice the energy at frequency 2ω [18]. Beyond the interaction of two photons in nonlinear optics the interplay of arbitrary numbers of equal or different photons is possible, which leads to a variety of new effects like sum frequency generation, difference frequency generation, optical rectification or four wave mixing, to only name a few.

Just after the first continuous wave laser sources, the invention of pulsed lasers paved the way to even higher intensities of optical electric fields. Until today ultrashort laser pulses can exhibit pulse durations on the order of femtoseconds (10^{-15} s) [19, 20] and even attosecond (10^{-18} s) pulse durations are possible [21, 22]. The ultrashort time scale of these events allowed to study and observe processes, which occur on similar short timescales, like the formation of molecules [23]. More or less a side effect of the ultrashort pulse duration is that the entire optical energy is focused to an ultrashort event in time and therefore these short laser pulses exhibit enormous peak intensities, which further boost the efficiency in nonlinear optical effects.

In this thesis we combine the ability of metal nanoparticles to confine and focus light to deep sub-wavelength volumes in space with ultrashort laser pulses, which concentrate all their energy to a tiny "space" in time. Together, these two systems pave the way to extremely high conversion efficiencies in nanoscale volumes of nonlinear optical effects.

The aim of this thesis is to understand and describe the microscopic processes responsible for nonlinear optical effects in plasmonics nanostructures and to design and engineer complex and hybrid nanostructure systems for the further enhancement of nanoscale nonlinearities.

In the first chapter we give a basic introduction to the optical properties of metal nanoparticles. Furthermore, we introduce the complex plasmonic nanostructure arrays, which are investigated in this thesis and outline the fundamental concepts of *Nonlinear Optics*.

The second chapter focuses on the generation of widely tunable ultrashort laser pulses. For this thesis an entire novel laser setup has been built up from the scratch and is introduced in detail.

Finally, the third and main chapter handles nonlinear spectroscopy of various complex and hybrid plasmonic nanostructure arrays.

ELECTRODYNAMICS, NANOPLASMONICS, AND NONLINEAR OPTICS

2.1 BASICS OF ELECTRODYNAMICS

In order to understand and describe the optical properties of plasmonic nanostructures it is essential to first introduce a few fundamental concepts and physical quantities. Since the optical processes in these nanostructures can be described with electrodynamics we start with Maxwells equations in matter, and subsequently derive a microscopic phenomenological model, the Lorentz oscillator model, for the dielectric susceptibility and the complex refractive index. We furthermore introduce the Drude model, which allows to describe and understand the fundamental optical properties of bulk metals.

2.1.1 *Maxwells Equations*

The key to all electrodynamic phenomena are the macroscopic Maxwell equations in matter [6]:

- Gauss's law

$$\operatorname{div} \mathbf{D} = \rho_{\text{ext}} \quad (2.1)$$

- Gauss's law for magnetism

$$\operatorname{div} \mathbf{B} = 0 \quad (2.2)$$

- Faraday's law of induction

$$\operatorname{rot} \mathbf{E} = -\frac{\partial \mathbf{B}}{\partial t} \quad (2.3)$$

- Ampère's law

$$\operatorname{rot} \mathbf{H} = \mathbf{j}_{\text{ext}} + \frac{\partial \mathbf{D}}{\partial t} \quad (2.4)$$

The vector fields \mathbf{E} , \mathbf{D} , \mathbf{H} and \mathbf{B} are the electric field \mathbf{E} , the electric displacement field \mathbf{D} , the magnetic field \mathbf{H} and the magnetic flux density \mathbf{B} , respectively. The sources of these fields are the external charge density ρ_{ext} and the external current density \mathbf{j}_{ext} .

In matter the constitutive equations relate the electrodynamic fields to the polarization \mathbf{P} and the magnetization \mathbf{M} of the medium [6]:

$$\mathbf{D} = \epsilon_0 \mathbf{E} + \mathbf{P} \quad (2.5)$$

$$\mathbf{B} = \mu_0 (\mathbf{H} + \mathbf{M}) \quad (2.6)$$

where

ϵ_0 is the electric permittivity of free space and
 μ_0 is the magnetic permeability of free space

When we insert the constitutive equations (2.5, 2.6) into Gauss's law (2.1) and Ampère's law (2.4), we obtain equivalent equations containing only the electric field \mathbf{E} and the magnetic flux density \mathbf{B} , which are also valid microscopically:

$$\operatorname{div} \mathbf{E} = \frac{1}{\epsilon_0} (\rho_{\text{ext}} - \underbrace{\operatorname{div} \mathbf{P}}_{\rho_{\text{int}}}) = \frac{1}{\epsilon_0} \rho_{\text{tot}} \quad (2.7)$$

$$\operatorname{rot} \mathbf{B} - \frac{1}{c^2} \frac{\partial \mathbf{E}}{\partial t} = \mu_0 (\mathbf{j}_{\text{ext}} + \underbrace{\frac{\partial \mathbf{P}}{\partial t} + \operatorname{rot} \mathbf{M}}_{\mathbf{j}_{\text{int}}}) = \mu_0 \mathbf{j}_{\text{tot}} \quad (2.8)$$

where we defined the total charge density $\rho_{\text{tot}} = \rho_{\text{int}} + \rho_{\text{ext}}$ and the total current density $\mathbf{j}_{\text{tot}} = \mathbf{j}_{\text{int}} + \mathbf{j}_{\text{ext}}$ and introduced the speed

of light $c = 1/\sqrt{\mu_0\epsilon_0}$ in free space. Furthermore, from Ampère's law (2.8) it is possible to derive a continuity equation for the total charge and the total current density,

$$\operatorname{div} \mathbf{j}_{\text{tot}} = -\frac{\partial \rho_{\text{tot}}}{\partial t} \quad (2.9)$$

which is in that form also separately valid for the internal and external charges and currents.

Since we restrict ourselves to dielectric or metallic but nonmagnetic materials, the magnetization \mathbf{M} can be neglected and is set equal to zero. In the following a wave equation for the electric field \mathbf{E} in matter is derived. We assume that all external sources, which generate primary, e.g. the incoming electrodynamic fields, are very far apart and located outside our considered spatial domain. Hence, the external charge density ρ_{ext} and the external current density \mathbf{j}_{ext} are in that case zero. To derive the wave equation a rotation is applied on Faraday's law of induction (2.3) and together with Gauss's (2.1) and Ampère's law (2.4) and the two constitutive equations (2.5, 2.6) we arrive at:

$$\Delta \mathbf{E}(\mathbf{r}, t) - \frac{1}{c^2} \frac{\partial^2 \mathbf{E}(\mathbf{r}, t)}{\partial t^2} = \mu_0 \frac{\partial^2 \mathbf{P}(\mathbf{r}, t)}{\partial t^2} \quad (2.10)$$

The left side of equation (2.10) corresponds to the free space wave equation for the electric field \mathbf{E} , while the right side describes the interaction of the electric field wave with the medium and its polarization \mathbf{P} .

So far, the above derivation of the wave equation (2.10) in matter was carried out in the spatial and the temporal domain. For the following considerations it is more convenient to switch to a frequency domain description. Hence, we define the Fourier-

Transform between the temporal and the frequency domain for the electric field \mathbf{E} as [17]:

$$\mathbf{E}(\mathbf{r}, \omega) = \int_{-\infty}^{\infty} \mathbf{E}(\mathbf{r}, t) e^{i\omega t} dt \quad (2.11)$$

$$\mathbf{E}(\mathbf{r}, t) = \frac{1}{2\pi} \int_{-\infty}^{\infty} \mathbf{E}(\mathbf{r}, \omega) e^{-i\omega t} d\omega \quad (2.12)$$

The Fourier-Transform of equation (2.10) can readily be carried out, since a temporal derivative yields in the frequency domain a factor $-i\omega$ [24]. Therefore, we obtain the wave equation in matter in the frequency domain:

$$\Delta \mathbf{E}(\mathbf{r}, \omega) + \frac{\omega^2}{c^2} \mathbf{E}(\mathbf{r}, \omega) = -\mu_0 \omega^2 \mathbf{P}(\mathbf{r}, \omega) \quad (2.13)$$

The polarization \mathbf{P} in the medium is a function of the electric field \mathbf{E} . Hence, it is possible to write the polarization \mathbf{P} as a power series of the electric field \mathbf{E} [16, 17]. When the electric field amplitude is low, the term linear in \mathbf{E} is dominating, and all higher order contributions can be neglected. For increasing field amplitude, the terms quadratic, cubic, or even of higher order in \mathbf{E} can get highly important, which lead to a plethora of new phenomena. These phenomena belong to the field of *Nonlinear Optics* [16], which will be introduced in section 2.3. For the moment we restrict ourselves to low electric fields \mathbf{E} , hence

$$\mathbf{P}(\mathbf{r}, \omega) = \epsilon_0 \chi^{(1)}(\omega) \mathbf{E}(\mathbf{r}, \omega) \quad (2.14)$$

where $\chi^{(1)}(\omega)$ is the first order electric susceptibility. For anisotropic materials the polarization and propagation direction of the electric field through the medium matters and the electric susceptibility must then be written as a tensor of second order: $P_i = \epsilon_0 \chi_{ij} E_j$. For isotropic materials we can neglect the tensorial character of the susceptibility and consider it as a scalar function

of the angular frequency ω . When inserting equation (2.14) into the wave equation (2.13) we obtain the Helmholtz equation [17],

$$\Delta \mathbf{E}(\mathbf{r}, \omega) + \underbrace{(1 + \chi^{(1)}(\omega))}_{\epsilon_r(\omega)} \frac{\omega^2}{c^2} \mathbf{E}(\mathbf{r}, \omega) = 0 \quad (2.15)$$

where we defined the dielectric constant $\epsilon_r(\omega) = 1 + \chi^{(1)}(\omega)$. The Helmholtz equation (2.15) in matter in the case of a linear response is of the same form like the wave equation in free space, in particular when the dielectric constant is written together with the propagation velocity in the denominator. Hence, the complex propagation velocity of the wave in matter calculates to $v_m = c/\tilde{n}(\omega)$, with the complex refractive index $\tilde{n}(\omega)^2 = \epsilon_r(\omega) = 1 + \chi^{(1)}(\omega)$. When investigating the linear optical properties of a medium, the goal is to determine either the frequency-dependent complex refractive index $\tilde{n}(\omega)$ or equivalently the complex dielectric constant $\epsilon_r(\omega)$.

It is noteworthy that the dielectric constant $\epsilon_r(\omega)$ is related to the conductivity $\sigma(\omega)$ of a material, which is defined by Ohm's law [6]:

$$\mathbf{j}_{\text{int}}(\mathbf{r}, \omega) = \sigma(\omega) \mathbf{E}(\mathbf{r}, \omega) \quad (2.16)$$

Here, \mathbf{j}_{int} is the above introduced internal current density in the medium. Together with the continuity equation ($\text{div } \mathbf{j}_{\text{int}} = -\dot{\rho}_{\text{int}}$) for the internal current density \mathbf{j}_{int} and the internal charge density ρ_{int} it is straightforward to show that [6]:

$$\epsilon_r(\omega) = 1 + \frac{i}{\epsilon_0 \omega} \sigma(\omega) \quad (2.17)$$

Hence, the real part of the dielectric constant $\epsilon_r(\omega)$ is linked to the imaginary part of the conductivity $\sigma(\omega)$ and vice versa.

2.1.2 The Lorentz Oscillator Model

As mentioned before, either the electric susceptibility $\chi^{(1)}(\omega)$, the dielectric constant $\epsilon(\omega)$, or the complex refractive index $\tilde{n}(\omega)$ describe the linear optical properties of a medium. We now would like to introduce a microscopic model for the above mentioned quantities, the *Lorentz oscillator model*.

When an electromagnetic wave propagates through a dielectric medium its electric field forces the bound electrons to oscillate in a periodic fashion. For low energies this mainly affects the valence electrons, which we hence consider in the following. However the model can be easily extended to electrons located in lower bands. For low light intensities, the electrons can be regarded as bound in a harmonic potential. Therefore, the electromagnetic wave excites the electrons to harmonic oscillations. We can write the equation of motion for one electron as:

$$\ddot{\mathbf{x}}(t) + 2\gamma\dot{\mathbf{x}}(t) + \omega_0^2\mathbf{x}(t) = -\frac{e}{m_e}\mathbf{E}(t) \quad (2.18)$$

where

- $\mathbf{x}(t)$ displacement of the electron
- γ damping constant
- ω_0 resonance frequency
- e elementary charge
- m_e mass of an electron
- $\mathbf{E}(t)$ electric field

The displacement of an electron $\mathbf{x}(t)$ is oriented along the polarization direction of the driving electric field wave. The damping constant γ is introduced as a phenomenological parameter and has to be determined from the experiment or from quantummechanical considerations. In quantum mechanics it is related to the dipole matrix element between two states and is inversely proportional to the lifetime of the excited state [25]. Furthermore the resonance frequency ω_0 corresponds to the energy difference

$\Delta E = \hbar\omega_0$ of both quantum states. The solution of the differential equation (2.18) can be obtained in the frequency domain:

$$\mathbf{x}(\omega) = \frac{e}{m_e} \frac{1}{\omega^2 - \omega_0^2 + 2i\gamma\omega} \mathbf{E}(\omega) \quad (2.19)$$

The displacement of an electron $\mathbf{x}(\omega)$ from its equilibrium position leads to an electric dipole moment $\mathbf{p} = -e\mathbf{x}$ [26]. When the dipole moments in a dielectric can be considered as independent and are aligned in the same direction this leads to a cumulative polarization $\mathbf{P} = n_A \mathbf{p} = -en_A \mathbf{x}$, where n_A is the number density of atoms, assuming that only one electron per atom contributes to the dipole moment \mathbf{p} . Finally, we relate the polarization \mathbf{P} such as introduced in equation (2.14) to the electric field \mathbf{E} . Hence, we obtain for the electric susceptibility $\chi^{(1)}(\omega)$ [2]:

$$\chi^{(1)}(\omega) = -\frac{e^2 n_A}{\epsilon_0 m_e} \frac{1}{\omega^2 - \omega_0^2 + 2i\gamma\omega} \quad (2.20)$$

As mentioned in the previous chapter the electric susceptibility $\chi^{(1)}(\omega)$ is related to the dielectric constant $\epsilon(\omega)$ and to the complex refractive index $\tilde{n}(\omega)$ as:

$$\tilde{n}(\omega) = n + i\kappa \quad (2.21)$$

$$= \sqrt{\epsilon_r(\omega)} = \sqrt{1 + \chi^{(1)}(\omega)} \quad (2.22)$$

$$\approx 1 + \frac{1}{2}\chi^{(1)}(\omega) \quad (2.23)$$

where we introduced the real part $n(\omega)$ and the imaginary part $\kappa(\omega)$ of the complex refractive index. After the last approximately sign we did a Taylor expansion of the square root, which is actually only valid for $\chi^{(1)}(\omega) \ll 1$ and thus for optically dilute media [17]. The real and the imaginary part of the refractive index calculate to [2]:

$$n(\omega) = 1 - \frac{1}{2} \frac{e^2 n_A}{\epsilon_0 m_e} \frac{\omega^2 - \omega_0^2}{(\omega^2 - \omega_0^2)^2 + 4\gamma^2 \omega^2} \quad (2.24)$$

$$\kappa(\omega) = \frac{e^2 n_A}{\epsilon_0 m_e} \frac{\gamma\omega}{(\omega^2 - \omega_0^2)^2 + 4\gamma^2 \omega^2} \quad (2.25)$$

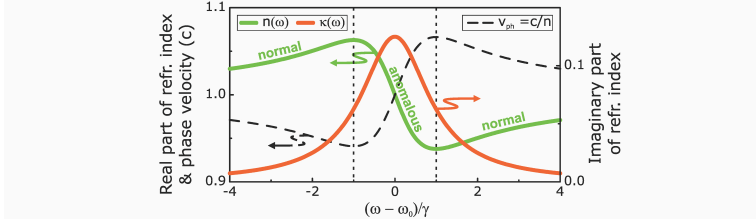


Figure 2.1: Real and imaginary part of the complex index of refraction $\tilde{n} = n + i\kappa$ as well as the phase velocity close to a resonance in the Lorentz oscillator model.

We can easily understand the meaning of the real and the imaginary part of the refractive index, if we consider a plane wave in a medium, propagating in z -direction, with wave vector $\mathbf{k}(\omega) = \tilde{n}(\omega) \cdot (\omega/c)\mathbf{e}_z$:

$$E(z) = E_0 e^{i\mathbf{k}\mathbf{r}} = E_0 e^{-\kappa \frac{\omega}{c} z} e^{i \frac{\omega}{c/n} z} \quad (2.26)$$

The real part of the refractive index $n(\omega)$ leads to a change in the phase velocity $v = c/n$, with which the electric field propagates through the medium. Due to the frequency dependence of the refractive index, the phase velocity v depends on frequency ω (dispersion). The imaginary part $\kappa(\omega)$ leads to attenuation of the amplitude of the propagating electric field by absorption. Both, the real and the imaginary part of the refractive index and the resulting phase velocity v are shown together in Fig. 2.1 in the vicinity of a resonance of the medium. Considering first the imaginary part $\kappa(\omega)$, we can see that the resonance leads to a peak in absorption close to the resonance frequency ω_0 . Furthermore, the width of the resonance is given by the damping constant γ . Secondly, the real part $n(\omega)$ at first increases monotonically when approaching the resonance, within the resonance it decreases and falls below one, after the resonance it increases again. Hence, outside the resonance the phase velocity v decreases with increasing frequency. This is the regime of normal dispersion, meaning that lower frequencies travel at higher velocities than higher frequencies. Within the resonance it is the other

way round, higher frequencies are faster than lower frequencies, which is the regime of anomalous dispersion.

At last we mention, that the imaginary part $\kappa(\omega)$ of the refractive index is related to the extinction coefficient $\alpha(\omega)$ of Lambert-Beer's law, which describes the attenuation of the intensity $I(z) = I_0 e^{-\alpha(\omega)z}$ of a plane wave with initial intensity I_0 when propagating in an medium [17]:

$$\alpha(\omega) = 2\frac{\omega}{c}\kappa(\omega) \approx \frac{\omega}{c} \operatorname{Im} \left[\chi^{(1)}(\omega) \right] \quad (2.27)$$

2.1.3 The Drude Model and the Optical Properties of Metals

In dielectrics and non-conducting materials the electrons are more or less bound to their atoms and are not able to move freely in the bulk material. This circumstance is caused by the fact that two electrons, which are Fermions, cannot occupy one quantum state with all quantum numbers identical [25] and furthermore, the bands, which form in solids, are in non-conducting materials completely filled. The valence electrons in dielectrics or semiconductors therefore have to acquire the energy difference between the valence band and the next higher lying unoccupied band to move in the material.

In contrast, in metals the conduction electrons are located in bands, which are only partly occupied. Hence, these electrons can jump between different quantum states in the band and move freely in the metal [2]. In gold for example, one electron from every atom is located in the sp-conduction band [27], which leads to its excellent conductivity.

Therefore, we treat the conduction electrons in a basic microscopic model of metals as individual freely moving electrons. It is called the *free electron model* or the *Drude model* of metals. Of course, the conduction electrons are not perfectly free in a metal

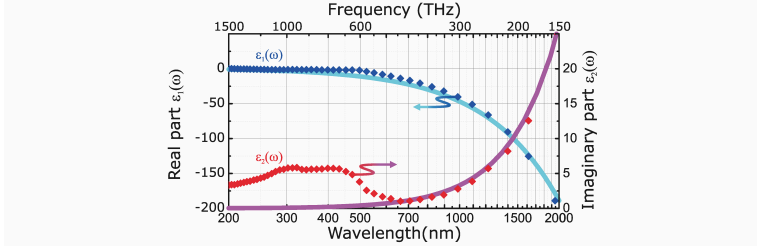


Figure 2.2: Measured values of the real and the imaginary part of the dielectric constant of gold (Johnson and Christy (1972) [28]). The solid lines correspond to a Drude model fit ($\omega_p = 2\pi \cdot 2077$ THz ($\lambda_p \sim 145$ nm), $\gamma_D = 2\pi \cdot 20.72$ THz ($\lambda_D \sim 14.5$ μm)).

and different scattering events, like scattering at lattice defects, electron-electron scattering or electron-phonon scattering, lead to an effective damping of the freely moving electrons. To account for these scattering events we introduce a phenomenological Drude damping parameter γ_D . The differential equation describing the movement of a free electron under the influence of an external electric field is formally identical to the differential equation of the Lorentz oscillator model (2.18) with the resonance frequency ω_0 being zero, since no restoring forces act on the conduction electrons:

$$\ddot{\mathbf{x}}(t) + \gamma_D \dot{\mathbf{x}}(t) = -\frac{e}{m_e} \mathbf{E}(t) \quad (2.28)$$

From the differential equation we obtain in analogy to the Lorentz oscillator model the electric susceptibility of the Drude model:

$$\chi(\omega) = -\underbrace{\frac{e^2 n_e}{\epsilon_0 m_e}}_{\omega_p^2} \frac{1}{\omega(\omega + i\gamma_D)} \quad (2.29)$$

In contrast to the Lorentz Oscillator Model the number density n_e here corresponds to the electron density in the metal, which can differ from the number density of atoms n_A , if on average more or less than one electron per atom contributes to the con-

ductivity. Furthermore, we introduced the bulk metal plasma frequency ω_p :

$$\omega_p = \sqrt{\frac{e^2 n_e}{\epsilon_0 m_e}} \quad (2.30)$$

In the next step we calculate the dielectric constant $\epsilon(\omega)$ in the Drude model and divide it into real part $\epsilon_1(\omega)$ and imaginary part $\epsilon_2(\omega)$:

$$\epsilon(\omega) = \epsilon_1(\omega) + i\epsilon_2(\omega) \quad (2.31)$$

$$= 1 - \omega_p^2 \frac{1}{\omega^2 + \gamma_D^2} + i \frac{\gamma_D \omega_p^2}{\omega(\omega^2 + \gamma_D^2)} \quad (2.32)$$

Despite the simplicity of the Drude model it describes the optical properties of metals in particular in the near infrared up to the visible part of the spectrum very well. In Fig. 2.2 measured data of the real and the imaginary part of the dielectric constant of gold are shown (Johnson and Christy (1972) [28]) together with a Drude model fit. The plasma frequency ω_p and the Drude damping constant γ_D extracted from the fit of the measured values for gold are $\omega_p = 2\pi \cdot 2077 \text{ THz}$ ($\lambda_p \sim 145 \text{ nm}$) and $\gamma_D = 2\pi \cdot 20.72 \text{ THz}$ ($\lambda_D \sim 14.5 \mu\text{m}$), respectively.

However, in particular the imaginary part $\epsilon_2(\omega)$ of the measured values for gold differ from the Drude model significantly in the visible and the ultraviolet (UV). In the Drude model the imaginary part $\epsilon_2(\omega)$ should converge for increasing frequency to zero since the scattering events caused by the Drude damping γ_D occur on a much longer timescale. In contrast, the measured values of $\epsilon_2(\omega)$ for gold show an increase towards higher frequencies, which occurs for gold at a wavelength of around 550 nm. The origin of this effect is that for large enough photon energies electrons from the inner lying d-band can be excited into the conduction band above the Fermi energy E_F [29].

Based on the Drude model for the dielectric constant it is also possible to understand the high reflectivity of metals. In the visible part of the spectrum the frequency ω is much larger when

compared to the Drude damping constant γ_D . Hence, the real part of the dielectric constant can be approximated to $\epsilon_1(\omega) \sim 1 - \omega_p^2/\omega^2$ and neglecting interband contributions the imaginary part $\epsilon_2(\omega)$ gets very small. Since in the visible regime the frequency ω is still smaller than the plasma frequency ω_p of the metal the real part of the dielectric constant $\epsilon_1(\omega)$ is negative. Therefore the complex refractive index $\tilde{n}(\omega) \sim \sqrt{\epsilon_1(\omega)}$ gets purely imaginary, meaning that no wave propagation but only evanescent waves are in the medium aloud. Therefore, a plane wave gets fully reflected at the interface of the metal.

Finally, for extreme UV frequencies when the frequency ω is larger than the plasma frequency ω_p metals turn into dielectrics [6], since here the real part of the dielectric constant is rendered positive. However, due to the above mentioned interband absorption electromagnetic waves propagating at extreme UV frequencies can get strongly damped and attenuated inside metals [6].

2.2 NANOOPTICS AND PLASMONICS

After the introduction to the optics of bulk metals in the last paragraph, we now turn to the optical properties of metal nanoparticles. When metal nanoparticles, which are on the size of about 10 nm to about several 100 nm, are illuminated with light in the visible or the near infrared, harmonic oscillations of the conduction electrons in the metal nanoparticles can be excited. These excitations are strongly related and similar to the oscillations of the conduction electrons in radio wave antennas, when these are illuminated by electrodynamic radiation in the radio wave regime. Since the conduction electrons in metals can be regarded as free electrons, like the electrons and ions in a plasma, the modes associated to these oscillations in the metal nanoparticles are often called "*localized surface plasmon resonances*" (LSPR) [6] and in general the term "*Plasmonics*" refers to the optics of metal nanoparticles. When localized plasmon oscillations are resonantly excited

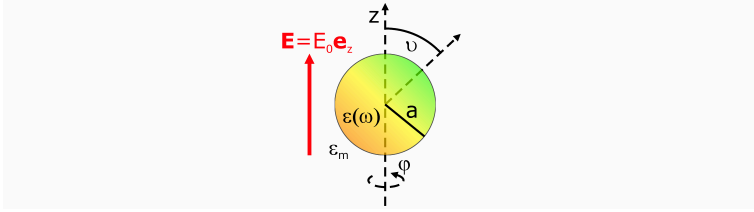


Figure 2.3: Schematic illustration of a metal nanoparticle with dielectric constant $\epsilon(\omega)$, embedded in a homogeneous medium with dielectric constant ϵ_m , and exposed to an external electric field \mathbf{E} oriented along the z -direction.

very high electric field strength and material polarizations can be obtained inside and in the near surrounding of the metal nanoparticles [6, 30]. The resonance frequency of a localized surface plasmon oscillation crucially depends on several properties of the metal nanoparticles: the size, the shape and the kind of metal of the nanoparticle [31]. Furthermore, the material in the surrounding of a nanoparticle strongly influences its resonance position.

In the following section we will show and discuss on a fundamental level, where these resonances are originating from. Furthermore, we will briefly introduce the samples, which are investigated in this thesis, and describe their fabrication method.

2.2.1 *Optical Properties of Metal Nanoparticles*

In order to understand the origin of *localized plasmon resonances* in metal nanoparticles we consider a small metal sphere with radius a embedded in a dielectric medium with dielectric constant ϵ_m in an electric field oriented along the z -direction [6]. The dielectric properties of the metal nanoparticle shall be described by the dielectric constant $\epsilon(\omega)$ [6], see Fig. 2.3.

For a time harmonic incoming electric field \mathbf{E} we have to solve the Helmholtz equation (2.15) for the electric and the magnetic field [7] for the above mentioned geometry. The complete electrodynamic solution to the problem was first given by Gustav Mie in 1908 [32]. However, the basic results can already be seen from an electrostatic approach.

In the *quasi-static approximation* we assume that the nanoparticle size is much smaller than the wavelength of light impinging on the particle, since then the phase of the light wave over the extension of the nanoparticle is at every time step nearly constant and therefore retardation effects can be neglected. Up to a particle size of around 100 nm this approximation describes the optical response of nanoparticles quite well [6].

Therefore, in the following we will neglect the time dependence of all electrodynamic fields. In particular, the applied electric field will be a static one ($\mathbf{E} = E_0 \mathbf{e}_z$). In electro- and magnetostatics the magnetic flux density \mathbf{B} does no more show any time dependence and Faraday's law of induction (2.3) simplifies to $\text{rot } \mathbf{E} = 0$. Hence, we can define an electrostatic scalar potential ϕ as [2]:

$$\mathbf{E} = -\text{grad } \phi \quad (2.33)$$

When we insert equation (2.33) into Gauss's law for the electric field (equation (2.7)) we arrive at the Poisson equation for the scalar potential ϕ , which is $\Delta\phi = -\rho_{\text{tot}}/\epsilon_0$ [2]. For an uncharged system in the dielectric surrounding the total charge density ρ_{tot} remains even in an external electric field \mathbf{E} equal to zero, since the electrons get only slightly shifted with respect to the atoms. In fact, this holds even for uncharged metals, also one at first could assume that in metals, where the conduction electrons are freely moving, local charge densities ($\rho_{\text{tot}} \neq 0$) could form in the presence of an external electric field \mathbf{E} . However, it can be shown using the continuity equation (2.9) that as soon as one defines a conductivity σ of the material ($\mathbf{j} = \sigma\mathbf{E}$), which includes the assumption of a homogeneous, isotropic and linear

medium, the total charge density ρ_{tot} stays zero for all times [26]. Even though the charge density in the medium is zero, of course surface charge densities are allowed at the interface of the metal sphere.

Hence, we need to find a solution for the electric potential ϕ by solving the Laplace equation [6]:

$$\Delta\phi = 0 \quad (2.34)$$

When the solution to the scalar potential ϕ is found the electric field \mathbf{E} can be calculated via equation (2.33). Due to the azimuthal symmetry the solution in spherical coordinates (r, ϑ, φ) does not depend on the azimuth angle φ and is given inside and outside of the nanoparticle by [6, 33]:

$$\phi_{\text{in}}(r, \vartheta) = \sum_{l=0}^{\infty} [A_l r^l] P_l(\cos \vartheta) \quad (2.35)$$

$$\phi_{\text{out}}(r, \vartheta) = \sum_{l=0}^{\infty} [B_l r^l + C_l r^{-(l+1)}] P_l(\cos \vartheta) \quad (2.36)$$

Here, the functions P_l are the Legendre Polynomials [33]. In the next step the coefficients A_l , B_l and C_l have to be determined from boundary conditions. First, far apart from the metal sphere the electric field has to be identical with the applied external electric field \mathbf{E} , and second, the tangential components of the electric field \mathbf{E} and the normal components of the displacement field \mathbf{D} have to be continuous at the interface of the sphere, respectively [6]. This leads to the conditions:

- Electric field at infinity

$$r \rightarrow \infty : \quad \phi_{\text{out}} \rightarrow -E_0 r \cos(\vartheta) \quad (2.37)$$

- Continuity of the tangential components of the \mathbf{E} -field:

$$\left. \frac{\partial \phi_{\text{in}}}{\partial \vartheta} \right|_{r=\alpha} = \left. \frac{\partial \phi_{\text{out}}}{\partial \vartheta} \right|_{r=\alpha} \quad (2.38)$$

- Continuity of the normal components of the \mathbf{D} -field:

$$\epsilon \left. \frac{\partial \phi_{\text{in}}}{\partial r} \right|_{r=a} = \epsilon_m \left. \frac{\partial \phi_{\text{out}}}{\partial r} \right|_{r=a} \quad (2.39)$$

The implementation of the boundary conditions (2.37, 2.38, 2.39) lead to the electric potential inside and outside the metal sphere [6]:

$$\phi_{\text{in}}(r, \vartheta) = -\frac{3\epsilon_m}{\epsilon + 2\epsilon_m} E_0 r \cos(\vartheta) \quad (2.40)$$

$$\phi_{\text{out}}(r, \vartheta) = -E_0 r \cos(\vartheta) + \frac{\epsilon - \epsilon_m}{\epsilon + 2\epsilon_m} E_0 a^3 \frac{\cos(\vartheta)}{r^2} \quad (2.41)$$

Interestingly, the potential inside the metal sphere ϕ_{in} depends only on $r \cos(\vartheta) = z$. Hence, the strength of the internal electric field, which is given by the negative gradient of the scalar potential, is spatially constant. Furthermore outside of the sphere, the scalar potential ϕ_{out} is a superposition of two contributions. The first term on the right hand side of equation (2.41) corresponds to the externally applied electric field. The second term describes the electric field, which is generated by the induced surface charge density on the interface of the metal sphere. Remarkably, that term is of the same functional form like the scalar potential of a static electric dipole \mathbf{p} located at the origin [6, 26]. Therefore, we can write the external scalar potential ϕ_{out} as [6],

$$\phi_{\text{out}} = -E_0 r \cos(\vartheta) + \frac{\mathbf{p} \cdot \mathbf{r}}{4\pi\epsilon_0\epsilon_m r^3}, \quad (2.42)$$

$$\text{with } \mathbf{p} = 4\pi\epsilon_0\epsilon_m a^3 \frac{\epsilon - \epsilon_m}{\epsilon + 2\epsilon_m} \mathbf{E}_0, \quad (2.43)$$

where \mathbf{p} is the induced dipole moment of the sphere in the *quasi-static approximation*. Furthermore, we can link the dipole moment \mathbf{p} to a polarizability α with $\mathbf{p} = \epsilon_0\epsilon_m\alpha\mathbf{E}_0$ [6]. Hence, the polarizability α for the sphere is given by [6]:

$$\alpha = 4\pi a^3 \frac{\epsilon - \epsilon_m}{\epsilon + 2\epsilon_m} \quad (2.44)$$

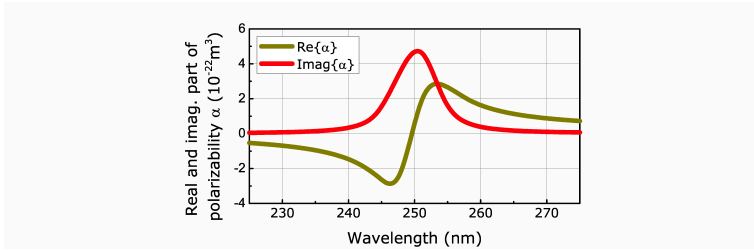


Figure 2.4: Real (green) and imaginary (red) part of the polarizability α of a small gold metal sphere ($a = 10 \text{ nm}$) in air calculated in the *quasi-static approximation* using a Drude model for gold and neglecting interband absorption.

On the one hand we can see that the polarizability α is proportional to the third power of the radius a and hence to the volume of the metal sphere. On the other hand it is proportional to a fractional term which contains the dielectric constants of the metal sphere and the surrounding. This term can exhibit a resonance if the denominator becomes zero. In the case of small damping in the metal we can neglect for the moment the imaginary part of the dielectric constant ϵ_2 of the metal sphere. The resonance then appears for $\text{Re}[\epsilon(\omega)] = -2\epsilon_m$, which is called "*Fröhlich condition*" [6]. When we use a Drude model for the dielectric constant of the metal, as introduced in section 2.1.3, the resonance frequency ω_0 can be calculated for a sphere located in air ($\epsilon_m = 1$) to $\omega_0 = \omega_p/\sqrt{3}$, where ω_p is the plasma frequency of the Drude metal.

In Fig. 2.4 the real and the imaginary part of the polarizability α of a gold sphere with a radius a of 10 nm located in air are shown. Here, a Drude model for the dielectric constant of gold was used. Similar to the complex refractive index $\tilde{n}(\omega)$ introduced in section 2.1.2, the real and the imaginary part of the polarizability α show a dispersive and an absorptive lineshape close to the resonance frequency ω_0 , respectively. However, in reality the imaginary part of the dielectric constant ϵ_2 severely shifts the plasmon resonance to over 500 nm, due to interband transitions, which were neglected in the above calculation.

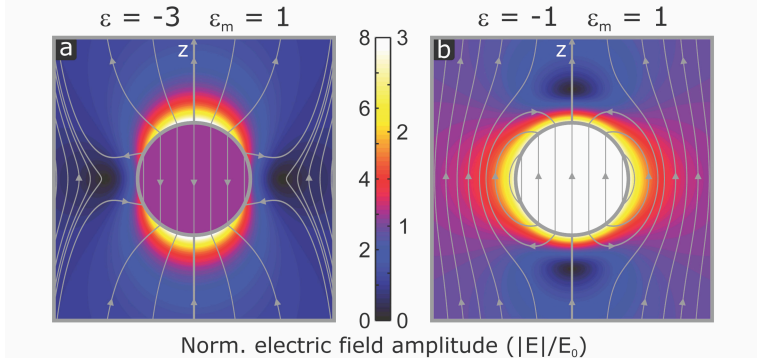


Figure 2.5: Normalized electric field amplitudes $|E|/E_0$ and field lines inside and in the vicinity of a small metal nanoparticle calculated in the *quasi-static approximation* below ((a), $\omega < \omega_0$) and above ((b), $\omega > \omega_0$) the *localized plasmon frequency* ω_0 .

In the next step we want to discuss the electric fields inside and in the vicinity of the metal sphere. As mentioned before, these can be calculated from the scalar potential ϕ via equation (2.33) [6]:

$$\mathbf{E}_{\text{in}} = \frac{3\epsilon_m}{\epsilon + 2\epsilon_m} \mathbf{E}_0 \quad (2.45)$$

$$\mathbf{E}_{\text{out}} = \mathbf{E}_0 + \frac{3(\mathbf{e}_r \cdot \mathbf{p})\mathbf{e}_r - \mathbf{p}}{4\pi\epsilon_0\epsilon_m r^3} \quad (2.46)$$

In Fig. 2.5 normalized electric field amplitudes $|E|/E_0$ and electric field lines inside and outside a small metal sphere located in air ($\epsilon_m = 1$) are shown. As one can see, the metal nanoparticle leads to strong enhancement of the electric field \mathbf{E} close to resonance inside and in the near surrounding of the nanoparticle. In Fig. 2.5(a) the dielectric constant of the metal sphere is $\epsilon = -3$, while in Fig. 2.5(b) the case for $\epsilon = -1$ is depicted. The imaginary part of the dielectric constant ϵ_2 of the metal sphere is again neglected. The *localized plasmon resonance* occurs for a dielectric constant of $\epsilon = -2$. For metals, the real part of the dielectric constant increases in the Drude model monotonically

towards higher frequencies. Therefore, $\epsilon = -1$ corresponds to a higher frequency and $\epsilon = -3$ to a lower frequency than the plasmon resonance frequency ω_0 .

For low frequencies (Fig. 2.5(a)) the conduction electrons are able to follow the external electric field \mathbf{E} almost perfectly. Hence, at the instant of time when the external electric field \mathbf{E} is oriented along the positive z -direction the surface charge density at the lower (upper) side of the metal sphere will be negative (positive). As a consequence the electric field \mathbf{E}_{in} inside the metal sphere points opposite and oscillates out of phase to the external electric field \mathbf{E} . For higher frequencies than the plasmon resonance frequency ω_0 (Fig. 2.5b) the situation is vice versa. The conduction electrons cannot follow the external field \mathbf{E} , which leads to an internal electric field which points into the same direction and oscillates in phase with the external electric field \mathbf{E} .

Finally, we want to note that not only the electrodynamic fields become resonantly enhanced in the vicinity of a metal nanoparticle, but also the efficiency of scattering and absorption of light of the metal nanoparticle. For small particles which are much smaller than the wavelength λ of light, scattering and absorption cross sections C_{sca} and C_{abs} become [6, 7]:

$$C_{\text{abs}} = k \cdot \text{Im} [\alpha] \sim a^3 \quad (2.47)$$

$$C_{\text{sca}} = k^4 |\alpha|^2 \sim a^6 \quad (2.48)$$

The important conclusion from these cross sections for small particles is that absorption is proportional to the volume of the nanoparticle, while scattering is proportional to the volume squared. Hence, for very small particles absorption dominates, but for increasing particle size scattering outperforms absorption.

2.2.2 *Complex Plasmonic Nanostructure Arrays and Their Fabrication*

In the last section we have seen on a fundamental level how localized surface plasmon resonances in small spherical metal nanoparticles can be formed. In general, these resonances not only occur in spherical particles, but also in nanoparticles of arbitrary size and shape. For example, more elongated ellipsoidal particles, for which as well an analytic solution in the quasi static approximation can be found, exhibit different resonance frequencies ω_0 for light polarized along their principal axes [6]. For light polarized along the long axis, the resonance frequency ω_0 can be severely shifted to longer wavelength [34]. Hence, by tailoring the aspect ratio, the resonance position can be tuned to a desired spectral position. However, the aspect ratio and the size of the nanoparticles not only influence the resonance position ω_0 but also the quality factor Q , meaning the damping γ of the plasmon resonances [29, 35], which originates from increased radiative damping for larger and in particular spherical particles. We will see in the third chapter that the damping γ is directly related to the electric field enhancement $|\mathbf{E}|/|\mathbf{E}_0|$, and hence it is most often highly important to keep the damping as low as possible for nonlinear optics applications.

Furthermore, plasmonic nanoparticles which are located close to each other and whose distance is smaller than about 100 nm start to interact via their optical near-fields. The interaction between two plasmonic nanoparticles can be described and understood in a hybridization scheme [36–39], similar to the formation of molecules from atoms. Such as the atomic wavefunctions also the plasmonic modes hybridize, couple and form symmetric and antisymmetric charge oscillations, whose corresponding modes are shifted to lower and higher energies, respectively.

The feasibility to artificially tune plasmonic resonances to arbitrary spectral positions paved the way to an entire new field of

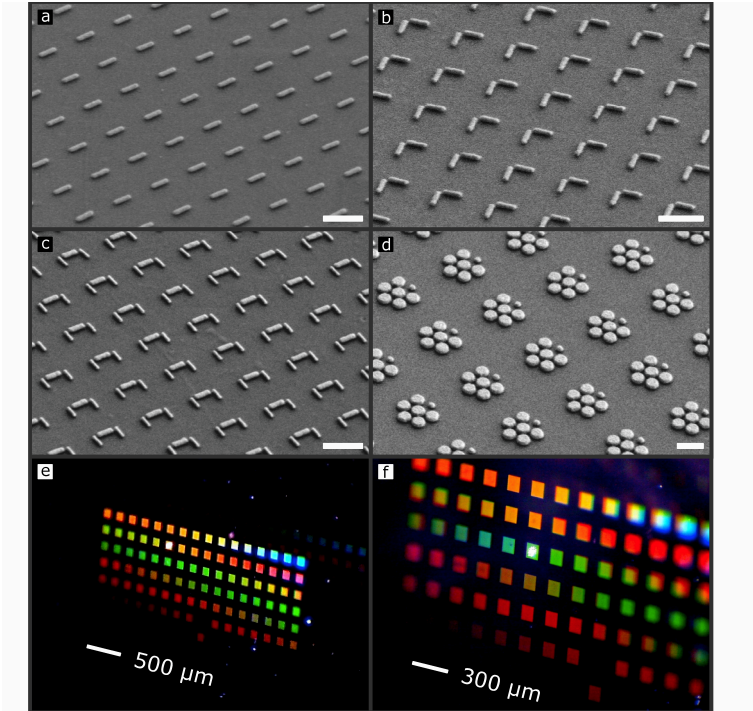


Figure 2.6: (a-d) Scanning electron micrograph overview images of various plasmonic nanostructure array samples. The scale bars are 500 nm. (e, f) USB-microscope images which show an overview of a nanoantenna array sample. Each square corresponds to a nanoantenna array with a size of $100 \times 100 \mu\text{m}^2$. The various antenna arrays appear under different colors since they exhibit different lattice constants and diffract different wavelength of the illuminating light source into the direction of the microscope. In the right image one can observe the laser spot, which is focused onto a nanoantenna array in the third row.

research, namely the development of so called *metamaterials*. In metamaterials mainly metallic but also dielectric sub-wavelength structures are manufactured in a 2D or also 3D periodic fashion [40, 41], which allows for engineering materials with a desired effective optical response. By the implementation of for example U-shaped metallic nanostructures, so called split ring resonators (SRR) [42], not only the electric but also the magnetic optical response can be tailored, since the circulating current in these kind of nanostructures constitutes a magnetic mode [43–46]. Furthermore, the possibility to set the electric permittivity $\epsilon(\omega)$ and the magnetic permeability $\mu(\omega)$ to a value below zero even allows for a negative refractive index n [40, 47–52].

Similar to metamaterials, in this thesis, the optical response of two dimensional periodic arrays of sub-wavelength sized complex plasmonic nanostructures is investigated. In Fig. 2.6(a-d) scanning electron micrographs of investigated samples are shown. Each sample consists of a basic nanostructure element, which is arranged in a 2D periodic fashion. Furthermore, each nanostructure array exhibits a lateral size of typically 100 μm . Therefore, every nanostructure array consists of about 200x200 elements. Fig. 2.6(e, f) shows optical microscope overview images of a nanostructure array sample. The different colors of the square nanostructure arrays arise from the different lattice constants on this particular sample.

The plasmonic nanostructure arrays investigated in this thesis are fabricated by electron beam lithography, which is briefly described in the following. Therefore, first a double layer of Poly(methyl methacrylate) (PMMA) is spin-coated on a fused silica substrate (Suprasil, Heraeus). Then, the nanostructure arrays are defined and written by electron beam exposure followed by a short developing of the resist. Subsequently, at first a 2 nm Cr adhesion layer and then a gold layer of the desired thickness of the nanostructures is evaporated by electron beam evaporation. Finally, the resist is removed in a lift-off process in a N-Ethyl-2-pyrrolidon (NEP) solution.

2.3 NONLINEAR OPTICS

The development of the "Laser" by T. H. Maiman in the year 1960 [16] paved the way to the field of research "*Nonlinear Optics*", which treats and describes the interaction of intense electromagnetic waves with matter. When high intensity electromagnetic waves propagate in a medium one often can observe a plethora of new phenomena, which do not occur for weak light intensities. In particular, high intensity electromagnetic waves very often generate new frequency components via the interaction of the medium. The first observation of a nonlinear optical effect took place already one year after the invention of the laser in 1961 by Franken et. al. [16, 18], who observed the *second harmonic generation* (SHG) from a ruby laser at a wavelength of $\lambda = 694.3 \text{ nm}$, which was frequency doubled to a wavelength of $\lambda = 347.2 \text{ nm}$ in the ultraviolet.

In this thesis, the nonlinear optical properties of metal nanoparticles are studied. Here, we will give a short introduction to the field of "*Nonlinear Optics*" and outline the most important effects arising from an intense light-matter interaction. At last, an extension of the Lorentz oscillator model to the nonlinear regime is given, which is extremely important for the investigation of resonant optical nonlinearities, like it is done in this thesis.

2.3.1 *Nonlinear Polarization and Nonlinear Susceptibility*

For an introduction to "*Nonlinear Optics*" and to explain and describe the novel phenomena arising in this field of research it is more convenient to switch back to a time domain description of the polarization \mathbf{P} , which we introduced in the case of a linear optical response in equation (2.14) in the frequency domain. When we transform equation (2.14) back to the time domain the product of the susceptibility $\chi^{(1)}(\omega)$ and the electric field amplitude $\mathbf{E}(\omega)$

in the frequency domain leads to a convolution of both quantities in the time domain:

$$\mathbf{P}(t) = \epsilon_0 \int_{-\infty}^{\infty} dt' \chi^{(1)}(t-t') \mathbf{E}(t') \quad (2.49)$$

In general, for a time dependent susceptibility and electric field, the convolution (2.49) has to be evaluated. However, in case of an instantaneous optical response of the medium or in the case of a plane wave excitation ($\mathbf{E}(t) = \mathbf{E}_1 \cdot e^{-i\omega_1 t}$) the convolution integral can be neglected. Hence, in the following we consider an instantaneous optical response of our medium, which is true for low frequencies and therefore, markedly below any absorptive resonances [16]. The first order susceptibility then can be written as $\chi^{(1)}(t-t') = \chi^{(1)} \cdot \delta(t-t')$, where $\delta(t-t')$ is the Dirac delta function, and the polarization in the linear regime becomes $\mathbf{P}(t) = \epsilon_0 \chi^{(1)} \mathbf{E}(t)$.

However, the term in the polarization \mathbf{P} , which is linear in the electric field \mathbf{E} , is only the first term of a Taylor expansion. For strong electric field amplitudes terms of higher order in \mathbf{E} get more important and have to be included in the polarization \mathbf{P} :

$$\mathbf{P}(t) = \underbrace{\epsilon_0 \chi^{(1)} \mathbf{E}(t)}_{\mathbf{P}_L(t)} + \underbrace{\epsilon_0 \chi^{(2)} \mathbf{E}(t)^2 + \epsilon_0 \chi^{(3)} \mathbf{E}(t)^3 + \dots}_{\mathbf{P}_{NL}(t)} \quad (2.50)$$

Here, the first term corresponds to the linear polarization \mathbf{P}_L and describes linear optical effects like dispersion and absorption. The following terms, which are of higher order in \mathbf{E} than the linear term, are summarized in the nonlinear polarization \mathbf{P}_{NL} , where the proportionality constants $\chi^{(n)}$ are the susceptibilities of n^{th} order. Such as in the linear case these susceptibilities are for anisotropic materials in general tensors of the order $(n+1)$. For isotropic materials, or when only one tensorial component is of interest, the tensorial character can often be neglected. Furthermore, symmetries of the crystal lattice very often allow to substantially reduce the amount of nonzero tensorial components

[53]. Also the higher order susceptibilities are in general time or frequency dependent quantities.

In the following we make an estimate on the order of magnitude of the nonlinear optical susceptibilities $\chi^{(n)}$. Therefore, we have to note that the optical nonlinearities are mostly originating from anharmonicities of the potentials, which bind the electrons to the core of the atoms. For low external electric field strength a bound electron will always "feel" a harmonic potential. However, for field strength on the order of the atomic electric fields the electrons get strongly perturbed from their classical equilibrium position and will "recognize" that the atomic binding potential is not a perfectly harmonic one. For a typical atomic electric field $E_{H\text{-atom}}$ we take the electric field at the position of the 1s electron in the hydrogen atom [16]:

$$E_{H\text{-atom}} = \frac{m_e^2 e^5}{(4\pi\epsilon_0)^3 \hbar^4} \sim 5.14 \cdot 10^{11} \frac{\text{V}}{\text{m}} \quad (2.51)$$

Furthermore, the first order susceptibility $\chi^{(1)}$ for dielectric materials is typically on the order of one [16]. Hence, we can write for our estimate the polarization as $P = \epsilon_0 E \left(1 + \chi^{(2)} E + \chi^{(3)} E^2 + \dots \right)$. If the external electric field is on the order of the atomic electric field and the higher order terms in the polarization P have to be on the order of one to deliver a distinct contribution to the polarization P , then the n^{th} order susceptibilities have to be on the order of the inverse atomic electric field to the power of $(n - 1)$ [16]:

$$\chi^{(n)} \sim \left(\frac{1}{E_{H\text{-atom}}} \right)^{n-1} \quad (2.52)$$

For the 2nd and 3rd order susceptibilities we explicitly obtain [16]:

$$\chi^{(2)} \sim \frac{1}{E_{H\text{-atom}}} \sim 1.94 \cdot 10^{-12} \frac{\text{m}}{\text{V}} \quad (2.53)$$

$$\chi^{(3)} \sim \left(\frac{1}{E_{H\text{-atom}}} \right)^2 \sim 3.78 \cdot 10^{-24} \frac{\text{m}^2}{\text{V}^2} \quad (2.54)$$

The estimate turns out to be quite accurate when compared to typical measured values of nonlinear optical susceptibilities [16]. For example fused silica exhibits a third order susceptibility of about $2.5 \cdot 10^{-22} \text{m}^2/\text{V}^2$ [16].

2.3.2 Nonlinear Optical Processes of Second Order

In this section we want to discuss nonlinear optical processes which arise from the nonlinear optical polarization $P^{(2)}(t)$ in second order:

$$P^{(2)}(t) = \epsilon_0 \chi^{(2)} E(t)^2 \quad (2.55)$$

Therefore, we assume two co-propagating electromagnetic waves with central frequencies ω_1 and ω_2 :

$$E(t) = \frac{1}{2} \left(E_1(t) \cdot e^{-i\omega_1 t} + E_2(t) \cdot e^{-i\omega_2 t} + \text{c. c.} \right) \quad (2.56)$$

Here, $E_1(t)$ and $E_2(t)$ are the complex slowly varying envelopes of the two electric field waves, which are in general, when for example describing the electric field of ultrashort laser pulses, composed of a real amplitude $|E_1(t)|$ and a complex phase factor $e^{i\phi_1(t)}$. In the case of continuous wave electric fields the slowly varying envelopes simply constitute a constant amplitude. The "c. c." has the meaning of the "complex conjugate", since the electric field has to be a real quantity. For the second order nonlinear polarization $P^{(2)}(t)$ we have to calculate the second power of the electric field $E(t)^2$ [16]:

$$\begin{aligned} E(t)^2 = & \underbrace{\frac{1}{2} (|E_1|^2 + |E_2|^2)}_{\text{OR}} + \underbrace{\frac{1}{4} (E_1^2 \cdot e^{-i2\omega_1 t} + E_2^2 \cdot e^{-i2\omega_2 t})}_{\text{SHG}} \quad (2.57) \\ & + \underbrace{\frac{1}{2} E_1 E_2 \cdot e^{-i(\omega_1 + \omega_2)t}}_{\text{SFG}} + \underbrace{\frac{1}{2} E_1 E_2^* \cdot e^{-i(\omega_1 - \omega_2)t}}_{\text{DFG}} + \text{c. c.} \end{aligned}$$

As a result we obtain various terms oscillating at different frequency components. The first term in equation (2.57) describes

the effect of *optical rectification* (OR), which oscillates for a continuous wave at "zero" frequency and hence, this term corresponds to a constant electric field. However, for ultrashort laser pulses the OR terms oscillate at about the inverse duration of the time-dependent slowly varying envelopes. If the exciting laser pulses are located in the visible or the near-infrared spectral region and exhibit pulse durations in the order of several hundred femtoseconds ($\text{fs} = 10^{-15}\text{s}$) or below the optical rectification describes the generation of electromagnetic radiation in the THz regime [54]. The second term constitutes the frequencies $2\omega_1$ and $2\omega_2$, hence, the corresponding effect is called *second harmonic generation* (SHG).

The previous two terms described the difference and the sum of two identical frequencies. However, also sums and differences between two different frequencies ω_1 and ω_2 are allowed, which leads to the next two terms oscillating at $\omega_1 + \omega_2$ and $\omega_1 - \omega_2$. The corresponding effects are naturally called *sum frequency generation* (SFG) and *difference frequency generation* (DFG).

So far, we considered the different possible contributions to the nonlinear polarisation $P^{(2)}(t)$ in second order, which in principle can occur. However, we did not take into account any optical properties of the medium. These are governed by the different optical susceptibilities $\chi^{(n)}$ of n^{th} order. In the following we will show, that nonlinear optical processes of even order, in particular second order, can only appear in media which show a lack of inversion symmetry. Therefore, we consider the nonlinear polarization $P^{(2n)}$ of the order $(2n)$ in tensorial notation.

$$P_i^{(2n)} = \epsilon_0 \chi_{i,j,k,\dots,2n,2n+1}^{(2n)} E_j E_k \dots E_{2n} E_{2n+1} \quad (2.58)$$

$$n = 1, 2, 3, \dots$$

Here, every index of the susceptibility $\chi^{(2n)}$ corresponds to a cartesian coordinate (x,y,z) . Furthermore, like in Einstein's notation we imply a summation over all cartesian coordinates if an index appears twice. In the next step, we apply a spatial inver-

sion on equation (2.58), which adds a negative sign to all vectorial quantities. However, we assume that our medium shows inversion symmetry. Hence, the susceptibility $\chi^{(2n)}$ will be unaffected by the inversion:

$$-P_i^{(2n)} = \epsilon_0 \chi_{i,j,k,\dots,2n,2n+1}^{(2n)} (-E_j)(-E_k)\dots(-E_{2n})(-E_{2n+1}) \quad (2.59)$$

$$= \epsilon_0 \chi_{i,j,k,\dots,2n,2n+1}^{(2n)} E_j E_k \dots E_{2n} E_{2n+1} \quad (2.60)$$

$$= P_i^{(2n)} \quad (2.61)$$

For arbitrary electric field distributions E the equation $P_i^{(2n)} = -P_i^{(2n)}$ can only be fulfilled for a vanishing nonlinear polarization $P^{(2n)}$:

$$P_i^{(2n)} = 0 \quad \Rightarrow \quad \boxed{\chi_{i,j,k,\dots,2n,2n+1}^{(2n)} = 0} \quad (2.62)$$

$n = 1, 2, 3, \dots$

Hence, we can conclude that nonlinear optical processes of even order vanish in the bulk of all centro-symmetric materials. However, locally the inversion symmetry can be broken at the interface also of centro-symmetric materials, which allows for a non vanishing nonlinear susceptibility at the surface [55].

2.3.3 Nonlinear Optical Processes of Third Order and the Nonlinear Refractive Index

The nonlinear optical processes of third order are governed by the nonlinear polarization $P^{(3)}(t)$:

$$P^{(3)}(t) = \epsilon_0 \chi^{(3)} E(t)^3 \quad (2.63)$$

Third order processes regard the interaction of four photons with different or also equal frequencies ω . Hence, in general these processes are termed *four wave mixing* (FWM). In typical experiments there are three incoming photons at frequency ω_1 , ω_2 and

ω_3 and one outgoing photon at frequency ω_4 , where of course one or more frequencies also can be identical:

$$\omega_4 = \pm\omega_1 \pm \omega_2 \pm \omega_3 \quad (2.64)$$

Such as in the case of a second order process the different frequency components can enter with positive or negative sign, which leads to a variety of new possible frequency components. Since the calculation of the general case with three different incoming frequencies is quite sophisticated we only cover the case where the three incoming electromagnetic waves exhibit identical central frequency ω_1 :

$$E(t) = \frac{1}{2}E_1(t) \cdot e^{-i\omega_1 t} + c. c. \quad (2.65)$$

Here, $E_1(t)$ again describes the slowly varying envelope of the electric field $E(t)$. In the next step we calculate the third power of the electric field $E(t)$:

$$E(t)^3 = \underbrace{\frac{1}{8}E_1^3 \cdot e^{-i3\omega_1 t}}_{\text{THG}} + \underbrace{\frac{3}{8}|E_1|^2 E_1 \cdot e^{-i\omega_1 t}}_{\text{FWM}} + c. c. \quad (2.66)$$

For our particular case the third order polarization $P^{(3)}(t)$ constitutes two contributions. The first term oscillates at three times the fundamental frequency ω_1 and corresponds to the case in equation (2.64) where all three fundamental frequencies are identical and exhibit a positive sign. The respective process is called *third harmonic generation* (THG). The second term oscillates at the incoming fundamental frequency ω_1 and originates in terms of equation (2.64) from a negative and two positive signs. At first glance, the just mentioned FWM process appears to be quite useless, since it seems to generate photons only at frequencies which are already available. However, it is this term which leads to intriguing phenomena like spatial *self focusing* of optical beams or *self phase modulation* (SPM). SPM can lead to enormous spectral broadening of ultrashort laser pulses, which will be important in the next chapter.

SPM, which is a FWM process, can also be described in the wave picture in terms of an effective intensity dependent refractive index n_{eff} :

$$n_{\text{eff}} = \tilde{n} + n_2 I_1(t) \quad (2.67)$$

Here, \tilde{n} and n_2 are the complex refractive index and the nonlinear refractive index, respectively, and $I_1(t)$ is the slowly varying envelope of the intensity $I(t)$. It is related to the slowly varying envelope of the electric field by $I_1(t) = \frac{1}{2} \epsilon_0 \epsilon_r^{\frac{1}{2}} c |E_1(t)|^2$ [2]. In the following we only consider the degenerate FWM part of the third order polarization $P^{(3)}(t)$:

$$P_{\text{FWM}}^{(3)}(t) = \frac{3}{4} \epsilon_0 \chi^{(3)} |E_1(t)|^2 E(t) \quad (2.68)$$

Together with the linear polarization $P_L(t)$ the polarization $P(t)$ becomes:

$$P(t) = \epsilon_0 \underbrace{\left(\chi^{(1)} + \frac{3}{4} \chi^{(3)} |E_1(t)|^2 \right)}_{\chi_{\text{eff}}^{(1)}} E(t) \quad (2.69)$$

Such as in case of the effective intensity dependent refractive index n_{eff} we can define an effective intensity dependent susceptibility $\chi_{\text{eff}}^{(1)}$. If we adapt the relation between the effective refractive index and the effective susceptibility $n_{\text{eff}}^2 = 1 + \chi_{\text{eff}}^{(1)}$, which we already introduced in section 2.1.1, we come upon that the nonlinear refractive index n_2 is in a good approximation directly related to the third order susceptibility $\chi^{(3)}$ [16]:

$$n_2 = \frac{3}{4 \epsilon_0 \tilde{n}^2 c} \chi^{(3)} \quad (2.70)$$

In order to understand how the nonlinear refractive index n_2 influences the propagation of an electromagnetic wave, we consider an electric field $E(t)$ such as in equation (2.65). The nonlin-

ear refractive index n_2 induces an additional intensity dependent nonlinear temporal phase $\phi_{\text{nl}}(t)$:

$$E(t) = \frac{1}{2} |E_1(t)| \cdot e^{-i\omega_1 t} \cdot e^{i\phi_{\text{nl}}(t)} + \text{c. c.} \quad (2.71)$$

$$\phi_{\text{nl}}(t) = n_2 \frac{\omega_1}{c} I_1(t) z \quad (2.72)$$

When we neglect for the moment dispersive effects, which would originate from the linear complex refractive index \tilde{n} , the total temporal phase $\phi(t)$ of the electric field $E(t)$ becomes:

$$\phi(t) = -\omega_1 t + \phi_{\text{nl}}(t) \quad (2.73)$$

$$= -\omega_1 t + n_2 \frac{\omega_1}{c} I_1(t) z \quad (2.74)$$

In the next step we calculate the negative derivative of the temporal phase $\phi(t)$, which delivers the instantaneous frequency $\omega_{\text{inst}}(t)$ within the slowly varying envelope of the electric field:

$$\omega_{\text{inst}}(t) = -\frac{\partial \phi}{\partial t} \quad (2.75)$$

$$= \omega_1 - n_2 \frac{\omega_1}{c} \frac{\partial I_1}{\partial t} z \quad (2.76)$$

Hence, we can see that a positive nonlinear refractive index n_2 leads to decreasing (increasing) frequencies towards the leading (trailing) edge of the slowly varying envelope. In the field of ultrashort laser pulses, where the slowly varying intensity $I_1(t)$ can often be described by a symmetric Gaussian intensity distribution, this leads to the generation of new frequency components symmetrically around the center of the laser pulses.

Typically, one can observe efficient SPM in optical fibers made of fused silica. In Fig. 2.7 the spectral broadening of a Gaussian laser pulse by SPM in fused silica for a propagation distance of 10 cm is shown. For the simulation we assumed an incoming Gaussian laser pulse with a central wavelength λ_0 of 1000 nm, a pulse duration τ of 100 fs (FWHM) and a peak intensity I_0 in the fused silica of 10 GW/cm².

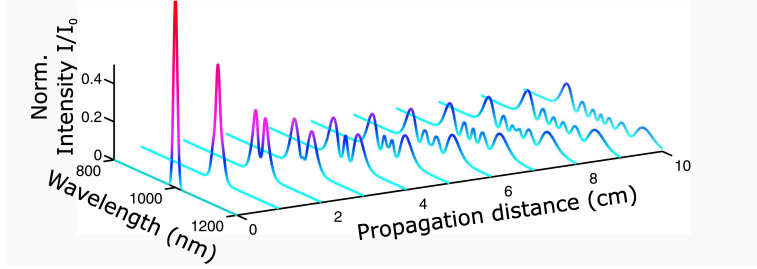


Figure 2.7: Spectral Broadening by SPM of a Gaussian laser pulse with a central wavelength of 1000 nm, a pulse duration of $\tau = 100$ fs (FWHM) and an initial peak intensity $I_0 = 10 \text{ GW/cm}^2$ propagating over a distance of 10 cm in fused silica ($n_2 = 3.2 \cdot 10^{-16} \text{ cm}^2/\text{W}$) (Absorptive and dispersive effects have been neglected).

2.3.4 The Anharmonic Oscillator Model

Routinely, nonlinear optical effects like SHG are performed in nonlinear optical crystals like beta barium borate (BBO) far off any material resonances. The nonlinear optical susceptibilities $\chi^{(n)}$ can then be considered as frequency independent and with an instantaneous optical response, which we assumed in the previous sections. However, as soon as the frequency of the exciting electric field or the frequency of the nonlinear signal get close to a material resonance, the frequency dependence of the nonlinear susceptibilities become highly important, in particular if one wants to understand the efficiency of nonlinear optical processes at these frequencies.

In the following we introduce a basic model for the nonlinear susceptibilities for n^{th} harmonic generation. It is an extension of the Lorentz oscillator model, which already has been discussed in section 2.1.2, to describe the linear optical properties of a medium close to an absorption resonance. In the Lorentz oscillator model we assumed that the electrons which are bound to the cores perform harmonic oscillations when excited by an external oscillating electric field. However, for high external elec-

tric field strengths the electrons will "recognize" that they are not bound to a perfect harmonic potential. Hence, we have to include higher order corrections in the Taylor expansion of the atomic binding potential $V(x)$ [16]:

$$V(x) = \frac{1}{2} m_e \omega_0^2 x^2 + \frac{1}{3} m_e a_2 x^3 + \frac{1}{4} m_e a_3 x^4 + \dots \quad (2.77)$$

Here, the coefficients a_n ($n = 2, 3, \dots$) describe the strength of the anharmonicities of the potential V . In order to account for these higher order terms in a differential equation we have to take the negative derivative with respect to the spatial coordinate x , which delivers the restoring force acting on the bound electrons. Hence, we obtain the differential equation describing a driven anharmonic oscillator:

$$\ddot{x}(t) + 2\gamma\dot{x}(t) + \omega_0^2 x(t) + \sum_{n \geq 2} a_n [x(t)]^n = -\frac{e}{m_e} E(t) \quad (2.78)$$

In contrast to the differential equation of the Lorentz oscillator (2.18) we obtain additional nonlinear terms in the differential equation (2.78). In the general case and to account for arbitrary orders in the potential $V(x)$ we have to sum over the index n . Here, we only want to consider the case with one nonlinear term being nonzero, so that we can neglect the summation.

Unfortunately, the differential equation of the anharmonic oscillator (2.78) cannot be solved analytically. However, the solution can be obtained in a perturbative approach, in analog to the quantum mechanical perturbation theory [16, 25]. Therefore, we expand the solution for the displacement $x(t)$ of an electron in orders of the small perturbation parameter a_n :

$$x(t) = x_0(t) + a_n x_1(t) + a_n^2 x_2(t) + \dots \quad (2.79)$$

If we insert the ansatz for the displacement of equation (2.79) into the differential equation of the anharmonic oscillator (2.78) and

compare on both sides the terms with the same order of a_n we obtain for the zeroth and the first order:

$$a_n^0: \quad \ddot{x}_0(t) + 2\gamma\dot{x}_0(t) + \omega_0^2 x_0(t) = -\frac{e}{m_e} E(t) \quad (2.80)$$

$$a_n^1: \quad \ddot{x}_1(t) + 2\gamma\dot{x}_1(t) + \omega_0^2 x_1(t) = -[x_1(t)]^n \quad (2.81)$$

In zeroth order (a_n^0) the differential equation is completely equivalent to the ordinary differential equation of the Lorentz oscillator. Such as in section 2.1.2 we solve it in the frequency domain. The solution for the displacement $x_0(\omega)$ in zeroth order is then given by

$$x_0(\omega) = -\frac{e}{m_e} g(\omega) E(\omega) \quad (2.82)$$

where $g(\omega) = -(\omega^2 - \omega_0^2 + 2i\gamma\omega)^{-1}$ is called linear response function. Note, that the linear response function $g(\omega)$ is directly proportional to the first order susceptibility $\chi^{(1)}(\omega)$ of equation (2.20).

In the following, to simplify the derivation of the nonlinear optical susceptibilities $\chi^{(n)}$, we assume a continuous wave illumination of the form: $E(t) = E_1 \cdot e^{-i\omega_1 t}$, with a constant electric field amplitude E_1 . The continuous wave electric field $E(t) = E_1 \cdot e^{-i\omega_1 t}$ in the time domain can be written in the frequency domain in terms of a delta function $E(\omega) = 2\pi E_1 \delta(\omega - \omega_1)$:

$$x_0(\omega) = -2\pi \frac{e}{m_e} g(\omega) E_1 \delta(\omega - \omega_1) \quad (2.83)$$

Hence, the Fourier transform back to the time domain can directly be carried out and we obtain:

$$x_0(t) = -\frac{e}{m_e} g(\omega_1) E_1 \cdot e^{-i\omega_1 t} \quad (2.84)$$

We can now address the differential equation (2.81), which we derived in first order (a_n^1) perturbation theory. Remarkably, equation (2.81) is on the left hand side of the same functional form like the differential equation (2.80) in zeroth order. On the right hand side the displacement in zeroth order $x_0(t)$ enters in the

role of an external force. Hence, the solution for the displacement $x_1(\omega)$ in the frequency domain can be analogously calculated by $x_1(\omega) = -g(\omega)\mathcal{F}\{[x_0(t)]^n\}$, where \mathcal{F} denotes a Fourier transform. If we insert the displacement in zeroth order $x_0(t)$ and transform again back to the time domain we finally obtain:

$$x_1(t) = (-1)^n \left(\frac{e}{m_e} \right)^n [g(\omega_1)]^n g(n\omega_1) E_1^n \cdot e^{-in\omega_1 t} \quad (2.85)$$

We can see that the solution for the displacement $x_1(t)$ in first order oscillates at the n^{th} harmonic of the incoming frequency ω_1 . As in case of the Lorentz oscillator model we relate the solution for the displacement $x_1(t)$ to the nonlinear polarization $P^{(n)}(t)$ to derive the expression for the nonlinear susceptibilities of n^{th} order:

$$P^{(n)}(t) = \epsilon_0 \chi^{(n)} E(t)^n = -en_A a_n x_1(t) \quad (2.86)$$

$$= (-1)^n a_n \frac{e^{n+1} n_A}{m_e^n} [g(\omega_1)]^n g(n\omega_1) E(t)^n \quad (2.87)$$

Finally, for n^{th} harmonic generation we obtain for the n^{th} order susceptibility $\chi^{(n)}(\omega)$:

$$\chi^{(n)}(\omega) = (-1)^n a_n \frac{e^{n+1} n_A}{\epsilon_0 m_e^n} [g(\omega)]^n g(n\omega) \quad (2.88)$$

The expression for the nonlinear susceptibility $\chi^{(n)}(\omega)$ is the most important result of this section. In particular, we find that the nonlinear susceptibility $\chi^{(n)}(\omega)$ of n^{th} order is proportional to the n^{th} power of the linear response function $g(\omega)$ at the fundamental frequency ω . Furthermore, the linear response function g also enters linearly at the frequency $n\omega$ of the nonlinear signal. Hence, the linear optical properties determined by the first order susceptibility $\chi^{(1)}(\omega)$, which is directly proportional to the linear response function $g(\omega)$, enter critically into the nonlinear response. This implies that a resonance in the linear optical response, either at the fundamental frequency or at the frequency

of the nonlinear signal, tremendously allow to enhance the conversion efficiency of nonlinear optical processes. Unfortunately, an absorptive resonance at the fundamental wavelength limits very often the absolute laser intensity, since due to absorption the respective material is heated up and hence the damage threshold is strongly reduced.

Notably, throughout this derivation we treated the electric field as a complex value, which is of course not entirely true. As soon as a mathematical nonlinear operation is performed, in principle the real part of this complex valued electric field has to be used, which we did in the previous sections by adding up the complex conjugate. Since we neglected the complex conjugated in this derivation, only the nonlinear term describing n^{th} harmonic generation appears and the other frequency mixing terms with "negative signs" cancel out.

At first glance, it appears odd, that the higher order susceptibilities depend on the first order susceptibility $\chi^{(1)}(\omega)$. Mathematically, in the Taylor expansion of the polarization P to the powers of E in equation (2.50) the different proportionality factors are of course independent from each other. However, the physics in terms of the anharmonic oscillator model tells us that these are strongly related quantities.

ULTRASHORT LASER PULSES: FUNDAMENTAL PRINCIPLES AND EXPERIMENTAL REALIZATION

The main goal of this thesis are nonlinear optical spectroscopy experiments of complex plasmonic nanostructures. As discussed in the introductory paragraph effects in the nonlinear regime only appear for intense electromagnetic fields. Typically, nonlinear optical effects in plasmonic nanostructures can be observed for light intensities higher than about 10 or 100 MW/cm². To obtain such light intensities with a continuous wave (CW) laser source on a nanostructured sample one would have to focus an average power of 1 to 10 kW on an area of 100 × 100 μm². Such high average powers would tremendously heat the nanostructures, which probably would be melted after a short period of time. To reduce the heat exposure of the nanostructures it is possible to utilize ultrashort laser pulses, which exhibit the corresponding intensities only for a very short period of time in the range of several femtoseconds (10⁻¹⁵ s).

Furthermore, to realize nonlinear spectroscopy experiments of plasmonic nanostructures, the laser source should be widely tunable in terms of the operating wavelength. Wavelength tunability of laser systems is very often obtained by utilizing effects from nonlinear optics, like for example in optical parametric oscillators (OPO) [56–59] or optical parametric amplifiers (OPA) [60, 61]. However, on the one hand OPOs operated at ultrashort pulse durations very often show a lack of long term stability, since their cavity length is required to be accurately synchronized to the repetition rate of the pumping laser oscillator. On the other

hand OPAs were in the past restricted to low repetition rate systems with a repetition rate on the order of 1 kHz to 1 MHz. A low repetition rate tremendously leads to a decrease of the signal to noise ratio in nonlinear optics experiments of plasmonic nanostructures, where the peak power of the laser pulses should also not be too high, since in that case the nanostructures will be blown away by a single laser pulse. Only recently OPAs also were made possible at high repetition rates [62] by utilizing high-power femtosecond oscillators as pump sources [63, 64]. Nevertheless, pulse durations markedly below 100 fs, which are desirable for nonlinear spectroscopy experiments, are hard to obtain with the just above mentioned concepts.

Hence, for the generation of widely tunable ultrashort laser pulses, which also operate at a high repetition rate, a completely new laser setup was developed and set up from scratch for this thesis. This chapter is devoted to introduce step wise all components of the setup. In parallel, the theoretical background required to understand the physics behind the setup will be explained. In the first section the Yb:KGW oscillator, which throughout this thesis serves as pump source, is introduced. The propagation of the femtosecond Yb:KGW laser pulses in optical fibers allows to tremendously broaden their spectrum, which is in this thesis used for example to obtain the wide tunability of the laser pulses. Hence, in the next paragraph a small introduction to *nonlinear fiber optics* [17] is given. Furthermore, the ultrabroad bandwidth of the laser pulses allows to generate ultrashort laser pulses with pulse durations on the order of 10 fs. Therefore, pulse compression techniques have to be employed, which will be briefly introduced in the third section of this chapter. Finally, in the last paragraph we turn to a quite advanced technique for pulse compression and pulse shaping, which is called *Fourier transform pulses shaping*. The combination of all the abilities presented in this chapter will allow for the generation of widely tunable sub-20 fs Gaussian laser pulses, which constitute

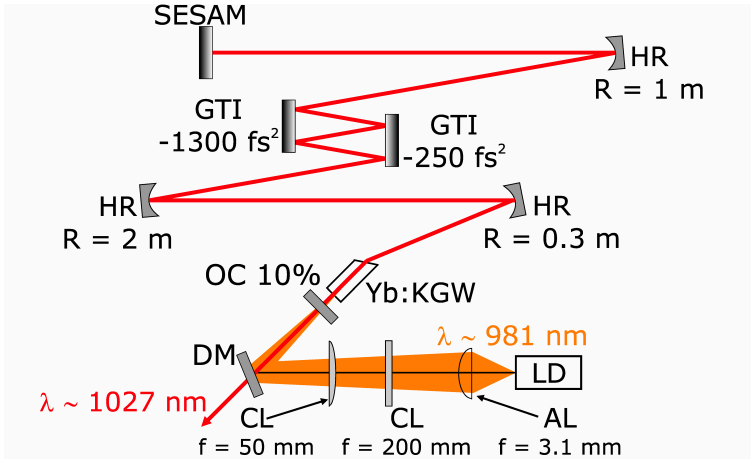


Figure 3.1: Schematic setup of the Yb:KGW oscillator. LD: Laser diode, AL: aspherical lens, CL: cylindrical lens, DM: dichroic mirror, OC: output coupler, HR: highly reflective mirror, GTI: Gires Tournois interferometer mirror, SESAM: semiconductor saturable absorber mirror [65].

an ideal light source for nonlinear optical experiments of plasmonic nanostructures.

3.1 YB:KGW LASER OSCILLATOR

The Yb:KGW laser oscillator set up for this thesis is a further development of the two beam laser system developed by F. Hoos et. al. [63]. We developed an all-solid-state diode-pumped solitary mode-locked Yb:KGW oscillator, which is able to emit femtosecond laser pulses at a wavelength of about 1027 nm and a repetition rate of 44 MHz. A schematic is shown in Fig. 3.1. To pump the Yb:KGW crystal, which is placed at the one end of the resonator, we use a broad-area laser diode (LD) [66]. The laser diode is able to emit from a single emitter with an aperture of $3 \times 200 \mu\text{m}^2$ an average power of up to 18 W. Hence, the beam profile of the laser diode is nearly diffraction limited along the

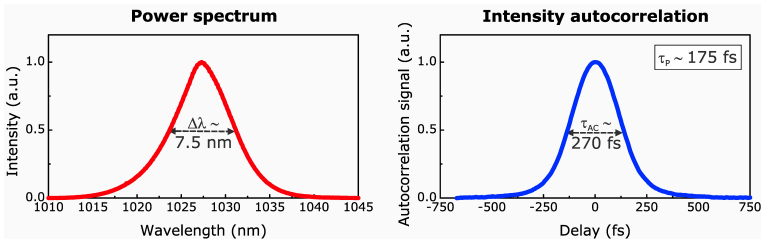


Figure 3.2: Measured power spectrum and measured intensity autocorrelation of the Yb:KGW oscillator laser pulses.

fast axis with an M^2 factor of about 1.2 [63]. Along the slow axis the M^2 factor is on the order of about 50 to 60 [63].

Between the pump diode and the laser crystal we placed a dichroic mirror (DM), which is highly reflective for the pump wavelength at 981 nm and transmitting for the oscillator wavelength at 1027 nm. Furthermore, we pump the laser crystal through the 10 % output coupling (OC) mirror.

On the side of the pump laser diode the Yb:KGW laser crystal is anti-reflection coated for the laser and the pump wavelength, respectively [63]. On the other side the laser crystal is uncoated, but exhibits a cut at Brewster angle. Furthermore, in the Yb:KGW crystal the laser light and the pump light are both polarized along the N_m axis of the laser crystal [63]. In the resonator we use several Gires Tournois interferometer (GTI) mirrors [67] to compensate the temporal dispersion introduced during one round trip and to enable solitary operation. Additionally, to initiate mode-locking we use a semiconductor saturable absorber mirror (SESAM) [65] with a modulation depth $\Delta R = 0.5\%$ and a saturation fluence of $90 \mu\text{J}/\text{cm}^2$.

In Fig. 3.2 a measured power spectrum and a measured non-interferometric intensity autocorrelation of the Yb:KGW oscillator laser pulses are shown. The laser spectrum exhibits a bandwidth of about 7.5 nm (FWHM) and we deduced a pulse dura-

tion τ_p of the laser pulses of about 175 fs (FWHM), which is very close to the Fourier limit of the laser spectrum. Furthermore, we achieve an output power of up to 2.4 W of average power with power fluctuations which were measured to be smaller than 0.15% rms over 1 h.

3.2 LINEAR AND NONLINEAR FIBER OPTICS

The invention of silica optical fibers revolutionized the transmission of data in telecommunication applications, since they allow to transfer optical signals at high data rates and at the ultimate speed of light [68]. Typically, optical fibers are made of fused silica and standard step index fibers consist of a cylindrical fiber core with a slightly higher index of refraction than the surrounding material, which is called the fiber cladding [68]. The slightly higher index of refraction of the core leads to total internal reflection of paraxial optical beams, which is usually the basic working principle for the guidance of light in optical fibers [2, 69].

Beyond their ability to transmit optical signals with low loss at high rates and over large distances optical fibers also had quite an impact on the field of *nonlinear optics* [17]. Their great potential in nonlinear optics originates from the fact that light propagating in an optical fiber is strongly confined to the fiber core. Typically, single mode fibers (SMF) exhibit core diameters below 10 μm , which leads to extremely high light intensities within the fiber. Furthermore, the nonlinear interaction length of a focused beam within a nonlinear optical crystal is usually limited to its Rayleigh length. In contrast, in optical fibers the long propagation distances lead to an extreme and an efficient accumulation of nonlinear optical effects.

In the last years there have been developments towards new kind of optical fibers, which even further boost the efficiency of nonlinear optical effects. In particular, *photonic crystal fibers* (PCF)

allow to precisely tailor the optical properties of the fiber [70, 71] and hence, also its nonlinearity.

A more simple approach to increase the nonlinearity was achieved by the invention of *tapered fibers* [72]. Both, tapered fibers and PCFs, were widely used in this thesis and therefore they will be briefly introduced in the following.

3.2.1 *Tapered Fibers and Photonic Crystal Fibers*

As mention above, beyond standard step index fibers there exist a variety of different fiber concepts, which allow to tailor their linear and nonlinear optical properties over a broad range.

First, in photonic crystal fibers (PCF) the light guidance is achieved by introducing in particular in the cladding region small cylindrical airy holes along the fiber [70]. These holes lead to an effectively reduced refractive index in the cladding region of the fiber. In Fig. 3.3(a) colored scanning electron micrographs (SEM) of the end facet of a PCF are shown. The left picture shows an overview, while the right image shows a close up of the core and the cladding region of the PCF. The outer diameter of the fiber is $125\ \mu\text{m}$ [73]. For this particular PCF (LMA-8, NKT photonics) the airy holes in the cladding region are introduced in a six fold symmetry and for the core of the fiber simply one airy hole is left out. Hence, the core shows a diameter of about $8\ \mu\text{m}$ [73]. In section 3.3.3 we will utilize this fiber to enormously broaden the laser spectrum of the laser pulses to a bandwidth of over 300 nm, which subsequently will enable the recompression of the laser pulses to pulse durations of only several femtoseconds.

Secondly, tapered fibers facilitate the enhancement of nonlinear optical effects in optical fibers with a quite simple concept [72, 74–76]. These fibers are fabricated from standard step index fibers, in our case from the SMF-28 from the company Corning. The

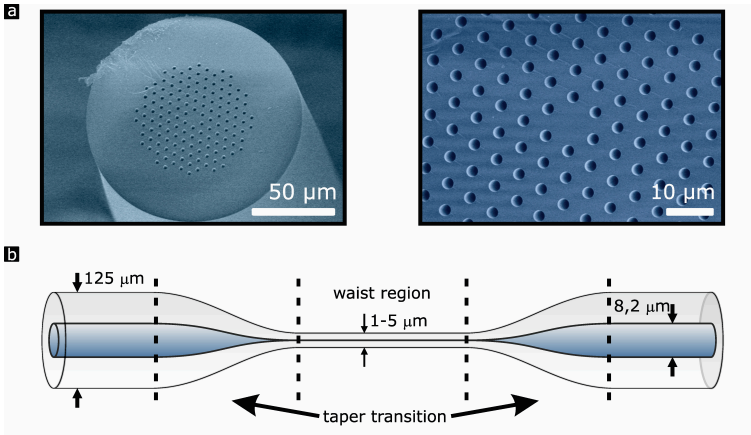


Figure 3.3: a) Scanning electron micrographs of the end facet of an endlessly single mode (ESM) large mode area (LMA) photonic crystal fiber (LMA-8). b) Schematic illustration of a tapered fiber.

SMF-28 shows a core diameter of $8.2 \mu\text{m}$, a cladding diameter of $125 \mu\text{m}$ and the refractive index difference $\Delta n = (n_1 - n_2)/n_1$ between the core refractive index n_1 and the cladding refractive index n_2 is only 0.36% [77].

In order to boost the effective nonlinearity of such a step index fiber, it is possible to taper the fiber to even smaller diameters, which is achieved by heating and pulling the fiber simultaneously [72]. The local heating typically is done either by focusing an intense laser beam on the fiber or, like in our case, by simply heating the fiber from below with a propane/butane flame. The drawing of the fiber is completely computer controlled and the adjustment of the drawing speed and the movement of the flame with respect to the fiber allows to fabricate a variety of different fiber profiles, for example also conical or sinusoidal fiber profiles [74, 75].

A typical profile of a tapered fiber consists of three regions [78–80], see Fig. 3.3(b). In the center there is the so called waist region, where the diameter of the fiber has been tapered to about

a few microns. On both sides of the waist over about 1 or 2 cm along the fiber the diameter increases monotonically in the taper transition regions. Finally, on both ends there are small pieces of the original fiber, which can be used for in and output coupling. By tapering the original diameter of 125 μm down to only a few microns, the light intensity in the fiber and hence the effective nonlinearity of the fiber get strongly enhanced.

Beyond the highly increased effective nonlinearity the tapering also influences the linear optical properties, namely the dispersion of the fiber. In an optical fiber the dispersion of the material and the so called waveguide dispersion, which accounts for the geometrical properties of the fiber, lead to an effective refractive index. In particular, for very thin waist diameters the waveguide dispersion can lead to an effective refractive index, which shows anomalous group delay dispersion in the visible and the near infrared. Anomalous dispersion and enhanced nonlinearity acting simultaneously can lead to the formation of optical solitons, which are very important for the process of efficient supercontinuum generation [17, 71].

Noteworthy, in the waist region of a tapered fiber the propagation of light in fact takes place in the cladding, since here the original fiber core shows a diameter of only a few hundred nanometers. Hence, the air in the surrounding of the waist region adopts the role of a cladding. It's quite astonishing that at the end of the waist region the light "finds" its way back into the core of the fiber.

3.2.2 *Supercontinuum Generation in Nonlinear Optical Fibers*

When femtosecond laser pulses are coupled into a highly nonlinear optical fiber the interplay of dispersive and nonlinear optical effects can lead to enormous spectral broadening, which is also called *white light generation* or *supercontinuum generation*. For ul-

ultrashort laser pulses with extreme light intensities the enormous spectral broadening is the result of various optical effects acting simultaneously. These effects can be described by the *Generalized Nonlinear Schrödinger equation* (GNLSE) [71, 80]:

$$\begin{aligned} \frac{\partial A(z, T)}{\partial z} = & i \sum_{k \geq 2} \frac{i^k}{k!} \beta_k \frac{\partial^k}{\partial T^k} A(z, T) \\ & + i\gamma_0 \left(1 + \frac{i}{\omega_0} \frac{\partial}{\partial T} \right) \left(A(z, T) \int_{-\infty}^{\infty} dt' R(t') |A(z, T - t')|^2 \right) \end{aligned} \quad (3.1)$$

The GNLSE describes the spectral and temporal evolution of the slowly varying pulse envelope $A(z, T)$, when propagating along an optical fiber. The first term on the right hand side of equation (3.1) accounts for linear optical effects in the fiber, where β_k are the Taylor expansion coefficients of the propagation constant $\beta(\omega)$ [17, 80]. Furthermore, γ_0 is the nonlinear parameter at the central frequency ω_0 , and describes the strength of the effective nonlinearity of the fiber [17]. This nonlinear parameter γ_0 is related to the nonlinear refractive index n_2 via [17, 80]

$$\gamma_0 = \frac{n_2 \omega_0}{A_{\text{eff}} c}, \quad (3.2)$$

where A_{eff} is the effective mode area [17, 80]. Hence, the second term on the right hand side of equation (3.1) accounts for all kind of nonlinear optical effects, to these belong: *self phase modulation* (SPM), *self steepening* and *Raman scattering*.

In section 2.3.3 we already saw that the nonlinear refractive index n_2 can lead to enormous spectral broadening via SPM of ultrashort laser pulses. Furthermore, *self steepening* is the result of an intensity dependent group velocity v_g , which becomes important for very broadband pulses [17]. As a consequence the group velocity is reduced at the peak of the pulse envelope, which leads to a flattening in the leading edge and to a self steepening in the trailing edge of the pulse envelope [80]. The retarded response function $R(t)$ accounts for a non-instantaneous optical response

of the fiber material, e. g. fused silica, which results in *intrapulse Raman scattering* [80]. In general, *Raman scattering* describes the inelastic scattering of photons at optical phonons, and results in an continuous red-shift of the pulse envelope [80].

In particular, the formation of optical solitons is very important for white light generation in the anomalous dispersion regime. If we neglect higher order dispersion ($\beta_k = 0$, $k \geq 3$), self steepening ($\frac{\partial}{\partial T} = 0$) and Raman scattering ($R(t) = \delta(t)$) for the moment, the positive nonlinear phase caused by SPM can then be completely compensated by a negative spectral phase caused by second order dispersion ($\beta_2 < 0$). The result is a fundamental soliton, which fully maintains its spectral and its temporal pulse shape during propagation [17]. Furthermore, there also exist higher order solitons, which do not preserve their pulse shape at all time, but change their spectral and temporal pulse shape periodically [17]. The order of a soliton can be quantified by the soliton number N [17, 80]:

$$N = \sqrt{\frac{\gamma_0 P_0 T_0^2}{|\beta_2|}} \quad (3.3)$$

When high power ultrashort laser pulses enter a nonlinear optical fiber in the anomalous dispersion regime, depending on their peak power P_0 and their pulse duration T_0 (half width at $1/e$), a higher order soliton of the order N can be formed [80]. However, in the presence of perturbation, e.g., higher order dispersion or Raman scattering, it decays to lower order or fundamental solitons, which shift due to Raman scattering to new frequencies [81]. The soliton fission leads at the same time to the generation of an intense dispersive wave at the short wavelength side of the spectrum [71]. Furthermore, as long as the different frequency components still overlap in time, these may interact by four wave mixing (FWM) and fill up the spectral gaps in between [80].

For the experimental realization and the generation of white light laser pulses we fabricated tapered fibers with waist diameters of 3.0 μm , 4.0 μm , 5.0 μm , and a waist length of 8 cm each.

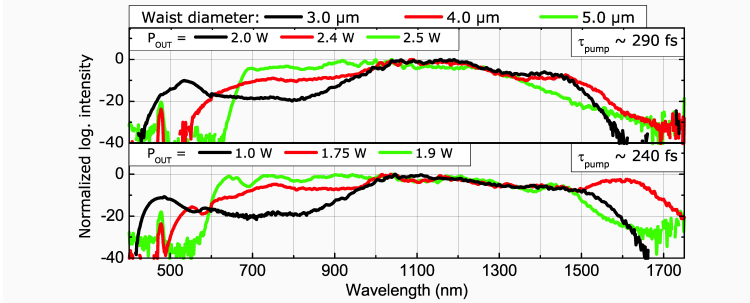


Figure 3.4: Measured high-power white light spectra generated in tapered fibers with different waist diameters and their corresponding average output powers. Top and bottom spectra differ by input pulse duration τ_{pump} and input power.

On both sides of the waist the taper transition length is about 1.5 cm, and approximately 10 cm of SMF-28 remain on both ends for input and output coupling. For the input coupling we use an aspheric lens with a focal length of 15.4 mm and a numerical aperture of 0.16. The throughput of those fibers is on the order of 50% to 70%, depending on the fiber parameters and the input power. Fig. 3.4 shows measured spectra of the generated supercontinua and their corresponding average output powers. For these measurements, the Yb:KGW oscillator was operated at a slightly different configuration than described in section 3.1, which allowed higher average powers, but also longer pulse durations. The top row in Fig. 3.4 corresponds to white light laser pulses generated with 290 fs oscillator pulses, while the bottom row was generated with 240 fs pulses. The difference in the fiber output power between top and bottom arises from the following: Firstly, the average power available from the oscillator is higher when operating at longer pulse durations, and secondly, when using shorter pulse durations the higher peak power can lead to the destruction of the fiber, so that the input power is limited. On the one hand we achieved high output powers of up to 2.5 W using the 290 fs pump pulses. On the other hand with shorter pump pulses of 240 fs broader spectra were obtained due to the higher nonlinearity arising from the higher peak intensities [81].

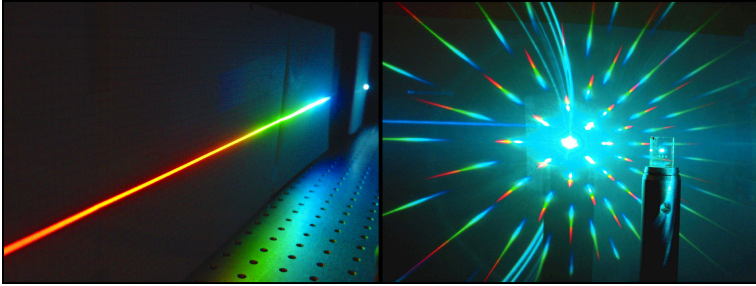


Figure 3.5: Pictures of white light laser pulses, which were directed onto an optical grating. The left image shows the reflectance of the zeroth and the first grating order. The zeroth order is just visible on the right side of the image and constitutes a bright white laser spot. In the right image the white light laser pulses were transmitted through a more complex photonic structure, which leads to aesthetic diffraction of the supercontinuum [82].

Fig. 3.5 shows aesthetic photographs of white light laser pulses, which were spatially diffracted by optical gratings.

3.3 PULSE COMPRESSION

In the last paragraph we experimentally demonstrated that the propagation of high intensity laser pulses in nonlinear optical fibers leads to enormous spectral broadening. Due to the time bandwidth product (TBP), which is the optical analogue of Heisenberg's uncertainty principle, ultrabroadband laser spectra in principle allow for the generation of ultrashort laser pulses. In fact, the duration of laser pulses can only be as short as supported by their spectral bandwidth, which is a consequence of their wave nature. Laser pulses, which exhibit their shortest possible pulse duration allowed from their spectral bandwidth are called *Fourier-limited*.

However, generating ultrabroadband laser pulses close to the Fourier-limit can become quite difficult. Mainly due to disper-

sion, which appears in any material, the different frequency components of a broadband laser pulse get out of phase. This fact tremendously broadens the temporal pulse envelope of ultrabroadband laser pulses. Furthermore, the plethora of nonlinear effects used in the last section for spectrally broadening can lead to a very complex phase of the laser pulses.

There exist a variety of different possibilities to recompress and compensate the dispersion of laser pulses. One option is to utilize prism or grating sequences, where different frequency components travel different optical paths and therefore are shifted in time with respect to each other [83]. In the next section we will utilize such a prism sequence to compress different spectral parts of the previously generated supercontinua, which will lead to a widely tunable laser source with pulse durations down to 26 fs.

The dispersion and the phase of the complete supercontinua are too complex to compress the laser pulses only with the prism sequence to the Fourier-limit. Hence, in the subsequent section we investigate the influence of the fiber properties on the phase of the generated broadband laser pulses. Spectral broadening in the normal dispersion regime is less efficient than in the anomalous dispersion regime, however, we will show that laser pulses which were spectrally broadened in the normal dispersion regime exhibit a smooth and recompressible phase distribution [84].

Therefore, at last we will demonstrate the compression of high power laser pulses with a bandwidth of over 300 nm, which have been spectrally broadened in a normal dispersion photonic crystal fiber (LMA-8).

3.3.1 *Generation of Widely Tunable Sub-65 fs Laser Pulses*

In order to develop a pulse compression device we first measured the dispersion of the white light laser pulses after prop-

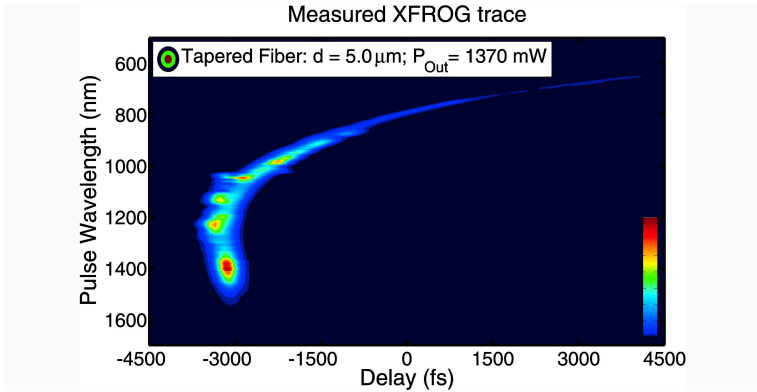


Figure 3.6: Measured XFROG trace of white light laser pulses generated in a tapered fiber with 5.0 μm waist diameter.

agation in the tapered fiber. Therefore, we performed XFROG measurements [85] using type-I interaction in a 25 μm thin BBO crystal. In comparison to FROG [86] the required broadband phase-matching can be more easily achieved when narrowband reference pulses are cross-correlated with broadband supercontinuum pulses. A typical result of those measurements is shown in Fig. 3.6. Since the reference pulses are spectrally and temporally narrow, one can directly observe the envelope of the white light laser pulses in a spectrally and temporally resolved fashion. The retrieval of the electric field can be carried out with an appropriate algorithm [85]. To obtain information about the dispersion it is however sufficient to fit the measured trace with a polynomial function. The slope of this fit then directly gives the linear chirp [81].

From the evaluation of the XFROG trace in Fig. 3.6 we obtained the information that the linear chirp of the white light laser pulses changes over the entire spectral width on the order of a few hundreds up to a few thousands fs^2 . Therefore, it is a complex task to compress the full spectral width of these pulses [19, 87], however, it is possible to compensate at least the second

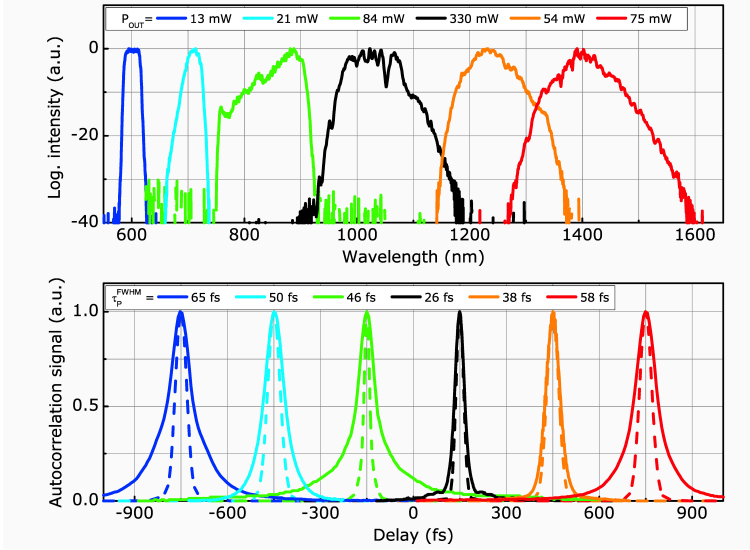


Figure 3.7: Measured spectra (top) and autocorrelations (bottom) with corresponding average output powers and pulse durations of the compressed pulses. The dashed autocorrelations are calculated from the measured spectra and represent the Fourier-limited case (see text).

order dispersion over a small spectral range with a bandwidth of up to 100 nm with a simple prism sequence. Hence, we spectrally filtered our white light laser pulses in different spectral domains and sent the filtered pulses into a prism sequence consisting of two equilateral N-SF10 prisms [83]. The spectral filtering was realized with a variable slit between the two prisms of the sequence. The results we achieved with this setup are displayed in Fig. 3.7, where the spectra and their corresponding autocorrelations of the compressed pulses are shown. To illustrate the quality of compression we plotted in addition calculated autocorrelations which can be obtained from the measured spectra with the assumption of a flat phase and hence representing the Fourier-limited case. A deconvolution factor for each measured autocorrelation can be extracted from these calculations as well. We were able to compress different spectral parts from 600 nm

to 1450 nm down to pulse durations ranging from 26 fs to 65 fs. For the compression, the distance of the prisms was on the order of 1 m, but had to be slightly adjusted for the different spectral parts. For all compressed pulses, except the one at 600 nm, we used a tapered fiber with 5.0 μm waist diameter for the spectral broadening. For the 600 nm pulses, we used a fiber with 4.0 μm waist diameter, because such a fiber leads to a relatively intense spectral part at about 600 nm, which arises from the dispersive wave [71] appearing on the short wavelength side of the supercontinuum [81].

For successful compression it is important to launch appropriate powers through the tapered fiber. For too high powers, the phase becomes too complex, so that the pulses cannot be compressed to ultrashort durations with the prism sequence. For example, for the pulses located at the central wavelength of the oscillator, we adjusted the power such that in the fiber nearly only self phase modulation (SPM) occurs. For this reason, the pulses here could be compressed very well down to 26 fs, because the chirp induced by SPM is over a large extent of the pulse envelope nearly linear [17]. For the pulses that were compressed on the long wavelength side of the oscillator wavelength, we consequently adjusted the power such that the furthest red-shifted soliton was exactly at the desired spectral position. On the short wavelength side we used the position of the dispersive wave to obtain as much power as possible in the compressed pulses. Here one can actually tune the fiber parameters such that the dispersive wave appears at the desired spectral position. However, since the major part of the power is distributed in the solitonic long-wavelength part of the supercontinuum, there the average power is lower than in the other spectral regions. To achieve better compression and higher output power in the visible, one could in principle frequency double the pump at 1025 nm and then use these pulses to generate supercontinua or SPM-broadened spectra in appropriate tapered fibers with the main power distributed in the visible [88]. Also, pulse shapers with

spatial light modulators might be utilized to achieve even shorter pulse durations [87, 89].

3.3.2 *Pulse Stability and Recompressibility after Spectral Broadening in the Normal and the Anomalous Dispersion Regime*

In the last section we demonstrated the spectral filtering and the subsequent temporal compression of small spectral parts of white light laser pulses with a bandwidth of up to 100 nm with a prism sequence. However, there are several reasons which limit the compression of the entire spectral bandwidth to the Fourier-limit. Firstly, the dispersion of ultrabroadband white light laser pulses changes quite considerably over the entire spectral range, this means that there is lot of higher order dispersion. Secondly, due to various nonlinear effects acting in the fiber simultaneously the phase of the electric field of the laser pulses can be quite complex and can also exhibit leaps between the different spectral parts, which renders the recompression nearly impossible.

In this paragraph we will show in simulation that the spectral broadening in nonlinear optical fibers can be divided into three characteristic regions. In particular, we will see that spectral broadening in the normal dispersion regime leads to a smooth and recompressible phase distribution of the output laser pulses [84]. In contrast, when pumping slightly in the anomalous regime, the phase can become very complex and very sensitive to input power fluctuations [84]. Lastly, deep in the anomalous dispersion regime the output spectra become more stable again.

The simulations performed to obtain the following results were done by solving the nonlinear Schrödinger equation (3.1) numerically. Therefore, *S. Pricking* [80] kindly provided his code of the numerical solution of equation (3.1), which is solved by a split step Fourier method [17]. Hence, for the simulations simply the fiber parameters and the input pulse properties had to be chosen.

In order to numerically study the spectral broadening in the three different regimes mentioned above we simulate the propagation of ultrashort laser pulses in the SMF-28 optical fiber [77] and in tapered fibers with different fiber parameters. The input pulse properties are chosen such that they coincide with the parameters of the experimentally used Yb:KGW oscillator ($\lambda_0 = 1027$ nm, $T_0 = 100$ fs ($\tau_P = 2\sqrt{\ln 2}T_0$ [17]), $R = 44$ MHz), see section 3.1, and the average input powers are varied between the different fibers so that the input light intensity in the fibers roughly maintain equal and are high enough so that efficient spectral broadening occurs.

At first we simulate the propagation in a standard SMF-28 over a propagation distance of 10 cm. The zero dispersion wavelength (ZDW) of the SMF-28 is located at around 1313 nm [77], and hence, considerably above our pumping wavelength. Therefore, for this fiber the pump wavelength of around 1027 nm lies well in the normal dispersion regime. To observe efficient spectral broadening, which is here mainly dominated by *self phase modulation* (SPM), we have to pump the fiber with a quite high average power. In Fig. 3.8(a) the XFROG trace [85] and the temporal evolution of the electric field amplitude for an average input power of $P_{av} = 2$ W are shown. In the XFROG trace we can observe that the pulse spectrum broadens quite strongly and that it exhibits a smooth and coherent pulse shape. In addition, the temporal evolution shows slight temporal broadening, but in particular no complex behaviour. Hence, with appropriate techniques these pulses are recompressible close to the Fourier-limit.

In the next step we simulate a tapered fiber with a waist diameter of 4 μm , also over a propagation distance of 10 cm. For such a tapered fiber the ZDW shifts to about 925 nm. Hence, the pump wavelength is now located slightly in the anomalous dispersion regime. As explained in section 3.2.2 the spectral broadening of ultrashort laser pulses in the anomalous dispersion regime is dominated by the formation of optical solitons [71]. Since the absolute value of the dispersion coefficient β_2 is

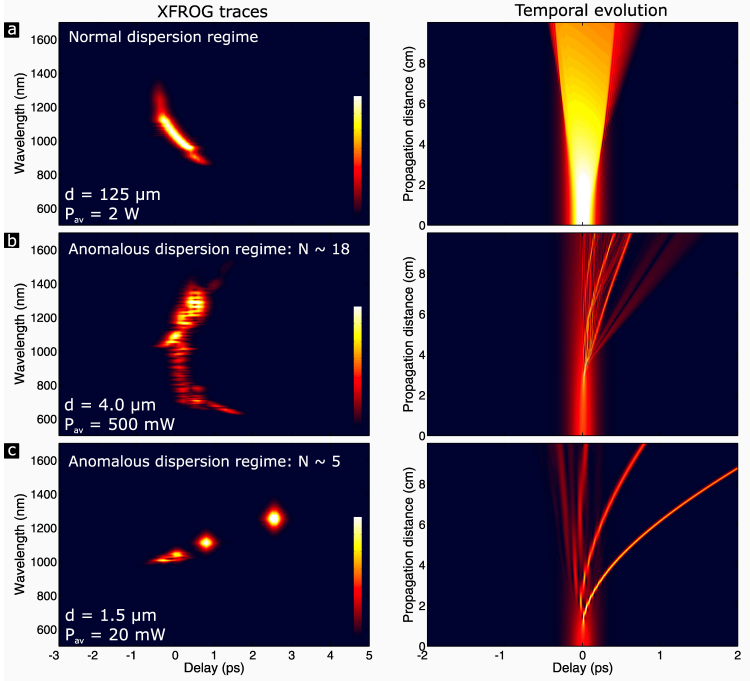


Figure 3.8: Simulated XFROG trace and simulated temporal evolution of the electric field amplitude of ultrashort laser pulses, which were spectrally broadened in a SMF-28 (a) or tapered fibers (b,c) with different waist diameters d . The input pulse parameters in the simulation were $\lambda_0 = 1027 \text{ nm}$, $T_0 = 100 \text{ fs}$, $R = 44 \text{ MHz}$. In order to have roughly comparable and realistic light intensities in the fibers the launched average input power P_{av} has been re-adjusted in the three different simulations.

small, when pumping very close to the ZDW, the soliton number $N = \sqrt{\gamma_0 P_0 T_0^2 / |\beta_2|}$ becomes large. In Fig. 3.8(b) the XFROG trace in the regime of large soliton numbers N , which exhibits in this simulation roughly a value of 18, shows more efficient spectral broadening. However, due to the high soliton number N the pulse shape and the phase of the complex electric field amplitude become very complex. This fact shows in particular up when we consider the corresponding temporal evolution, where we can see that different frequency components move quite chaotic within the pulse shape. Furthermore, the spectral broadening in this situation is also quite sensitive to input power fluctuations [84]. Hence, the temporal compression to the Fourier-limit of such complex pulse shapes acquires very advanced techniques and due to the leaps in the phase it is rendered nearly impossible.

At last a tapered fiber with a thin diameter of only $1.5 \mu\text{m}$ is simulated. In case of such a thin waist diameter the ZDW shifts further down to about 640 nm . Hence, the pump wavelength is now located deep in the anomalous dispersion regime and since the absolute value of the dispersion coefficient β_2 is large, the soliton number N becomes smaller. In our simulation the soliton number N is on the order of 5. In the XFROG trace in Fig. 3.8(c) we can observe the fission of higher order solitons to fundamental solitons, which red-shift due to intrapulse Raman scattering [71, 80]. In particular, first order solitons can be identified in the XFROG trace from their rhombus-like shape [79]. The red-shifted individual solitons exhibit ultrashort pulse durations, cf. the temporal evolution in Fig. 3.8(c), and also a very stable and smooth phase distribution.

In summary, spectral broadening in the anomalous dispersion regime is more efficient than in the normal dispersion regime, however, only in the normal dispersion regime the output spectra exhibit recompressible phase distributions. In the anomalous dispersion regime and in case of high soliton numbers N the phase of the electric field amplitude is so complex that an opti-

mal pulse compression is limited. Even more, the output pulses are also very sensitive to input power fluctuations [84]. Furthermore, deep in the anomalous dispersion regime and for small soliton numbers N the spectral broadening is dominated by the Raman red-shift of fundamental solitons, which constitute very stable ultrashort laser pulses.

At last we mention that all the phenomena described here in simulation have also been observed in a variety of ways in experiment, however, due to compactness, we limited ourselves to only present the simulation results.

3.3.3 *Nonlinear Pulse Compression with a Large Mode Area Photonic Crystal Fiber*

In the last paragraph we have seen that spectral broadening in the normal dispersion regime leads to high intensity and very broadband laser pulses, which exhibit a smooth and re-compressible phase distribution. Even though, supercontinuum generation in the anomalous dispersion regime allows for even broader spectra, the phase of the electric field becomes so complex that the laser pulses are no more re-compressible to the Fourier-limit.

Nonlinear spectroscopy experiments of plasmonic nanostructures, which are the main goal of this thesis, require high power widely tunable ultrashort and very stable laser pulses. Hence, in order to achieve an ultrabroad bandwidth we utilize for the spectral broadening an optical fiber which exhibits a core diameter which is as small as possible, so that efficient *self phase modulation* (SPM) occurs [90]. However, the ZDW of the fiber should still be located well above the pump wavelength of 1027 nm of the Yb:KGW oscillator so that the spectral broadening takes place in the normal dispersion regime. Experimentally, it turned out that the LMA-8 photonic crystal fiber (PCF) from the company NKT photonics [73] performs best for our purposes, see also section

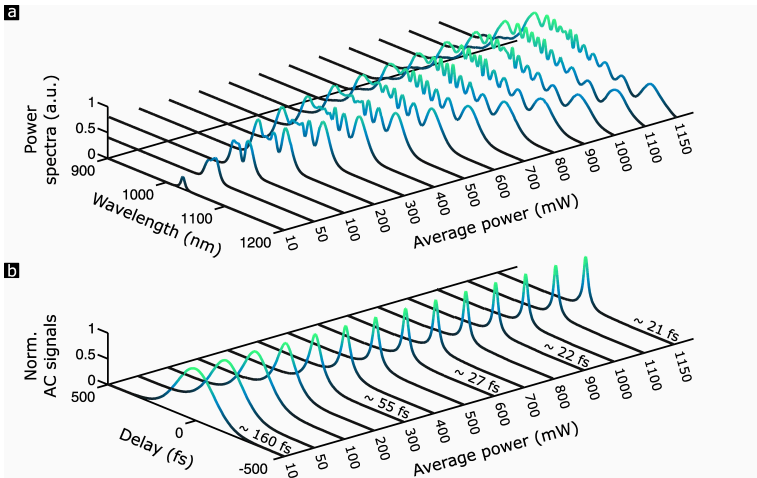


Figure 3.9: Nonlinear pulse compression by spectral broadening of ultrashort laser pulses in an LMA-8 PCF with a length of 10 cm and subsequent propagation through a prism sequence. **a)** Measured power spectra of the compressed laser pulses for different average output powers P_{av} . **b)** Corresponding measured intensity autocorrelations of the compressed pulses. The time values given next to the autocorrelation curves correspond to determined pulse durations τ_p (FWHM).

3.2.1. The mode field diameter for this fiber is at our pump wavelength on the order of $7.5 \mu\text{m}$ and the ZDW is located at a wavelength of about 1160 nm , so the pumping occurs in the normal dispersion regime.

In the experiment we couple after a Faraday isolator about 1.8 W of average power of the Yb:KGW laser pulses into 10 cm of the just mentioned LMA-8 PCF. Input and output coupling is achieved using an aspheric lens with a focal length of 11.0 mm and a $10\times$ microscope objective, respectively. In the fiber enormous spectral broadening due to SPM occurs. The output of the fiber is then sent through a prism sequence consisting of two equilateral SF₁₀ prisms [91]. In Fig. 3.9 measured power spectra (a) and measured intensity autocorrelations (b) for different average output powers P_{av} are shown. As it can be seen the spectra

broaden enormously with increasing average power and exhibit the characteristic shape for SPM-broadened spectra, cf. Fig. 2.7.

Simultaneously, the temporal width of the intensity autocorrelations decreases monotonically. Already for an average output power of about 500 mW the pulse duration τ_p is on the order of 30 fs. Even though, the spectrum broadens by about an additional factor of 2 when further increasing the maximum average output power to 1150 mW the pulse duration τ_p only slightly decreases further to about 21 fs. The reason is that the broader the spectra get the more important becomes higher order dispersion, which can not be independently be compensated simply by our prism sequence.

In order to compress the pulses to the Fourier-limit, which is located at around 10 fs, we have to apply more advanced pulse compression techniques, which will be addressed in the following paragraph.

3.4 FOURIER TRANSFORM PULSE SHAPING

The manipulation of laser pulses in the time domain is extremely limited due to their ultrashort pulse durations in the femtosecond (10^{-15} s) time scale. Typically, electronics are able to sample signals with a rate of up to several GHz. The fastest oscilloscopes nowadays even allow a bandwidth of nearly up to 100 GHz. However, even with such high sampling rates the shortest laser pulses which can be measured have a duration of about several 10 ps.

In order to measure or manipulate laser pulses, which exhibit even shorter pulse durations, different techniques have been developed. On the one hand in the time domain laser pulses are sampled with themselves, which is the basic working principle in autocorrelation measurement techniques [92]. In terms of laser pulse manipulation in the time domain it is possible to generate

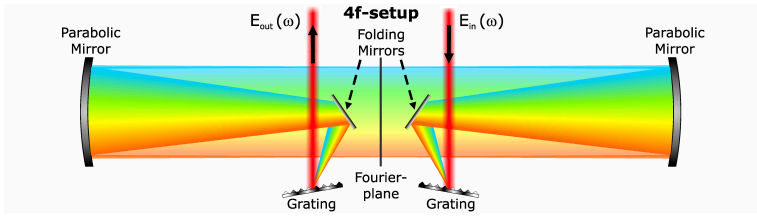


Figure 3.10: Schematic illustration of a 4f-setup used for frequency domain pulse shaping.

double pulses or pulse sequences, utilizing for example Michelson interferometers. However, beyond that time domain shaping of ultrashort laser pulses is strongly limited. On the other hand in the frequency domain the basic measurement device of course is the spectrometer, which is based on optical elements, such as prisms or gratings, which spatially disperse electromagnetic waves. Furthermore, a focusing optical element, like a lens or a curved mirror, in focal distance collimates the diffracted beam. In the Fourier-plane of the spectrometer, which is located another focal length away from the focusing element, the different frequency components are spatially separated best. Hence, a spatially-resolving detector is typically placed there, which allows for measuring the frequency spectrum of the laser pulses.

The setup of a spectrometer is also the basic working principle for frequency domain pulse shaping [83, 93–95]. Instead of placing a detector into the Fourier-plane, there the laser pulses can be manipulated in the frequency domain. Of course, afterward the laser pulses have to be transformed back to a collimated beam, which can be obtained either by an additional mirror in the Fourier-plane, which reflects the beam backwards through the setup, or in a transmittive scheme with a symmetric setup with respect to the Fourier-plane.

The transmittive scheme is used in this thesis and is schematically depicted in Fig. 3.10. Such as in a spectrometer, the incoming laser pulses get spatially and spectrally diffracted by a first

grating and collimated by a curved parabolic mirror. The folding mirror in between is used in order to guarantee normal incidence onto the parabolic mirror. As mentioned before, after another focal length with respect to the first parabolic mirror there is the Fourier-plane of the setup. Finally, a symmetric setup with respect to the Fourier-plane is used to obtain a collimated output beam.

Such as in a CCD-based spectrometer, the next step now is to place a pixelated device into the Fourier-plane. In contrast to a spectrometer, the device is not used to measure laser spectra, but to manipulate or shape the electric field amplitude $E(\omega)$ in the frequency domain in amplitude and phase. We therefore utilize a liquid crystal (LC) spatial light modulator (SLM), which will be introduced in the next section.

3.4.1 *Liquid Crystal Spatial Light Modulation*

Spatial light modulators (SLM) allow for modulating the phase and the polarization state of electromagnetic waves. In television liquid crystal displays (LCD) for example the switching of the brightness of a 2D array of pixels is obtained using birefringent liquid crystals (LC), whose orientation can be controlled by an external static electric field. In this thesis as well an array of LC pixels is implemented within the Fourier plane of the previously introduced 4f setup to modulate the propagating electromagnetic wave.

The SLM used in this thesis contains two separately controllable LC pixel arrays stacked behind each other. We will see that the combination of two 1D pixel arrays allows for the independent control of amplitude and phase of ultrashort laser pulses. Each of both pixel arrays contains 640 stripe electrodes with a width of $97\ \mu\text{m}$, separated by a gap of $3\ \mu\text{m}$ [96]. Hence, a single pixel is $100\ \mu\text{m}$ and the full pixel array $6.4\ \text{cm}$ wide.

A single nematic LC cell consists of a thin layer of nematic LC, located between two parallel glass plates [96]. At the inside of the glass plates transparent indium tin oxide (ITO) electrodes and an alignment layer for the LC molecules are placed [96]. The alignment layer causes a homogeneous orientation of the elongated LC molecules parallel to the adjacent glass plates, which yields an uniaxial birefringent material [96]. The axis parallel to the orientation direction of the elongated LC molecules is also called optical axis (OA) of the material.

An electromagnetic wave polarized perpendicular to the OA of the LC layer will experience the ordinary refractive index n_o during propagation while an electromagnetic wave polarized parallel to the OA experiences the extraordinary refractive index n_e . Without electric field the OA of the LC layer is aligned parallel to the glass plates and as given by the alignment layer. However, if a voltage is applied to the ITO electrodes the resulting electric field tilts the OA of the LC layer toward the direction of the applied electric field. Hence, the refractive index experienced by an electromagnetic wave polarized parallel to the OA (for zero voltage) of the LC layer can be continuously tuned between n_e and n_o . This implies that the phase between both polarization components can as well be continuously tuned.

In the following we will see that the combination of a stack of two LC arrays placed between two polarizers allows for the independent tuning of the amplitude and phase of ultrashort laser pulses. In the LC-SLM used in this thesis the two optical axis of both LC stacks are tilted by 90° with respect to each other, such as schematically shown in Fig. 3.11. To analyze and determine the amplitude A and the phase variation ϕ of the outgoing electric field \mathbf{E}_{out} it is most convenient to apply the Jones-matrix formalism [96]:

$$\mathbf{E}_{\text{out}} = \underline{\underline{M}}_{\text{SLM}} \mathbf{E}_{\text{in}} \quad (3.4)$$

Here \mathbf{E}_{in} is the incoming electric field and $\underline{\underline{M}}_{\text{SLM}}$ corresponds to the transfer matrix describing the entire optical response of the

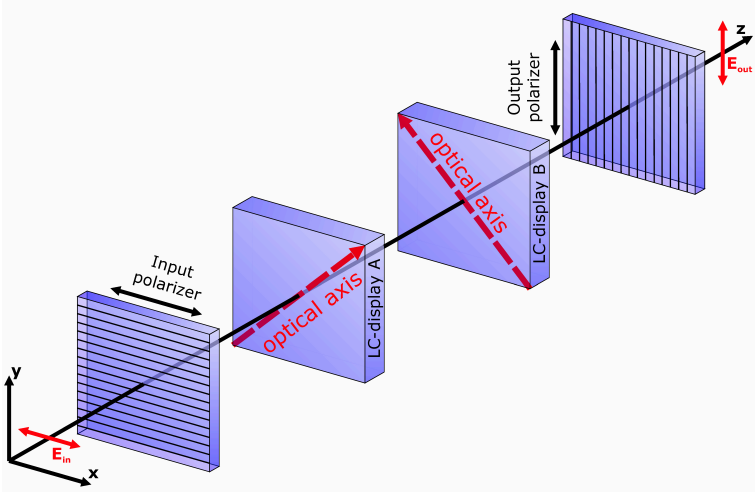


Figure 3.11: Schematic illustration of two stacked LC cells placed between two polarizers for independent amplitude and phase modulation.

optical elements. It can be calculated from fundamental matrices [96]:

$$\underline{\underline{M}}_{\text{SLM}} = \underline{\underline{P}}_y \underline{\underline{R}}_{-45^\circ} \underline{\underline{L}}_B \underline{\underline{L}}_A \underline{\underline{R}}_{45^\circ} \underline{\underline{P}}_x \quad (3.5)$$

$$= \begin{pmatrix} 0 & 0 \\ 0 & 1 \end{pmatrix} \begin{pmatrix} \cos(45^\circ) & -\sin(45^\circ) \\ \sin(45^\circ) & \cos(45^\circ) \end{pmatrix} \begin{pmatrix} 1 & 0 \\ 0 & e^{i\Delta\phi_B} \end{pmatrix} \cdot \begin{pmatrix} e^{i\Delta\phi_A} & 0 \\ 0 & 1 \end{pmatrix} \begin{pmatrix} \cos(45^\circ) & \sin(45^\circ) \\ -\sin(45^\circ) & \cos(45^\circ) \end{pmatrix} \begin{pmatrix} 1 & 0 \\ 0 & 0 \end{pmatrix} \quad (3.6)$$

$$= \frac{1}{2} \begin{pmatrix} 0 & 0 \\ e^{i\Delta\phi_A} - e^{i\Delta\phi_B} & 0 \end{pmatrix} \quad (3.7)$$

Here, the $\underline{\underline{P}}_i$, $\underline{\underline{R}}_\alpha$ and $\underline{\underline{L}}_i$ matrices ($i = A, B$) mathematically describe the effect of a polarizer, a rotation of the coordinate system by the angle α and the relative phase $\Delta\phi_i$ introduced by an LC

cell, respectively. For an incoming electric field $\mathbf{E}_{\text{in}} = E_{\text{in}}\mathbf{e}_x$ polarized along the x-direction we obtain:

$$\mathbf{E}_{\text{in}} = \frac{1}{2} \left(e^{i\Delta\phi_A} - e^{i\Delta\phi_B} \right) E_{\text{in}}\mathbf{e}_y \quad (3.8)$$

$$= \sin \left(\frac{\Delta\phi_A - \Delta\phi_B}{2} \right) e^{i\frac{\pi + \Delta\phi_A + \Delta\phi_B}{2}} E_{\text{in}}\mathbf{e}_y \quad (3.9)$$

Hence, by varying the relative phases $\Delta\phi_A$ and $\Delta\phi_B$ from both LC cells the outgoing electric field \mathbf{E}_{out} polarized along the y-direction can independently be modulated in amplitude A and phase ϕ , which calculate to:

$$A = \sin \left(\frac{\Delta\phi_A - \Delta\phi_B}{2} \right) \quad (3.10)$$

$$\phi = \frac{\pi + \Delta\phi_A + \Delta\phi_B}{2} \quad (3.11)$$

By inverting these equations the relative phases $\Delta\phi_A$ and $\Delta\phi_B$ required for a certain amplitude and phase modulation can be calculated.

Remarkably, for pulse compression of ultrashort laser pulses of course only the phase difference between adjacent pixel cells is important. The absolute phase offset only becomes crucial for ultrashort laser pulses in the single cycle regime, since here the absolute carrier envelope phase takes on greater significance.

3.4.2 *The Complete Experimental Pulse Shaper Setup and its Theoretical Limits*

In the last paragraph the basics of the 4f pulse shaper built up during this thesis and its fundamental working principles have been introduced. In the following we want to summarize the optical components of the entire experimental setup, which is shown in Fig. 3.12.

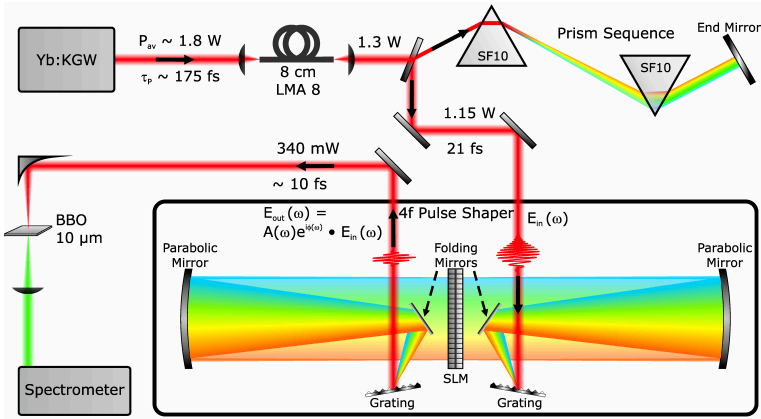


Figure 3.12: Schematic setup. The Yb:KGW oscillator pulses are coupled into an LMA-8 PCF, whose output is precompressed by a prism sequence. The laser pulses are then sent into the 4f pulse shaper for amplitude and phase modulation. At last a nonlinear signal is generated in a $10\ \mu\text{m}$ thin BBO crystal which is measured by a spectrometer.

The Yb:KGW oscillator pulses are coupled into 10 cm of LMA-8 PCF to generate a broadband spectrum spanning over 300 nm. The output of the fiber is then sent through a prism sequence consisting of two equilateral SF10 prism to precompress the laser pulses, see section 3.3.3. After the prism sequence the pulse duration of the laser pulses is already as short as 21 fs with an average power of about 1.15 W. However, the broad spectrum supports much lower pulse durations, so there is higher order dispersion, which cannot be completely compensated using only the prisms.

To get rid of higher orders of dispersion and to shape the spectrum in amplitude the broadband laser pulses are subsequently sent into a 4f pulse shaper [94, 95], which was introduced at the beginning of section 3.4, consisting of two 300 lines/mm gold coated gratings and two parabolic mirrors with a focal length of 444.5 mm. Hence, the two parabolic mirrors are placed at a distance of 889 mm. Furthermore, in this configuration the setup projects a spectral bandwidth of about 450 nm on a spatial region

of about 6.4 cm in the Fourier-plane, which is the spatial width of our LC-SLM.

In the Fourier-plane of the pulse shaper an LC-SLM (Jenoptik, SLM-S640d) with two 640 pixel masks stack behind each other is placed for independent amplitude and phase modulation. By this means the output electric field $E_{\text{out}}(\omega) = A(\omega) \cdot \exp(i \cdot \phi(\omega)) \cdot E_{\text{in}}(\omega)$ can be controlled in a diverse fashion. Here $E_{\text{in}}(\omega)$ denotes the spectral electric field of the laser pulses sent into pulse shaper and $A(\omega)$ and $\phi(\omega)$ correspond to the amplitude and phase applied to the pulse shaper, respectively.

The output of the pulse shaper is finally frequency doubled in a $10 \mu\text{m}$ thin BBO crystal, and the corresponding second harmonic (SH) signal is measured with a spectrometer.

It is very interesting and important to investigate the theoretical limit in terms of the maximum group delay (GD) and the maximum group delay dispersion (GDD) which can be caused or compensated by the SLM. In particular, the limit of the SLM is not given by the total phase offset, which can be generated by the LC pixel cells, since they allow for varying the phase in the whole spectral range over more than 2π . In contrast, the total amount of pixels N of the SLM, or more precisely, the spectral bandwidth which impinges on one pixel limits the maximum GD/GDD. The reason is that the phase between different frequency components propagating through one and the same pixel can of course not be varied. Hence, if the slope of the phase gets too steep, or equivalently the phase within one pixel changes on the order of π , the SLM will not be able to compensate or generate the corresponding GD/GDD [97].

The formula for the maximum group delay GD_{max} can be determined from the just described condition and calculates to [97]:

$$\text{GD}_{\text{max}} = \frac{\lambda_0}{2c\Delta\lambda} \quad (3.12)$$

For a center wavelength λ_0 of 1000 nm and a spectral bandwidth $\Delta\lambda$ of 1 nm impinging on one pixel, which are roughly the values for our pulse shaper setup, we obtain a theoretical limit for the maximum group delay GD_{\max} of about 1.7 ps. Similarly, one can derive an equation for the maximum group delay dispersion GDD_{\max} [97],

$$\text{GDD}_{\max} = \frac{\lambda_0^4}{N\pi c^2 \Delta\lambda^2}, \quad (3.13)$$

where we obtain a theoretical limit of about 5500 fs².

3.4.3 *The Multiphoton Intrapulse Interference Phase Scan*

In the context of pulse shapers, different kind of algorithms have been developed to determine the phase which has to be applied so that Fourier-limited laser pulses are obtained. Most popular among them are evolutionary and genetic algorithms [98]. In addition to those, deterministic algorithms have been developed, which need only one or very few iterations for convergence. Hence we chose to use the multiphoton intrapulse interference phase scan (MIIPS) [99–101], known to need only a few iterations for full compensation of nearly arbitrary orders of dispersion. Of course, an external pulse characterization method such as SPIDER [87, 102], which instantaneously delivers the spectral phase, is appropriate as well. Though, using the MIIPS algorithm no additional equipment is required.

The basic idea of MIIPS is the fact that phase modulation affects the efficiency of nonlinear optical processes. Hence, in order to determine the phase that leads to Fourier-limited laser pulses, a nonlinear signal, in our case a SH, is generated and spectrally measured while scanning a series of phase functions with the pulse shaper. Typically, sinusoidal reference phase functions $\phi_{\text{MIIPS}}(\omega, \delta) = \alpha \cdot \sin[\gamma \cdot (\omega - \omega_0) - \delta]$ are used, where the parameter δ is scanned over a range of 4π . Here, the amplitude α is typically on the order of π and the parameter γ is chosen

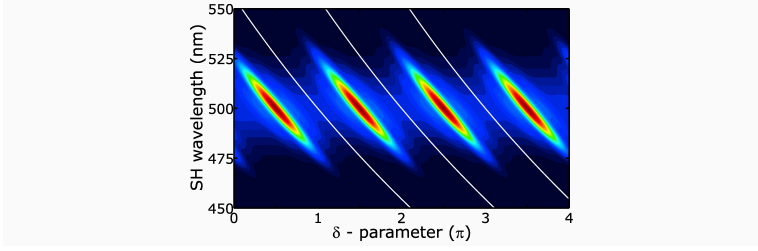


Figure 3.13: Simulated MIIPS trace of Fourier-limited Gaussian laser pulses with a pulse duration of $T_0 = 10$ fs ($\tau_P = 2\sqrt{\ln 2}T_0$ [17]) and a central wavelength of $\lambda_0 = 1000$ nm. The parameters of the MIIPS reference phase Φ_{MIIPS} are $\alpha = \pi$ and $\gamma = \tau_P$.

similar to the pulse duration. The measured result is a MIIPS trace, where the intensity of the SH signal is plotted over the SH wavelength and the δ -parameter.

A simulated MIIPS trace for Fourier-limited Gaussian laser pulses with a pulse duration of $T_0 = 10$ fs (half width at $1/e$) and a central wavelength of $\lambda_0 = 1000$ nm is shown in Fig. 3.13. In order to comprehend the appearance of this MIIPS trace we consider the complete spectral phase $\phi(\omega)$ of the electric field of the pulse shaper output laser pulses. It is composed of the pre-existent spectral phase of the laser pulses $\phi_{\text{laser}}(\omega)$ and the MIIPS reference phase $\Phi_{\text{MIIPS}}(\omega, \delta)$ caused by the pulse shaper:

$$\phi(\omega) = \Phi_{\text{MIIPS}}(\omega, \delta) + \phi_{\text{laser}}(\omega) \quad (3.14)$$

$$= \alpha \sin[\gamma(\omega - \omega_0) - \delta] + \phi_0 + \phi_1(\omega - \omega_0) \quad (3.15)$$

$$+ \frac{1}{2}\phi_2(\omega - \omega_0)^2 + \frac{1}{6}\phi_3(\omega - \omega_0)^3 + \dots \quad (3.16)$$

Here, the pre-existent spectral phase $\phi_{\text{laser}}(\omega)$ has been written in terms of a Taylor series around the central frequency ω_0 of the laser pulses.

In the subsequent SH process a maximum nonlinear signal is generated when the second and all higher order derivatives of the

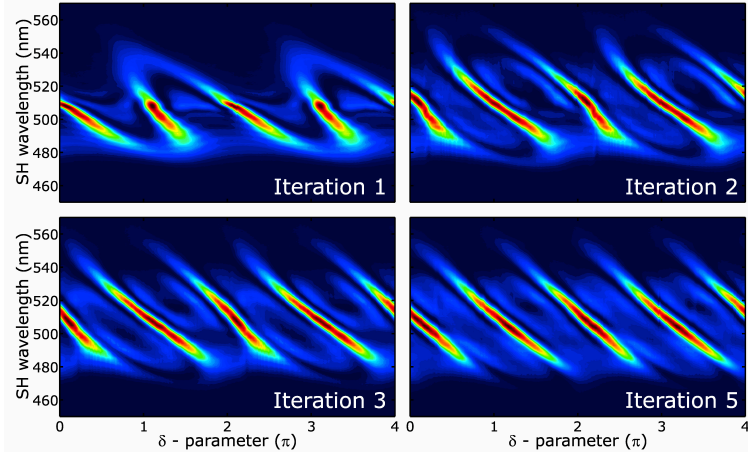


Figure 3.14: Iteratively measured MIIPS traces showing the 1st, 2nd, 3rd and 5th iteration.

spectral phase vanish. The condition that the second derivative has to be equal to zero ($\partial^2\phi/\partial\omega^2 = 0$) leads to:

$$\sin[\gamma(\omega - \omega_0) - \delta] = \frac{1}{\alpha\gamma^2} (\phi_2 + \phi_3(\omega - \omega_0) + \dots) \quad (3.17)$$

For Fourier-limited laser pulses the right hand side of equation (3.17) becomes zero and we obtain $\gamma(\omega - \omega_0) - \delta = n\pi$, with $n \in \mathbb{Z}$. Hence, in the MIIPS trace we observe a maximum nonlinear signal on parallel lines, which are separated by δ equal to π .

In the case of non-Fourier-limited laser pulses the second order dispersion ϕ_2 leads to a constant offset of the MIIPS features in the δ direction. Furthermore, third and fourth order dispersion (ϕ_3, ϕ_4) cause a tilt and a bending of the MIIPS features, respectively. It is therefore possible to directly estimate the amount of spectral phase distortions from the appearance of a measured MIIPS trace [100].

In particular, the MIIPS algorithm allows to compensate nearly arbitrary orders of dispersion with the pulse shaper. Therefore,

the maxima of a first measured MIIPS trace $\delta_{\max}(\omega)$ are determined for every SH wavelength. In Fig. 3.13 the white lines indicate the boundaries of this maxima search routine. From that, an analytical expression allows to derive a compensating phase, which partly reduces the amount of dispersion in the laser pulses [99]. Finally, from iteratively measured MIIPS traces it is possible to retrieve the full spectral phase and to compress the laser pulses to the Fourier-limit. Of course, the zeroth order of the phase and its linear term can not be determined, since they do not have any influence on the nonlinear signal.

Experimental measured MIIPS traces of the laser pulses which were generated in section 3.3.3 are shown in Fig. 3.14, showing the 1st, 2nd, 3rd, and 5th iteration step. In the measurement the best results we obtained for the amplitude α to be equal to 2.5 and the parameter γ set to 20 fs. While in the 1st MIIPS trace the MIIPS features are strongly tilted and bent, already in the 3rd MIIPS trace the pulse quality has remarkably improved. In the 5th iteration the MIIPS trace shows features which are nearly parallel lines separated by π in the δ -direction, indicating that the laser pulses are already very close to the Fourier-limit. Finally, up to 10 iterations could still slightly improve the pulse quality and the compression.

3.4.4 *Amplitude Shaping and Pulse Shaper Assisted Interferometric Frequency Resolved Optical Gating*

After phase shaping of the broadband laser pulses, we observe pulse durations as short as 11.5 fs. However, the pulse spectrum, which is shown in Fig. 3.15(a), still shows the modulated shape typical for SPM-broadened spectra, since up to now the amplitude $A(\omega)$ applied to the pulse shaper was set equal to one. To obtain a desired spectral shape as well, we set the pulse shaper amplitude $A(\omega)$ equal to a desired target amplitude $A_{\text{target}}(\omega)$. Of course, this does not yet lead to the target spectrum $|A_{\text{target}}(\omega)|^2$.

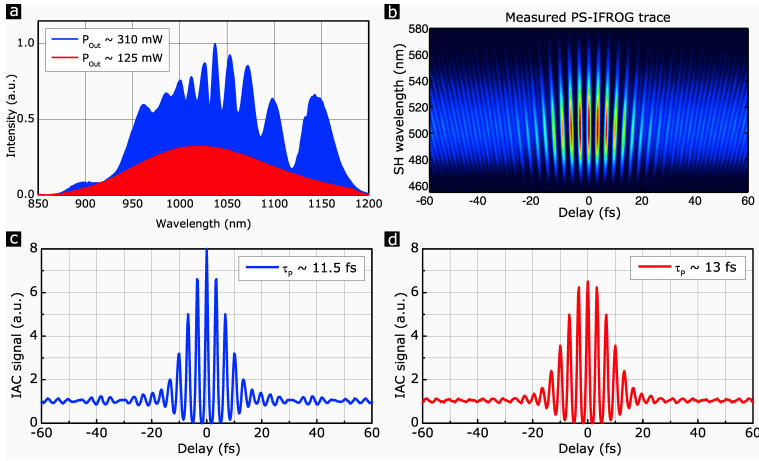


Figure 3.15: a) Measured pulse shaper output spectra and their respective average powers, (blue) without amplitude shaping, (red) using the pulse shaper amplitude $A(\omega)$ to shape a Gaussian-like pulse shape. b) Measured PS-IFROG trace of the Gaussian-shaped spectrum, using the pulse shaper for generation of double pulses (see text). c) and d) Measured interferometric autocorrelations of the spectra depicted in (a).

Hence, we measure the output spectrum $I_{\text{out}}(\omega)$, and use it to correct the amplitude $A(\omega)$ in the following way:

$$A'(\omega) = A(\omega) - \left(\sqrt{I_{\text{out}}(\omega)} - A_{\text{target}}(\omega) \right) \quad (3.18)$$

Here $A'(\omega)$ denotes the new amplitude to be applied to the SLM. Experimentally it turned out to be advantageous when using an iterative procedure for the amplitude shaping as well, so that after 5 to 10 iterations the final spectrum coincides well with the desired target spectrum. An example for the amplitude shaping is shown in Fig. 3.15(a) depicting a broadband Gaussian-like shaped spectrum.

In order to completely characterize our laser pulses in amplitude and phase we can use the pulse shaper as well. Therefore,

we multiply our actual amplitude $A(\omega)$ with a cosine-like amplitude modulation:

$$A_{2P}(\omega) = A(\omega) \cdot \cos\left(\omega \cdot \frac{\Delta\tau}{2}\right) \quad (3.19)$$

Applying the amplitude $A_{2P}(\omega)$ leads to identical double pulses separated in time by the delay $\Delta\tau$ [103]. By this means we have realized a highly stable Michelson interferometer, since it contains no moving parts and the delay between the double pulses can simply be tuned by ramping the parameter $\Delta\tau$. If we measure the SH signal in dependence of the delay $\Delta\tau$ with the spectrometer, we directly obtain the equivalent to an interferometric FROG trace, which we term PS-IFROG (pulse shaper assisted interferometric FROG) and which can be used for full amplitude and phase retrieval as described in [104]. Fig. 3.15(b) shows a measured PS-IFROG trace from the Gaussian-shaped spectrum depicted in Fig. 3.15(a). Fig. 3.15(c,d) show the corresponding interferometric autocorrelations (IAC) of the unshaped and the Gaussian-shaped spectrum from Fig. 3.15(a) which can be obtained by summing up the PS-IFROG traces over all wavelength components, showing pulse durations of 11.5 fs and 13 fs, respectively. These pulse durations have been obtained by evaluation of the corresponding measured PS-IFROG traces. Therefore, the unmodulated kernel of the traces was extracted via Fourier filtering and subsequently entered into an SHG-FROG retrieval algorithm (Femtisoft Technologies).

Note that the temporal sidewings of the Gaussian-like shaped spectrum were remarkably suppressed with respect to the unshaped spectrum as well.

3.4.5 *Widely Tunable sub-20 fs Laser Pulses*

By incorporation of all the abilities we presented above, we are able to shape nearly arbitrary spectra in the range of 900 nm up to

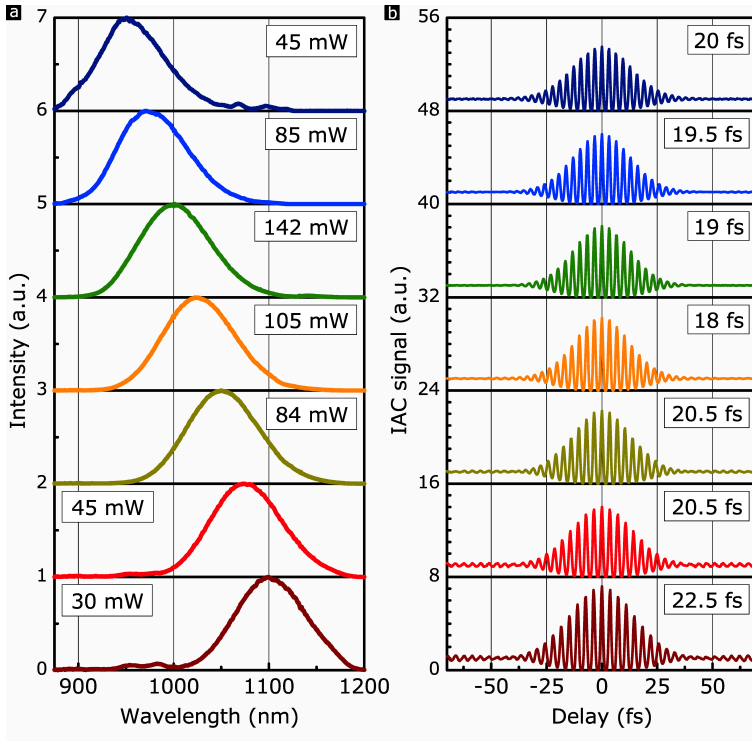


Figure 3.16: **a)** Measured output spectra, which were obtained by iterative amplitude shaping and their measured average output powers. **b)** Corresponding measured interferometric autocorrelations and their determined pulse durations.

1150 nm. Here we demonstrate this by realizing widely tunable Gaussian-shaped sub-20 fs laser pulses. We first use the MIIPS algorithm to compensate the spectral phase. Then we shape the spectrum to a Gaussian-like shape with a bandwidth of about 85 nm, with central wavelengths tunable between 950 nm and 1100 nm. The corresponding measured spectra and their measured average powers are shown in Fig. 3.16(a). Of course, by amplitude shaping the average power is reduced, however, the obtained spectra still show average powers from 30 mW up to 142 mW.

These laser pulses can directly be characterized using the above described PS-IFROG procedure. The corresponding measured IACs and the pulse durations are displayed in Fig. 3.16(b), all exhibiting a pulse duration in the range of 20 fs or below. The pulse durations have been obtained once more by the FROG retrieval of the measured PS-IFROG traces.

Of course, the pulse shaper is not limited to Gaussian-like spectral shapes presented here. For example also squared or double Gaussian spectra can be realized. However, one has to keep in mind that changes of the spectral amplitude always lead to temporal changes as well.

Due to its high repetition rate, its tunability, its ultrashort pulse duration in combination with well-shaped spectra and its high peak power this system is specifically well suited for ultrafast nonlinear spectroscopy. Applications are in particular in the field of nonlinear nano-plasmonics as well as nonlinear and ultrafast spectroscopy of carrier dynamics in solids.

NONLINEAR PLASMONICS

In the field of research *Nonlinear Plasmonics* the nonlinear optical properties of metallic nanostructures and in a broader sense also the amplification of nonlinear optical processes in other materials by the strong electric near-fields of plasmonic nanoantennas is studied and investigated [105, 106]. The interesting nonlinear optical properties of metal nanostructures originate in particular from localized surface plasmon resonances, which can be excited in metal nanoparticles by electromagnetic waves. The resonances lead to an intense electric field enhancement inside and in the near surrounding of the metal nanoparticles. This fact made scientists from the start to envision enhanced conversion efficiencies on the nanoscale for nonlinear optical effects.

In this chapter the nonlinear optical properties of various complex plasmonic nanostructure arrays are investigated. In the following sections nonlinear optical spectroscopy at first of very basic and then of more complex plasmonic and also hybrid nanostructures is performed. In contrast to classical nonlinear optics using bulk dielectrics, usually nonlinear optics of plasmonic nanostructures is *resonant nonlinear optics*. Hence, the linear optical properties of the complex plasmonic nanostructures are highly important in order to understand the nonlinear optical response. Therefore, in advance to the nonlinear response we always first discuss the linear optical properties of each plasmonic nanostructure array. In parallel to the nonlinear spectroscopy experiments we develop simple but convincing physical models and perform full electrodynamic simulations in order to describe and understand the nonlinear optical response of the complex plasmonic

nanostructure arrays. Finally, in the last section of this chapter we present a new second harmonic measurement technique which utilizes ultrabroadband strongly chirped laser pulses and which allows for measuring the second harmonic response in principle by a single laser pulse.

4.1 PLASMONIC NANOANTENNA ARRAYS

The very first plasmonic nanostructure arrays investigated in this thesis consist of basic rod-type gold nanoantennas, which exhibit a single dipolar localized surface plasmon resonance for light polarized along their long axis. Each nanoantenna array with an area of $100 \times 100 \mu\text{m}^2$ is fabricated with standard electron beam lithography on a bare Suprasil (Heraeus) substrate, such as described in section 2.2.2. The individual rod-type antennas show a nominal height and width of 40 and 60 nm, respectively, and the antenna length is tuned among different arrays between about 200 and 250 nm. The grating period in both directions is 500 nm. Fig. 4.1(b) shows colored scanning electron micrograph (SEM) images of one particular antenna array with an antenna length of about 225 nm.

4.1.1 *Linear, Second and Third Harmonic Response of Plasmonic Nanoantenna Arrays*

In order to unravel the nonlinear optical response of the rod-type nanoantenna arrays we perform second harmonic (SH) and third harmonic (TH) spectroscopy. These experiments are realized with a high-power Yb:KGW solitary mode-locked oscillator at 44 MHz repetition rate, and which has been introduced in section 3.1. The oscillator laser pulses are coupled into a nonlinear optical fiber to generate a broad laser spectrum from below 900 to about 1200 nm. The output of the fiber is precompressed and subsequently sent into a 4-f pulse shaper with a dual mask spatial light modulator for independent amplitude and phase modulation. This system allows either the use of the complete broadband laser spectrum, which corresponds to 11.5 fs pulse duration, or the generation of sub-30 fs laser pulses with a Gaussian-like spectral shape and tunability over a spectral range of 200 nm [107].

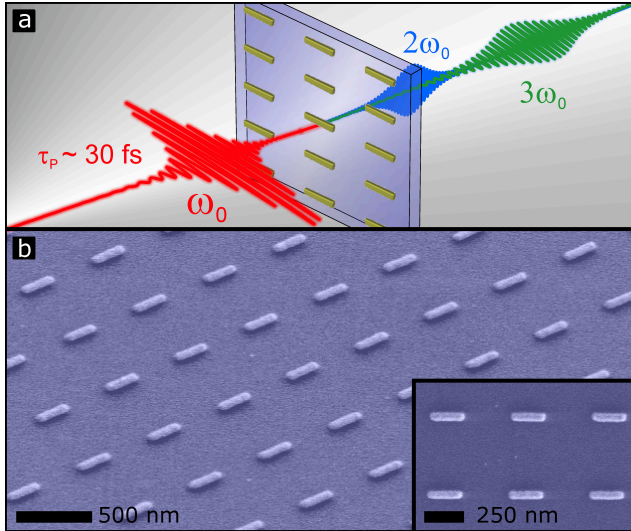


Figure 4.1: **a)** Schematic illustration of SH and TH generation in gold plasmonic nanoantennas. **b)** Colored SEM image of a nanoantenna array (45° tilted view). The inset shows a normal view.

In advance to the nonlinear spectroscopy experiments of the antenna arrays we measured their linear extinction spectrum. Therefore, the laser pulses are focused with an achromatic lens of 75 mm focal length onto the nanoantenna arrays. Subsequently, the transmitted beam is recollimated with a fused silica lens of the same refractivity. Then, the transmittance T is measured using an optical spectrum analyzer (Ando, AQ6317) and the linearly polarized broadband laser spectrum with the polarization along the antenna axis. The measured extinction spectrum $\alpha_z = -\ln(T)$ of one antenna array with an antenna length of 225 nm is exemplary depicted in Fig. 4.2(a) (black) showing a particle plasmon resonance with a central wavelength of about 1025 nm.

For the nonlinear optical experiments the same focusing and recollimation optics are used as in the linear transmittance measurements. In order to maintain a Fourier-limited pulse shape at the position of the sample the pulse shaper directly precompensates

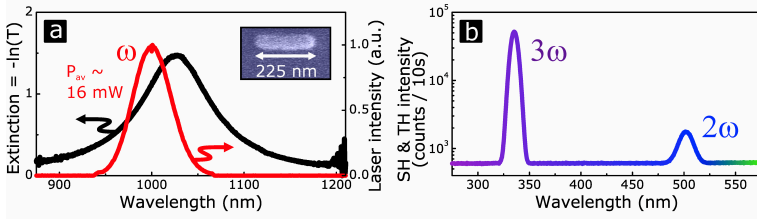


Figure 4.2: (a) Measured extinction spectrum (black) of a gold nanoantenna array with an antenna length of about 225 nm as well as measured Gaussian laser spectrum (red) at a central wavelength of about 1000 nm, which is focused on the nanoantenna array. (b) Corresponding radiated SH and TH signals, which occur at a wavelength of 500 nm and 333 nm, respectively.

sates the dispersion of the first lens. The polarization of the fundamental is again along the antenna axis. After recollimation, the fundamental laser light is filtered out by two 3 mm thick Schott KG5 filters. Subsequently, the generated SH and TH signals are detected with a liquid nitrogen cooled spectrometer.

In Fig. 4.2(a) we shaped the laser spectrum to a Gaussian-like spectral shape with a central wavelength of about 1000 nm and a bandwidth of about 45 nm. This corresponds to a Fourier-limited pulse duration of about 30 fs. Furthermore, we focused an average power of about 16 mW on the nanoantenna arrays, which corresponds to a peak intensity of about 0.5 GW/cm^2 . A corresponding measured nonlinear spectrum of the radiated nonlinear signals is shown in Fig. 4.2(b). We observe two peaks, namely at two times and three times the incoming frequency, at a wavelength of 500 nm and 333 nm, respectively, which correspond to the generated SH and TH signals. When analyzing the polarization state of the nonlinear signals we find that the generated TH in Fig. 4.2(b) exhibits the same polarization state as the incoming laser light, and hence is solely polarized parallel to the plasmonic nanoantennas. In contrast, the polarization of the SH signals is mainly oriented perpendicular to the antennas. However, also a very weak contribution polarized parallel to the antennas of the generated SH could be detected.

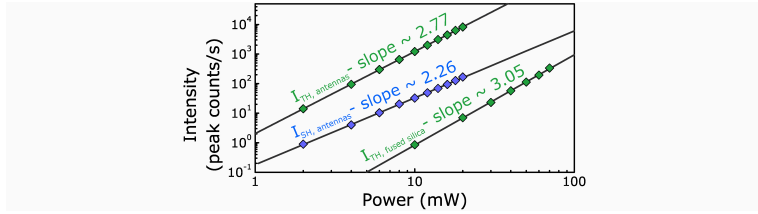


Figure 4.3: Measured peak intensities plotted over the incident average power for SH and TH generation on a plasmonic nanoantenna array with an antenna length of 225 nm as well as measured peak intensities of TH generation on a fused silica substrate.

In order to unambiguously prove that the measured nonlinear signals originate from two-photon and three-photon processes, we measured the SH and the TH signal intensity in dependence of the average input power. Hence, in Fig. 4.3 we depict the peak intensity of the measured SH and TH signals, which were generated at the nanoantenna array from Fig. 4.2, together with the peak intensity of TH signals, which were generated solely at the fused silica substrate.

In case of the TH of the fused silica substrate we find an increase of the TH intensity which is almost perfectly following the power of 3 dependence, which we determined by fitting the logarithmically plotted datapoints. Furthermore, in case of the nonlinear signals which are generated at the plasmonic nanoantenna array we find a slope of about 2.26 and 2.77 for SH and TH generation, respectively. Hence, both signals are proven to be of nonlinear origin and follow more or less the expected power of 2 and 3 dependence. Remarkably, at an average power of about 10 mW the SH signal intensity of the nanoantenna array is about an order of magnitude stronger than the TH of the fused silica substrate, but also about an order of magnitude weaker than the TH of the nanoantenna array.

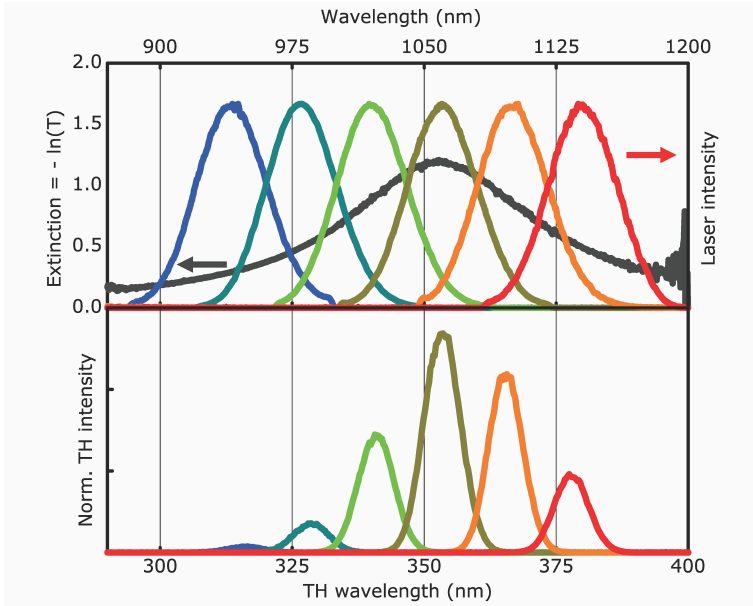


Figure 4.4: Top: Measured Gaussian laser spectra, which are used for the TH spectroscopy experiments. The laser spectrum is shifted in steps of 20 nm over the linear antenna resonance (black) and at each spectral position a TH signal is generated. Bottom: Measured normalized TH spectra. For clarity only every second laser and TH spectrum is depicted.

4.1.2 *Third Harmonic Spectroscopy of Plasmonic Nanoantenna Arrays*

In order to measure the spectral dependence of the TH generation on the nanoantenna arrays, tunable laser pulses with a narrow spectrum are required. If ultrabroadband spectra, e.g., sub-10 fs laser pulses are used, the spectral resolution in the TH response is limited. Hence, we spectrally shape our laser pulses to a Gaussian-like spectrum with an average power between 15 mW and 25 mW and a bandwidth of about 45 nm. As already mentioned above, this corresponds to a Fourier-limited pulse duration of about 30 fs. Then the central wavelength of the laser pulses

is shifted in 20 nm steps over the linear antenna resonance, and at each spectral position a TH spectrum is recorded, see Fig. 4.4. To eliminate the influence of residual dispersion and the slightly different average powers at the different spectral positions, the TH signals from the antennas are normalized to the TH from the bare fused silica substrate. Fig. 4.4 indicates that the TH generation process is most efficient close to the peak of the linear extinction spectrum.

To verify this finding we measured the linear extinction spectrum as well as the wavelength-dependent TH efficiencies on five different antenna arrays, where we increased the length of the individual antennas from 200 to 245 nm. These antenna arrays are located on three different samples. Hence, the width, the height and the quality of the antennas might differ slightly, even though they are nominally fabricated with equal parameters. The change in antenna length leads mainly to a shift of the fundamental particle plasmon resonance from about 970 to about 1100 nm. The results of these linear and nonlinear measurements are depicted in Fig. 4.5. It shows the measured TH efficiencies (green, diamonds) with respect to their corresponding linear extinction spectra (black) for the five antenna arrays. Every data point in the TH efficiency corresponds to a measured TH spectrum, which was integrated over all wavelength components and which was again normalized to the TH of the bare substrate. We find that the TH intensity generated at the antennas can be up to three orders of magnitude larger than that of the bare substrate. Furthermore, the peak of the TH generation efficiency is always slightly red-shifted with respect to the maximum of the linear extinction spectrum.

The behavior of the TH response of the plasmonic nanoantenna arrays can be modeled with an anharmonic oscillator model [16, 108]. Therefore, we treat the particle plasmon as a classical har-

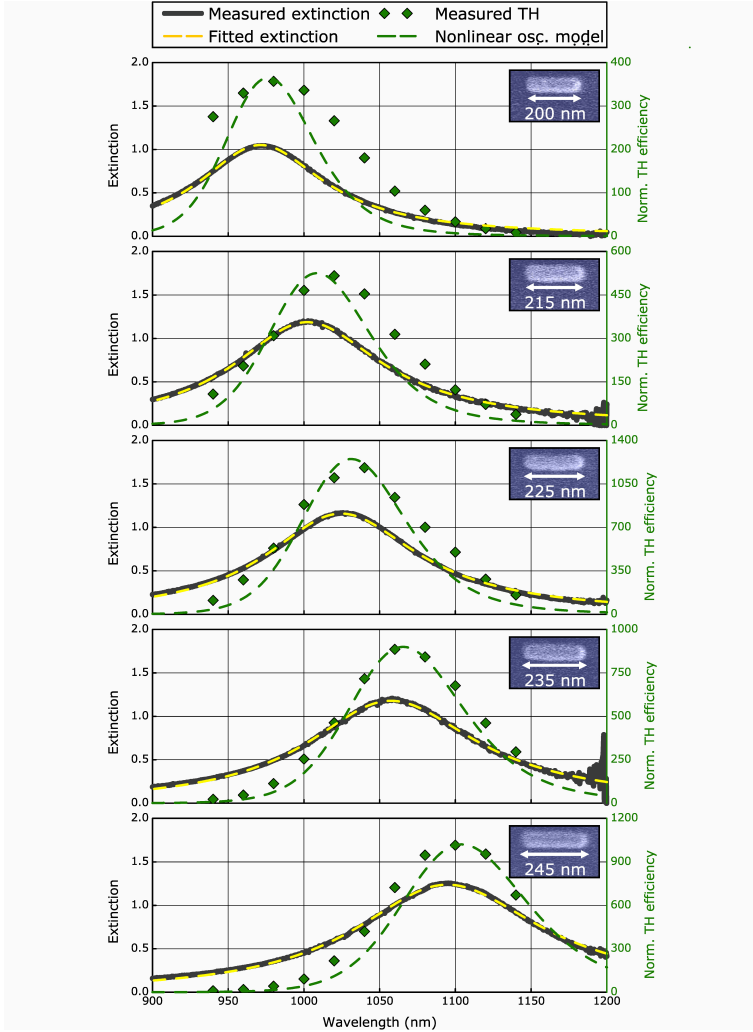


Figure 4.5: Measured and modeled normalized TH efficiencies with respect to their linear extinction spectra. From top to bottom the length of the antennas increases from 200 nm to 245 nm. The insets show colored SEM images of a single antenna element of the corresponding nanoantenna array.

monic oscillator with a small perturbation which is proportional to $[x(t)]^3$:

$$\ddot{x}(t) + 2\gamma\dot{x}(t) + \omega_0^2 x(t) + a[x(t)]^3 = -\frac{e}{m}E(t) \quad (4.1)$$

Here, $x(t)$ denotes the displacement of the localized particle plasmon, γ and ω_0 correspond to the damping constant and the resonance frequency of the unperturbed plasmonic oscillator, a is the small perturbation parameter and describes the absolute strength of the TH, e and m correspond to the charge and the mass, and $E(t)$ is the electric field of the Gaussian 30 fs laser pulses. The solution to this differential equation can be obtained using perturbation theory. Therefore, one expresses $x(t)$ in a power series for the perturbation parameter a as $x(t) = x_0(t) + a \cdot x_1(t) + \mathcal{O}(a^2)$. The first term $x_0(t)$ corresponds to the unperturbed solution while $x_1(t)$ is the first order correction which oscillates at the TH frequency. Since the solution of $x_0(t)$ is required to calculate $x_1(t)$ we first solve the unperturbed harmonic oscillation by Fourier transformation. The solution is given by

$$x_0(\omega) = -\frac{e}{m}g(\omega)E(\omega), \quad (4.2)$$

where $g(\omega) = -(\omega^2 - \omega_0^2 + 2i\gamma\omega)^{-1}$ is the linear response function of the oscillator. Such as in section 2.1.2 we can now relate the linear response function $g(\omega)$ to an effective linear optical susceptibility $\chi^{(1)}(\omega) = e^2 n / \epsilon_0 m \cdot g(\omega)$ of the nanoantenna arrays, where n corresponds to the number density of the plasmonic oscillators. Furthermore, we can derive an expression for the linear extinction coefficient $\alpha(\omega)$ using equation (2.27):

$$\alpha(\omega) = \frac{e^2 n}{\epsilon_0 c m} \frac{\gamma \omega^2}{(\omega^2 - \omega_0^2)^2 + 4\gamma^2 \omega^2} \quad (4.3)$$

The extinction spectrum, comprising absorbance and scattering, allows quantification of the interaction of the light field with the plasmonic nanoantennas. Hence, the expression for $\alpha(\omega)$ is used as a fit function for the measured extinction spectra. The fits of the extinction spectra are shown in Fig. 4.5 as well (yellow,

dashed). The good agreement between measured extinction spectra and their fits support that our particle plasmons can be well described by harmonic oscillators [109], which were also previously used in plasmonic systems [110]. From the individual fits it is possible to extract the parameters γ and ω_0 , which are the main parameters we need to calculate the unperturbed solution $x_0(t)$.

The solution for $x_1(\omega)$ can now be calculated as $x_1(\omega) = -g(\omega) \cdot \mathcal{F}[x_0(t)^3]$, where \mathcal{F} denotes a Fourier transform. The macroscopic TH polarization $P_{\text{TH}}(\omega)$, which is the source term for the TH, is directly proportional to the perturbed solution $x_1(\omega)$. Hence, the TH intensity $I_{\text{TH}}(\omega)$ radiated into the far-field is calculated as [111]:

$$I_{\text{TH}}(\omega) \sim |E_{\text{TH}}(\omega)|^2 \sim |\omega \cdot x_1(\omega)|^2 \quad (4.4)$$

If we use this model to describe the measured TH efficiencies we obtain the green dashed curves in Fig. 4.5. The anharmonic oscillator model explains the experimental behavior including the slight red-shift of the TH efficiencies with respect to the linear extinction spectra quantitatively. Basically, the physical origin of this shift is that the TH generation is most efficient when the plasmon oscillation amplitude $|x_0(\omega)|$ is largest. The peak of the plasmon oscillation amplitude is however red-shifted with respect to the linear extinction spectrum due to the damped nature of the plasmon oscillator [109]. Hence, the plasmon oscillation amplitude $|x_0(\omega)|$ does not peak at the resonance frequency ω_0 , but at the red-shifted near-field resonance frequency $\omega_{\text{NF}} = \sqrt{\omega_0^2 - 2\gamma^2}$ [2]. However, the far-field extinction spectrum $\alpha(\omega)$ (equation (4.3)) peaks independent of the damping constant γ at the resonance frequency ω_0 . Therefore, the TH efficiency peaks slightly red-shifted with respect to the linear extinction spectrum.

The only free parameter in this model is the perturbation parameter a into which information about the intrinsic bare gold

nonlinearity enters. In our case it acts as scaling parameter for the absolute TH efficiencies and is for all five antenna arrays individually scaled so that the simulation fits the measured data points best. Yet, the complete wavelength dependence of the TH efficiency is well predicted by the model.

In conclusion, we performed TH spectroscopy on plasmonic nanoantenna arrays using tunable sub-30 fs laser pulses and can quantitatively describe the experimental results with a nonlinear oscillator model. The results show that the linear resonance of the particle plasmon dominates the efficiency of the nonlinear process as well as its spectral shape. We believe that the nonlinear oscillator model can be applied to other nonlinear optical processes such as SH generation or sum frequency mixing. This finding will be of utmost importance for the design of future nanoplasmonic structures for nonlinear optics applications.

4.1.3 *Linewidth, Resonance Position and Their Influence on the Effective Plasmonic Near-Field Enhancement*

In the section above we have seen that the basic anharmonic oscillator model is able to describe the lineshape of the linear and the nonlinear optical response of plasmonic nanoantennas quite well. In contrast, we did not use the oscillator model in order to predict the absolute efficiency of the TH response, since we simply scaled the calculated TH curves to the measured ones.

However, the oscillator model can also give predictions to the overall efficiency of nonlinear optical processes, at least to some extent, which we want to illustrate in the following. In the oscillator model the source term for nonlinear optical effects is the plasmon oscillation amplitude $x_0(t)$, which is also directly related and proportional to the effective electric field enhancement inside and in the near surrounding of the plasmonic nanostructures.

Hence, here we consider the absolute value of the plasmon oscillation amplitude $|x_0(\omega)| = |g(\omega) \cdot E(\omega)|$. For continuous wave excitation with $E(t) = E_0 \cdot e^{-i\omega t}$ we obtain in the frequency domain:

$$|x_0(\omega)| = \frac{2\pi e E_0}{m} \frac{1}{\sqrt{(\omega^2 - \omega_0^2)^2 + 4\gamma^2 \omega^2}} \quad (4.5)$$

Furthermore, we have seen that the oscillator amplitude peaks at the red-shifted near-field resonance frequency $\omega_{\text{NF}} = \sqrt{\omega_0^2 - 2\gamma^2}$ [109]. Hence, its peak value calculates to

$$|x_0(\omega_{\text{NF}})| = \frac{2\pi e E_1}{m} \frac{1}{2\gamma \sqrt{\omega_0^2 - \gamma^2}} \quad (4.6)$$

$$\approx \frac{2\pi e E_1}{m} \frac{1}{2\gamma \omega_0} \sim \frac{1}{\gamma \omega_0}, \quad (4.7)$$

where we used the approximation that $\gamma \ll \omega_0$, which is very well fulfilled for our plasmonic oscillators. We find that the oscillator amplitude, or equivalently the electric near-field enhancement, is inversely proportional to the resonance frequency ω_0 as well as the damping constant γ .

At first glance it appears perhaps odd that already the resonance position ω_0 influences the absolute value of the near-field enhancement. However, if we remind ourselves that the resonance frequency ω_0 is directly related to the restoring force of a classical oscillator it becomes clear that a lower resonance frequency ω_0 , which also means a smaller restoring force, leads to a higher oscillation amplitude.

Furthermore, the amplitude of the oscillation increases with decreasing damping γ . Hence, a long lifetime τ or a narrow linewidth of the plasmon resonance, which are directly related quantities, as well lead to higher field enhancement [35, 112].

Finally, nonlinear optical effects typically scale with higher powers of the local near-field enhancement. For example the TH in-

tensity scales with the 6th power of the plasmon oscillation amplitude $x_0(t)$. Hence, the damping constant and the resonance frequency ω_0 enter with $1/(\gamma\omega_0)^6$ in the TH signal. We will see in section 4.4 that a shift to lower resonance frequencies ω_0 and a narrowing in the resonance linewidth indeed lead to an increased TH signal. Furthermore, already in the next section 4.2 we find that two plasmonic modes which exhibit the same damping and oscillator strength and hence differ only in their resonance frequency ω_0 , produce different strong TH signals, which can be completely understood from by the above considerations.

Of course, in the end the harmonic oscillator model is purely classical and can not replace a full quantitative electrodynamic simulation, since in real systems a number of effects take place simultaneously and are not accounted for by our simple oscillator model. However, it provides an intuitive picture on the microscopic origin and the enhancement of nonlinear optical processes in plasmonic nanostructures.

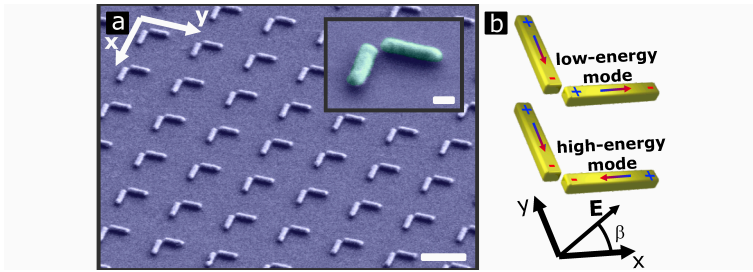


Figure 4.6: (a) SEM images of the investigated coupled plasmonic oscillator nanostructure array. The two nominally identical gold rods show a length, width and height of about 220, 60 and 40 nm, respectively. The gap distance is about 10 nm. The scale bar is 500 and 100 nm in the overview and in the inset, respectively. (b) Schematic illustration of the plasmonic eigenmodes in the coupled plasmonic oscillators. The coordinate system at the bottom defines the angle β , which is the angle between the x-direction and the electric field polarization vector.

4.2 TWO COUPLED PLASMONIC OSCILLATORS

In this section the linear and the nonlinear optical properties of more complex plasmonic nanostructure arrays are investigated, which consist of two orthogonally coupled plasmonic oscillators. The results show that even such complex plasmonic structures can be described and understood from classical coupled anharmonic oscillators and furthermore, the understanding of the microscopic processes in these coupled nanostructures is the key for developing complex plasmonic nanostructures with further enhanced conversion efficiencies in nonlinear optical effects.

The investigated nanostructures have been fabricated via electron beam lithography on a fused silica substrate and consist of arrays with an area of $100 \times 100 \mu\text{m}^2$ of two orthogonal oriented gold nanorods, see the SEM image in Fig. 4.6(a). The two nominally identical gold nanorods show a length, width and height of about 220, 60 and 40 nm, respectively, and the gap distance, which describes the shortest distance between the two gold

nanorods, is on the order of only about 10 nm. The lattice constant in both directions is 600 nm.

4.2.1 *Linear Optical Response of Coupled Plasmonic Oscillators*

In order to understand and describe the nonlinear optical response of our orthogonally coupled plasmonic oscillators we first discuss their linear optical properties. Both gold nanorods exhibit a longitudinal dipolar localized surface plasmon resonance, which can be resonantly excited in the gold nanorods by electromagnetic plane waves [34, 113]. However, owing to the small gap of about only 10 nm between the two nanorods the plasmonic modes exchange energy via their optical near-fields. Hence, the two plasmonic modes couple, hybridize and form two new eigenmodes at lower and higher resonance frequencies, with antisymmetric and symmetric charge oscillations, respectively [36, 37], see also Fig. 4.6(b).

When light polarized along an angle β of -45° or $+45^\circ$ (see Fig. 4.6(b)) is directed on the nanostructures only the lower or the higher energy mode is excited, respectively. In contrast, if the incoming polarization is oriented at an arbitrary angle β , for example also along one of the nanorods ($\beta = 0^\circ$), then a superposition of the two eigenmodes gets excited. For a polarization angle β of 0° , -45° and $+45^\circ$ we measured the transmittance spectra T , the reflectance spectra R and calculated via $T + R + A = 1$ the absorbance spectra A of the nanostructure array.

The corresponding spectra are shown in Fig. 4.7(a-c). First, in Fig. 4.7(a) for excitation under a polarization angle β of $+45^\circ$ and -45° we observe in both spectra a single extinction peak of the corresponding eigenmode at a wavelength of about 985 and 1140 nm, respectively. It is noteworthy that the extinction peaks differ slightly in their absolute peak value. Furthermore, for excitation under an angle β of 0° both extinction peaks can

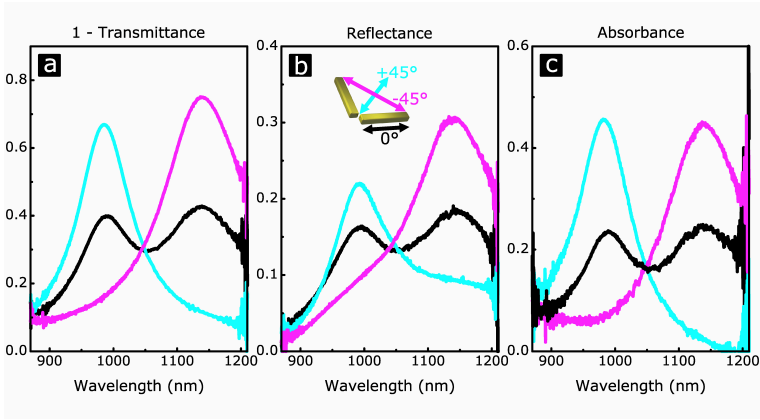


Figure 4.7: Measured 1-transmittance (a), reflectance (b) and absorbance (c) spectra for excitation under different polarization directions (0° (black), $+45^\circ$ (cyan), -45° (magenta)).

be observed due to the superposition of the two excited eigenmodes. Second, the reflectance and absorbance spectra in Fig. 4.7(b,c) show very similar behaviour for the three different light polarizations as the transmittance spectra in Fig. 4.7(a). However, in the reflectance spectra the different peak values of the scattering peaks are even more pronounced. In contrast, in the absorbance spectra the two absorbance peaks of the eigenmodes show about the same peak value. Hence, the different peak values in the transmittance spectra are caused by different scattering of the two eigenmodes, while the peak absorbance of the eigenmodes is almost identical.

In order to predict the nonlinear optical response of the nanostructures we now first develop a model for their linear optical properties, which is again based on harmonic oscillators:

$$\ddot{x}_0 + 2\gamma\dot{x}_0 + \omega_0^2 x_0 + \kappa \cdot y_0 = -\frac{e}{m} E_x(t) \quad (4.8)$$

$$\ddot{y}_0 + 2\gamma\dot{y}_0 + \omega_0^2 y_0 + \kappa \cdot x_0 = -\frac{e}{m} E_y(t), \quad (4.9)$$

where

x_0, y_0	displacement of the plasmonic modes
γ	damping constant
ω_0	resonance frequency
κ	coupling constant
e	charge
m	mass
$E_x(t), E_y(t)$	external electric field

Hence, we describe the two plasmonic modes by two identical classical coupled oscillators. The solution to these coupled differential equations can be found by Fourier transformation [24]. In the frequency domain and in matrix notation the two equations can be written as:

$$\underbrace{\begin{bmatrix} 1/g & \kappa \\ \kappa & 1/g \end{bmatrix}}_M \underbrace{\begin{bmatrix} x_0 \\ y_0 \end{bmatrix}}_{\mathbf{x}_0(\omega)} = -\frac{e}{m} \underbrace{\begin{bmatrix} E_x(\omega) \\ E_y(\omega) \end{bmatrix}}_{\mathbf{E}(\omega)}, \quad (4.10)$$

where $g = -1/(\omega^2 - \omega_0^2 + 2i\gamma\omega)$ is the linear response function of an individual plasmonic oscillator.

In order to solve the system of equations (4.10) we could either simply invert the matrix M , or we could transform to new coordinates \mathbf{x}_d , in which the matrix M exhibits only nonzero values on the diagonal, since then the solution is trivial [24]. The latter also directly delivers the eigenmodes of the system. Hence, it is carried out here.

The transformation to the new coordinates is performed by inserting the ansatz $\mathbf{x}_0 = Q\mathbf{x}_d$ into the system of equations (4.10), where Q is the transformation matrix, and by an additional multiplication with the inverse of Q :

$$\underbrace{Q^{-1}MQ}_{D} \mathbf{x}_d = -\frac{e}{m} \underbrace{Q^{-1}\mathbf{E}}_{\mathbf{E}_d} \quad (4.11)$$

$$\Rightarrow \mathbf{x}_d = -\frac{e}{m} D^{-1} \mathbf{E}_d \quad (4.12)$$

Here $D = Q^{-1}MQ$ is the diagonal matrix, which corresponds to the matrix M represented in the new coordinates \mathbf{x}_d . Furthermore, $\mathbf{E}_d = Q^{-1}\mathbf{E}$ is the external electric field in the new coordinates. In order to determine the matrices Q and D we first have to determine the eigenvalues λ of the matrix M , which are:

$$\lambda_l = \frac{1}{g} - \kappa \quad (4.13)$$

$$\lambda_h = \frac{1}{g} + \kappa, \quad (4.14)$$

where the indices l and h denote the lower and the higher energy mode, respectively. When inserting the linear response function g into the two eigenvalues λ_l and λ_h we see that

$$\lambda_{l,h} = -(\omega^2 - (\omega_0^2 \mp \kappa) + 2i\gamma\omega), \quad (4.15)$$

which shows that we obtain two new eigenfrequencies at $\omega_l = \sqrt{\omega_0^2 - \kappa}$ and $\omega_h = \sqrt{\omega_0^2 + \kappa}$. Furthermore, the normalized eigenvectors \mathbf{u}_l and \mathbf{u}_h calculate to:

$$\mathbf{u}_l = \frac{1}{\sqrt{2}} \begin{bmatrix} 1 \\ -1 \end{bmatrix} \quad (4.16)$$

$$\mathbf{u}_h = \frac{1}{\sqrt{2}} \begin{bmatrix} 1 \\ 1 \end{bmatrix} \quad (4.17)$$

The eigenvectors point along $\pm 45^\circ$ and hence along our measured eigenmodes. The transformation matrix Q , which contains the eigenvectors \mathbf{u}_l and \mathbf{u}_h , is given by:

$$Q = [\mathbf{u}_l, \mathbf{u}_h] = \frac{1}{\sqrt{2}} \begin{bmatrix} 1 & 1 \\ -1 & 1 \end{bmatrix}, \quad (4.18)$$

Furthermore, on the diagonal entries the diagonal matrix D consists of the eigenvalues λ_l and λ_h and can be calculated by [24]

$$D = Q^{-1}MQ = \begin{bmatrix} \lambda_l & 0 \\ 0 & \lambda_h \end{bmatrix}, \quad (4.19)$$

Finally, in order to determine a solution for the coordinates \mathbf{x}_d we only need to inverse the diagonal matrix D :

$$D^{-1} = \begin{bmatrix} \frac{1}{\lambda_l} & 0 \\ 0 & \frac{1}{\lambda_h} \end{bmatrix} = \begin{bmatrix} g_l & 0 \\ 0 & g_h \end{bmatrix}, \quad (4.20)$$

where $g_{l,h} = -1/(\omega^2 - \omega_{l,h}^2 + 2i\gamma\omega)$ are the linear response functions of the lower and the higher energy mode, respectively. Note that they exhibit the same mathematical form as the linear response function g of the original oscillators, but with the resonance frequency ω_0 replaced by the new eigenfrequencies ω_l and ω_h . In particular the damping constant γ remains the same for the two normal modes.

In the following we relate the solution for the plasmonic oscillations as in the Lorentz model [2] to an effective polarization \mathbf{P} so that we can determine a formula for the measured absorbance spectra A :

$$\mathbf{P} = \epsilon_0 \chi^{(1)} \mathbf{E} = -en\mathbf{x}_0 \quad (4.21)$$

$$\underbrace{Q^{-1}\mathbf{P}}_{\mathbf{P}_d} = \epsilon_0 \underbrace{Q^{-1}\chi^{(1)}Q}_{\chi_d^{(1)}} \underbrace{Q^{-1}\mathbf{E}}_{\mathbf{E}_d} = -en\mathbf{x}_d \quad (4.22)$$

Here, $\chi^{(1)}$ is the effective linear susceptibility tensor and n the number density of the plasmonic oscillators. Furthermore, we again transformed to the new coordinates by a multiplication with Q^{-1} . As before, the index d always denotes a physical quantity in the new diagonal coordinates \mathbf{x}_d .

In the next step we insert the solution for \mathbf{x}_d from equation (4.12) into equation (4.22), which allows to determine the linear optical susceptibility tensor $\chi_d^{(1)}$ in the new coordinates:

$$\mathbf{P}_d = \epsilon_0 \chi_d^{(1)} \mathbf{E}_d = \frac{e^2 n}{m} D^{-1} \mathbf{E}_d \quad (4.23)$$

$$\Rightarrow \boxed{\chi_d^{(1)} = \frac{e^2 n}{\epsilon_0 m} D^{-1}} \quad (4.24)$$

Hence, the linear optical susceptibility tensor $\chi_d^{(1)}$ is directly proportional to the inverse of the diagonal matrix D and therefore exhibits in the new coordinates also only nonzero values on the diagonal.

Ultimately, the linear optical susceptibility tensor $\chi_d^{(1)}$, which we just derived from our model, needs to be associated to measurable quantities, which are the measured transmittance, reflectance and absorbance spectra. In particular, the absorbance A can be related to the absolute extinction α_z :

$$A = 1 - \frac{I}{I_0} = 1 - e^{-\alpha z} \approx \alpha z \quad (4.25)$$

For the last approximation sign we made the assumption that absorbance is small in our system. Hence, using equation (2.27) the absorbance A is given by:

$$A = \frac{\omega}{c} \text{Im} \left[\chi_d^{(1)} \right] \quad (4.26)$$

In order to calculate the absorbance A of the lower and the higher energy mode, the (1,1) and the (2,2) component of the susceptibility tensor $\chi_d^{(1)}$ have to be evaluated in equation (4.26), respectively. The absorbance A for excitation of the nanostructure array under a polarization angle β of 0° can be determined by transforming the linear optical susceptibility $\chi_d^{(1)}$ back to the original coordinate system:

$$\chi^{(1)} = Q \chi_d^{(1)} Q^{-1} \quad (4.27)$$

The absorbance A for the light polarization along one of the two nanorods is then analogously determined from the diagonal entries in $\chi^{(1)}$ and equation (4.26).

In general, the absorbance spectrum A for excitation under an arbitrary light polarization angle β can be calculated by rotating the coordinate system by the corresponding angle [24]:

$$\chi_\beta^{(1)} = \mathbf{R}_\beta^{-1} \chi^{(1)} \mathbf{R}_\beta, \quad (4.28)$$

$$\text{with } \mathbf{R}_\beta = \begin{bmatrix} \cos \beta & \sin \beta \\ -\sin \beta & \cos \beta \end{bmatrix}, \quad (4.29)$$

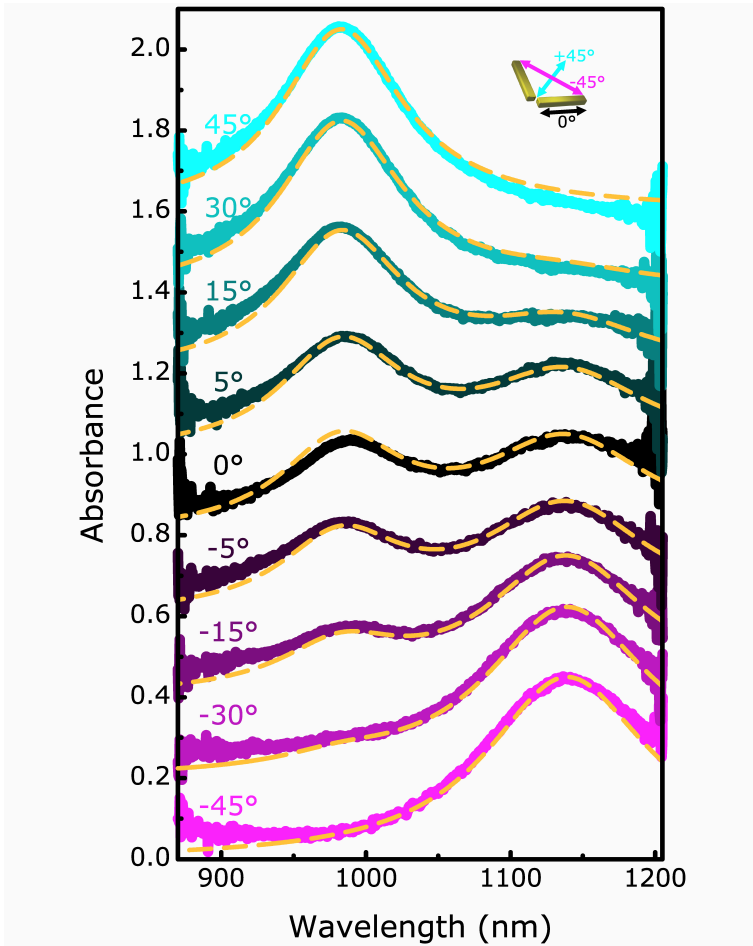


Figure 4.8: Measured and modeled absorbance spectra for excitation under different polarization directions.

where $\chi_{\beta}^{(1)}$ is the linear optical susceptibility tensor represented in the coordinate system which is rotated by the angle β relative to the original coordinate system. Furthermore, R_{β} is the rotation matrix which allows for rotating the coordinate system by the angle β .

In Fig. 4.8 measured absorbance spectra for different incoming light polarizations are shown. We fitted the two absorbance spectra of the two normal modes, which we measured under excitation of $\pm 45^{\circ}$, with the formula from equation (4.26). The free fitting parameters are the original particle plasmon resonance frequency ω_0 , the damping constant γ , the coupling coefficient κ and an overall amplitude. Hereby, the linear optical properties of the system are entirely set and the absorbance spectra A for different light polarization angles β can be calculated via the above explained procedure. The corresponding modeled absorbance spectra (yellow, dashed) for several light polarization angles β are shown in Fig. 4.8 together with corresponding measured absorbance spectra.

Hence, the polarization-resolved linear optical response of the orthogonally coupled plasmonic oscillator arrays can be modeled and understood with our classical coupled oscillator model. In the subsequent section we will see that the model even allows to predict the intensity and the polarization state of emitted TH signals for any incoming polarization angle β of the fundamental exciting laser light.

4.2.2 *Third Harmonic Spectroscopy and Modeling of the Third Order Susceptibility Tensor of Coupled Plasmonic Oscillators*

In this section we investigate the nonlinear optical response of the orthogonally coupled plasmonic oscillators. In order to understand and describe the TH signals radiated from the nanostructures we have to extend the coupled oscillator model to the non-

linear regime. Furthermore, we perform polarization-resolved TH spectroscopy experiments of the plasmonic nanostructure arrays, which are in excellent agreement with our modeling.

In order to account for the TH response of the plasmonic oscillators we include in both coupled differential equations (4.8, 4.9) anharmonic terms, which are proportional to the third power of the displacement of both plasmonic oscillators [16, 110, 114]:

$$\ddot{x} + 2\gamma\dot{x} + \omega_0^2 x + \kappa \cdot y + a \cdot x^3 = -\frac{e}{m} E_x(t) \quad (4.30)$$

$$\ddot{y} + 2\gamma\dot{y} + \omega_0^2 y + \kappa \cdot x + a \cdot y^3 = -\frac{e}{m} E_y(t) \quad (4.31)$$

Here, the parameter a describes the anharmonicity of the potentials. The nonlinear coupled differential equations can be solved in perturbation theory [16, 113]. Hence, we express the displacements of the plasmonic modes $x(t)$ and $y(t)$ in power series for the perturbation parameter a

$$x(t) = x_0(t) + a \cdot x_1(t) + \mathcal{O}(a^2) \quad (4.32)$$

$$y(t) = y_0(t) + a \cdot y_1(t) + \mathcal{O}(a^2), \quad (4.33)$$

where x_0 and y_0 are the unperturbed displacements of the plasmonic oscillators and x_1 and y_1 are the first order correction to the displacements, which in particular describe the TH response. When we insert the ansatz for $x(t)$ and $y(t)$ into the anharmonic coupled differential equations (4.30, 4.31) and compare in both equations terms of the same order of the perturbation parameter a , we find for a^0 the linear coupled differential equations (4.8, 4.9) from the previous section, which very well describe the linear optical response of the plasmonic oscillators. In first order perturbation theory (a^1) we obtain

$$\dot{x}_1 + 2\gamma\dot{x}_1 + \omega_0^2 x_1 + \kappa \cdot y_1 = -x_0(t)^3 \quad (4.34)$$

$$\ddot{y}_1 + 2\gamma\dot{y}_1 + \omega_0^2 y_1 + \kappa \cdot x_1 = -y_0(t)^3 \quad (4.35)$$

On the left hand side equations (4.34, 4.35) exhibit the identical mathematical form as the equations (4.8, 4.9) of the unperturbed coupled oscillators. However, on the right hand side of both equations the solution for the displacements x_0 and y_0 of the plasmonic modes taken to the third power enter into the equations as an "external force". Hence, the displacements in first order perturbation x_1 and y_1 are driven by their respective unperturbed solutions.

When we transform to the frequency domain we can write our coupled oscillator system in first order perturbation again in a matrix representation

$$\underbrace{\begin{bmatrix} 1/g & \kappa \\ \kappa & 1/g \end{bmatrix}}_M \underbrace{\begin{bmatrix} x_1 \\ y_1 \end{bmatrix}}_{x_1(\omega)} = -\mathcal{F} \begin{bmatrix} x_0(t)^3 \\ y_0(t)^3 \end{bmatrix}, \quad (4.36)$$

where M corresponds to the oscillator matrix, which we already introduced in the previous section. Since the TH generation in fact physically takes place in the gold nanorods, this time we stay in the coordinate system of the original plasmonic modes. The solution for the first order displacements x_1 can then be found by inverting the oscillator matrix M , which is in matrix notation given by:

$$\begin{bmatrix} x_1 \\ y_1 \end{bmatrix} = - \underbrace{\frac{1}{1 - \kappa^2 g^2} \begin{bmatrix} g & -\kappa g^2 \\ -\kappa g^2 & g \end{bmatrix}}_{M^{-1}} \mathcal{F} \begin{bmatrix} x_0(t)^3 \\ y_0(t)^3 \end{bmatrix} \quad (4.37)$$

Here, the various matrix components of the inverse matrix M^{-1} describe different physical processes, which we would like to discuss briefly.

First, the two diagonal entries weight $x_0(t)^3$ and $y_0(t)^3$, which oscillate at the TH frequency, with the linear response function g of the original plasmonic oscillators. Unfortunately, in our case the gold nanorods do not exhibit a plasmonic resonance at the TH frequency and therefore the response function g is close to zero and also spectrally flat at the TH. However, if the nanorods would not only exhibit a plasmonic resonance at the fundamental laser wavelength, but also at the TH frequency, this term could tremendously enhance the TH generation.

Second, the non-diagonal entries describe the transfer of TH energy from one gold nanorod to the other. Therefore, the transferred TH is multiplied with a factor of $-\kappa g^2$. Here, the response function g enters once for the plasmonic mode where the TH is generated and once for the nanorod to which it is transferred. Of course, the coupling coefficient κ accounts for the overall efficiency of the TH energy transfer.

Again, the response function g at the TH frequency is in our case small and spectrally flat, what means that $-\kappa g^2 \ll g$. Therefore, the non-diagonal entries, which describe the transfer of TH energy from one gold nanorod to the other, are in our case negligible compared to the diagonal entries. Since the linear response function g and also the other prefactors of the inverse matrix M^{-1} are at the TH spectrally flat, we calculate the displacements in first order simply as $x_1(\omega) \sim \mathcal{F}[x(t)^3]$. Finally, the TH electric field amplitude radiated into the far-field is given by $E_{\text{TH}}(\omega) \sim -i\omega x_1(\omega)$ [113, 115].

In order to test if the anharmonic coupled oscillator model is able to describe the nonlinear optical response of the coupled plasmonic oscillators we perform polarization-resolved TH spectroscopy of the nanostructures. Hence, we focus sub-30 fs laser

pulses tunable from 900 to 1200 nm with a 75 mm focal length achromatic lens on the nanostructure arrays [107, 113]. Subsequently, we collect the TH signals radiated in forward direction with a fused silica lens, send them through an analyzer, filter the signals from the fundamental laser light and measure these with a Peltier-cooled CCD camera attached to a spectrometer. To eliminate the influence of any wavelength-dependent components in our experimental setup we normalize all TH signals radiated from the nanostructures to TH signals, which we generate at a 20 nm thick gold film in transmission (see Fig. A1 in the appendix). Hereby, we as well eliminate any wavelength-dependence of the third-order susceptibility of the bare gold, which is not accounted for in our modeling. Furthermore, all measured TH spectra are integrated over all wavelength components yielding a scalar value, which describes the radiated TH intensity.

The results of the TH spectroscopy experiments are shown in Fig. 4.9 in the left column. We plot the measured and polarization-resolved TH intensities (diamonds) over the fundamental exciting laser wavelength together with the corresponding measured absorbance spectra. Furthermore, the corresponding modeling with the above introduced coupled anharmonic oscillator model is shown in the right column.

In the first row the absorbance spectrum for excitation under an angle β of $+45^\circ$ (cyan) and the corresponding TH spectra, which were measured under an analyzer angle of -45° (magenta) and $+45^\circ$ (cyan), are shown. We find the contribution of the radiated TH intensity, which is polarized parallel to the fundamental laser light, peaking close to the higher energy mode resonance frequency ω_n . Furthermore, perpendicular to the incoming polarization direction, namely at a TH polarization angle of -45° , only very weak TH signals can be detected. These remaining TH signals are probably due to small structure imperfections and alignment uncertainties of the polarizer and the analyzer in the experimental setup.

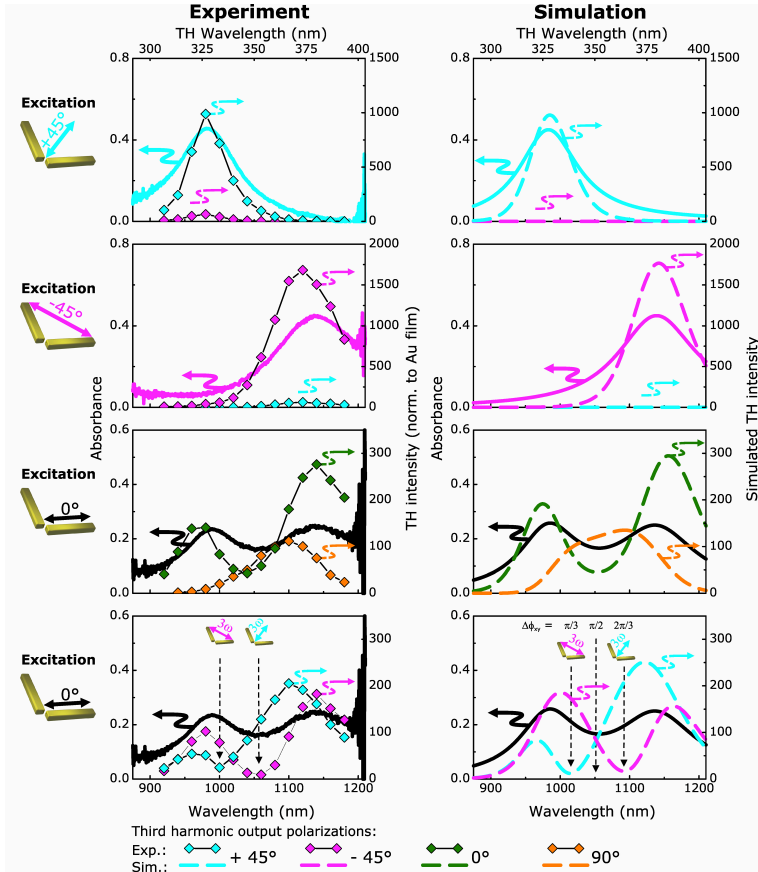


Figure 4.9: Experimental (left) and simulated (right) absorbance spectra as well as polarization-resolved TH spectra plotted over the fundamental excitation wavelength. The top axis shows the TH wavelength. The first and second row show excitation under $+45^\circ$ and -45° , respectively, the third and fourth row both show the results for excitation under 0° , but with different output polarizations of the TH light.

In the second row analogously we plot the absorbance spectrum for excitation under -45° as well as the corresponding radiated TH intensities. As before, we only find a pronounced TH signal in the polarization direction which is oriented parallel to the fundamental exciting laser polarization and it peaks close to the excited lower energy mode resonance frequency ω_1 .

Hence, if one of the two eigenmodes of the nanostructures is excited by the fundamental laser light individually, no nonlinear polarization conversion takes place. Therefore, the radiated TH signals at 3ω exhibit the identical polarization state as the incoming laser light at frequency ω .

In the third row the absorbance spectrum for excitation under 0° (black) together with the corresponding TH spectra which were measured under an analyzer angle of 0° (green) and $+90^\circ$ (orange) are shown. The TH spectrum polarized parallel to the exciting laser light exhibits two peaks due to the excitation of the two eigenmodes. Furthermore, in contrast to the excitation along the normal modes, here nonlinear polarization conversion of the TH can be observed. Hence, we also measure efficient radiation of TH intensity perpendicular to the exciting laser light, which spectrally peaks in between the two eigenmodes and close to the original resonance frequency ω_0 . This TH polarization contribution is generated at and radiated from the second perpendicular oriented gold nanorod, which gets resonantly excited at its resonance frequency ω_0 by the plasmonic mode in the first nanorod.

Finally, in the fourth row we again consider the case for excitation along one of the gold nanorods. Hence, the same absorbance spectrum as in the third row for excitation under 0° is shown. However, here we analyze the radiated TH signals along the polarization directions of the eigenmodes, namely along -45° (magenta) and $+45^\circ$ (cyan). Therefore, the measured TH spectra are a result of the interference of the TH signals radiated from both nanorods. In the TH spectra we can identify two spectral positions (lying symmetrically around ω_0) at which the TH sig-

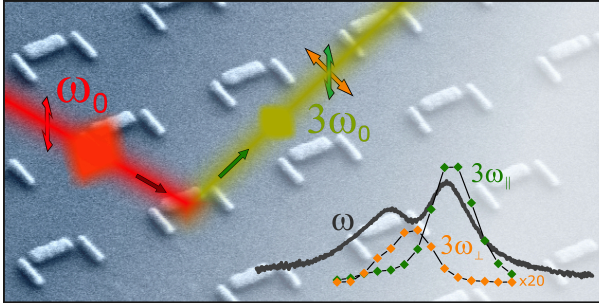
nal in one polarization component approaches zero. At these spectral positions the TH is purely polarized in one of the normal mode polarization directions. In order to understand that fact, we have to remind ourselves that for an excitation frequency ω much smaller than the resonance frequency ω_0 the two plasmonic modes of the two gold nanorods will oscillate completely out of phase, similar to the charge distribution of the lower energy mode, but with different amplitudes. This means that the phase difference $\Delta\Phi_{xy}$ between both plasmonic oscillators will be π . In contrast, for an excitation frequency ω much larger than the resonance frequency ω_0 both oscillators will oscillate in phase. Hence, over the entire resonance the phase difference $\Delta\Phi_{xy}$ between the two plasmonic modes varies between 0 and π and accounts at the resonance frequency ω_0 exactly to $\pi/2$.

However, if the phase difference $\Delta\Phi_{xy}$ between the two plasmonic oscillators varies over π this means that the phase difference $\Delta\Phi_{TH}$ of the TH signals, which are generated in the two nanorods, will vary at the same time over 3π . Hence, for a phase difference $\Delta\Phi_{xy}$ of the plasmonic oscillators of $\pi/3$ or $2\pi/3$ the x- and y-component of the TH signals will exhibit a phase difference $\Delta\Phi_{TH}$ of π or 2π , respectively. Therefore, at slightly shorter and longer wavelength than the resonance frequency ω_0 where the phase difference $\Delta\Phi_{xy}$ of the plasmonic modes accounts to $\pi/3$ and $2\pi/3$ the generated TH signals will oscillate in a polarization state parallel to the lower and higher energy mode, respectively.

Remarkably, the simulated TH spectra shown in the right column of Fig. 4.9 are able to capture all features of the measured and radiated TH spectra. Hence, the anharmonic coupled oscillator model allows for understanding and describing the linear and the nonlinear optical properties of the coupled plasmonic oscillators. In particular, the intensities of the radiated TH signals are modeled and predicted, since all displayed TH spectra are scaled with only one global parameter to the measured ones. Therefore, we can even understand why the excitation of the lower energy mode in the second row produces stronger TH than the excita-

tion of the higher energy mode in the first row. The two normal modes only differ in their eigenfrequency, since they exhibit equal damping and oscillator strength. The lower eigenfrequency ω_1 of the lower energy mode corresponds to a smaller restoring force and therefore a larger oscillator amplitude and finally this leads to the stronger generation of TH light.

In conclusion, we performed polarization-resolved TH spectroscopy of orthogonally oriented coupled plasmonic oscillators. The linear and the nonlinear optical response of these can entirely be understood and described from a classical coupled anharmonic oscillator model. We find that when solely a single eigenmode of the nanostructure system is excited no nonlinear polarization conversion takes place, which means that the generated TH signals exhibit the same polarization state as the incoming laser light. Furthermore, the lower energy mode exhibits due to the smaller eigenfrequency ω_1 a slightly higher near-field amplitude, which leads to more efficient generation of TH light. The interference of the generated TH signals from both nanorods shows that the phase difference in the TH varies over the entire plasmonic resonance over 3π .



4.3 COMPLEX PLASMONIC FANO STRUCTURES

Plasmonic nanostructures are attractive for nonlinear optics as they resonantly enhance nonlinear effects on the nanoscale [106]. In the last years, scientists just started to design complex plasmonic nanostructures to amplify nonlinear optical processes, such as second and third harmonic (TH) generation or four wave mixing by using doubly-resonant or multiresonant antennas [116–119] or plasmonic Fano resonances [120–122]. The latter mainly benefit from a narrow subradiant linewidth, which renders them highly attractive for enhanced optical nonlinearities [123, 124]. Recently, a number of detailed studies of the nonlinear optical response of metal nanostructures have been carried out [108, 110, 113, 125–130]. Despite the variety of sophisticated experiments, the microscopic source of the nonlinear response has not been answered conclusively [114, 131]. Furthermore, if and under which conditions plasmonic Fano resonances allow for more efficient nonlinear light generation is still under discussion. In this section we examine the origin of the nonlinear response of complex plasmonic Fano resonances by polarization-resolved TH spectroscopy of gold dolmen-type nanostructure arrays [132–134], see Fig. 4.10(a). Our results indicate whether it is possible to further enhance nonlinear optical processes using plasmonic Fano resonances and allow drawing conclusions on the source of the TH response.

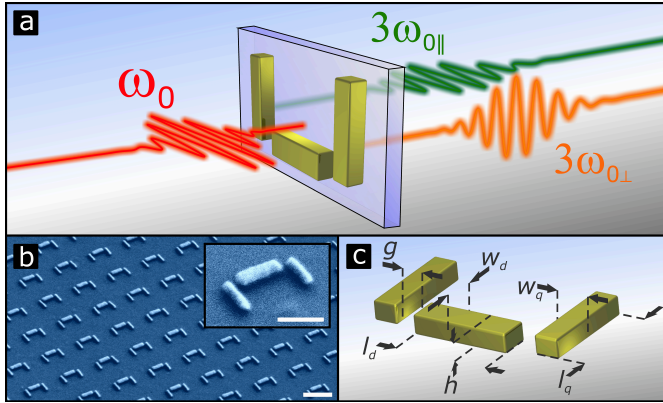


Figure 4.10: (a) Illustration of TH spectroscopy of plasmonic Fano structures. (b) Tilted SEM images of the samples. The scale bars are 500 nm and 200 nm in the overview and the inset, respectively. (c) Geometrical parameters of the dolmen-type nanostructures: $l_d = 220$ nm, $w_d = 70$ nm, $l_q = 190$ nm, $w_q = 50$ nm, $g = 40 - 60$ nm, $h = 60$ nm. The lattice constants of the nanostructure arrays are 600 and 700 nm perpendicular and parallel to the dipole rod, respectively.

4.3.1 Third Harmonic Mechanism in Dolmen-Type Complex Plasmonic Fano Structures

The investigated gold nanostructure arrays with an area of $100 \times 100 \mu\text{m}^2$ are fabricated via electron beam lithography on a fused silica substrate. The dolmen-type structures consist of a dipole rod placed between two orthogonal oriented dipole rods. In Fig. 4.10(b) tilted scanning electron micrographs (SEM) of the fabricated nanostructures are shown. Fig. 4.10(c) depicts the corresponding geometrical parameters.

Particle plasmons are excited when illuminating the nanostructures with light polarized parallel to the single dipole. Simultaneously energy is exchanged via the optical near-fields between the dipole and the perpendicularly oriented gold rods. Due to the out-of-phase oscillation of the perpendicularly oriented

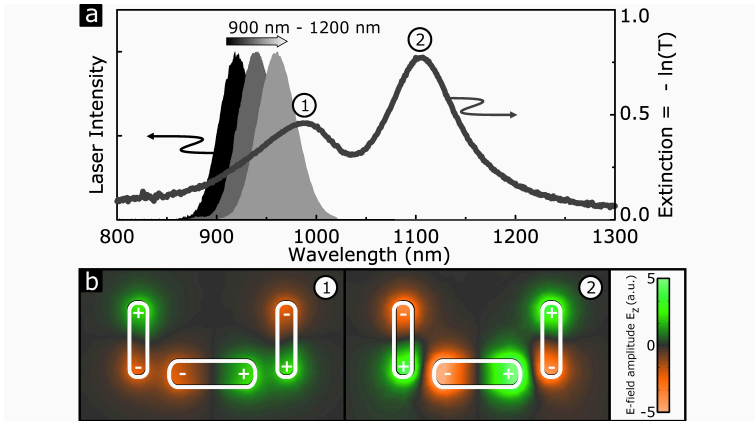


Figure 4.11: (a) Measured extinction spectrum of a dolmen-type nanostructure array as well as experimental laser spectra, which are tuned over the Fano resonance to measure the TH spectrum of the structure. (b) Simulations of the z-component (normal to the substrate) of the electric near-field amplitude 20 nm above the structure at the two spectral positions marked in (a).

rods they form a subradiant quadrupolar mode. The interference of the bright dipole and the dark quadrupole mode leads to the typical Fano lineshape in the linear extinction spectrum as shown in Fig. 4.11(a), which is characterized by a spectrally narrow transmittance window within a broad absorbance peak [45, 123, 132, 133, 135]. The Fano interference results in the formation of two distinct absorption peaks. In Fig. 4.11(b) the z-components of the electric near-field at the far-field spectral positions of the two peaks are depicted, which were simulated using finite element methods (FEM) (Comsol Multiphysics). The near-fields show antisymmetric and symmetric electric field distributions, with repulsive and attractive interaction at the gap region of the structure, respectively.

In order to unravel the nonlinear optical response of the dolmen-type structures we perform polarization-resolved TH spectroscopy experiments. We focus sub-30 fs laser pulses with an average power of about 15 mW, tunable from 900 to 1200 nm (Fig. 4.11(a))

from an amplitude and phase adjustable pulse shaper [107], with a 75 mm focal length achromatic lens on the nanostructure arrays. This leads to a beam diameter in the focus of about $50\ \mu\text{m}$ and to peak intensities on the order of about $0.5\ \text{GW}/\text{cm}^2$. A factor of two to three above these light intensities we could observe slight changes in the linear optical spectra, in particular after long exposure times. Hence, the damage threshold for the resonantly excited gold nanostructures is located close or slightly above a peak intensity of about $1\ \text{GW}/\text{cm}^2$. In order to position the nanostructure arrays in the focus of the exciting laser light, the sample is mounted on an xyz-translation stage. Throughout the manuscript the polarization of the incoming laser light is oriented along the dipole. The TH signals, which are radiated in forward direction, are recollimated with a fused silica lens of the same focal length. Hence, we only collect the zeroth diffraction order of the radiated TH signals, although higher diffraction orders are allowed at the TH frequency, which is located in the ultraviolet, due to the lattice constants of 600 and 700 nm of the nanostructure arrays. Subsequently, the TH signals are analyzed by a polarizer and measured with a Peltier cooled CCD camera attached to a spectrometer.

The experimental results of the TH spectroscopy measurements are shown in Fig. 4.12 in the left column. To examine the influence of the quadrupole on the TH response we varied the gap distance g between the dipole and the quadrupole rods from about 60 nm to about 40 nm from top to bottom. Even though the difference in the gap distance g is relatively small, the increased coupling is clearly visible in the measured linear extinction spectra as more pronounced splitting of the Fano resonance peaks. In addition to the linear extinction spectra the integrated TH intensities are depicted over the fundamental wavelength as datapoints (polarizations: green: \parallel dipole, orange: \perp dipole). The TH polarized parallel to the dipole is found to always peak close to the low energy peak of the Fano resonance. Neither in the Fano resonance dip nor at the high energy peak strong TH emission is

observed. Perpendicular to the dipole, only very weak TH emission can be detected. For the intermediate gap distance of 50 nm the inset shows the magnified TH perpendicular to the dipole, which we find to peak close to the Fano resonance dip.

In order to unravel the underlying physical mechanisms, we describe the particle plasmons as classical coupled oscillators with a small cubic perturbation, which accounts for the TH generation [136]. Furthermore, we perform FEM simulations to gain more insight on the nonlinear light generation. Both strategies show excellent agreement with our measurements and provide complementary information on the nonlinear optical response of plasmonic nanostructures.

In the anharmonic coupled oscillator model we treat the bright mode of the dipole and the dark mode of the quadrupole rods as classical harmonic oscillators [110, 114, 134, 137]:

$$\ddot{x}_d + 2\gamma_d \dot{x}_d + \omega_d^2 x_d - \kappa \cdot x_q + \alpha \cdot x_d^3 = -\frac{e}{m} E(t) \quad (4.38)$$

$$\ddot{x}_q + 2\gamma_q \dot{x}_q + \omega_q^2 x_q - \kappa \cdot x_d + \alpha \cdot x_q^3 = 0 \quad (4.39)$$

The indices $j = d, q$ represent the dipole and the quadrupole, respectively. Here, $x_j(t)$ is the displacement of the mode, γ_j and ω_j denote its damping and its resonance frequency, κ describes the coupling strength between both modes, the small perturbation parameter α determines the absolute strength of the TH, e and m correspond to the charge and the mass of the dipole oscillator, and $E(t)$ is the electric field of the 30 fs laser pulses. Due to the relatively large gap distances of the structures we utilize a complex coupling coefficient $\kappa = |\kappa| \cdot \exp^{i\Phi}$, which accounts for the retarded interaction of both modes [138], see also section 4.3.2. The solution of the coupled differential equations can be obtained in the frequency domain using perturbation theory. The unperturbed solution for the displacements $x_{j0}(\omega)$ then follow from a matrix inversion:

$$\begin{bmatrix} x_{d0} \\ x_{q0} \end{bmatrix} = -\frac{e}{m} \frac{1}{1 - \kappa^2 g_d g_q} \begin{bmatrix} g_d & \kappa g_d g_q \\ \kappa g_d g_q & g_q \end{bmatrix} \begin{bmatrix} E(\omega) \\ 0 \end{bmatrix} \quad (4.40)$$

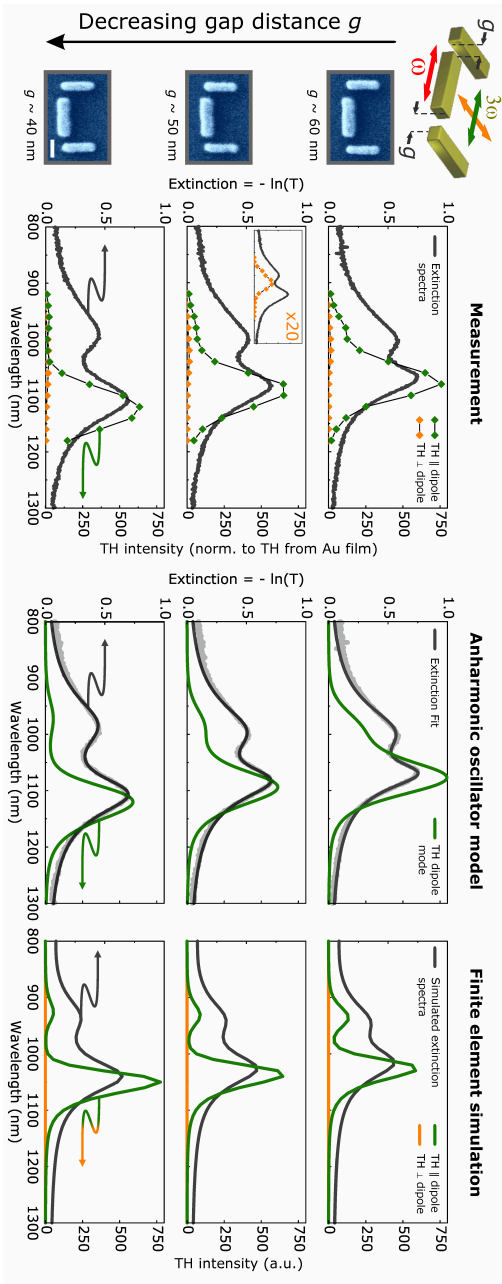


Figure 4.12: Measured, modeled and simulated TH spectra plotted together with their corresponding linear extinction spectra for decreasing gap distance g from top to bottom. On the left SEM images are depicted, respectively. The scale bar is 100 nm.

Here $g_j(\omega) = -[\omega^2 - \omega_j^2 + 2i\gamma_j\omega]^{-1}$ is the linear response function of an individual oscillator. From the solution the linear extinction $\alpha(\omega)$ for light polarized along the dipole can be derived [134, 138]:

$$\alpha(\omega) = \frac{e^2 n}{\epsilon_0 m} \frac{\omega}{c} \text{Im} \left[\frac{g_d}{1 - \kappa^2 g_d g_q} \right] \quad (4.41)$$

Fitting of the measured linear extinction spectra with the expression for $\alpha(\omega)$ yields the linear optical properties (ω_j , γ_j , κ) of the coupled oscillator system. Subsequently, the solution in first order perturbation $x_{j1}(\omega)$, which describes the TH response, can be calculated as $x_{j1}(\omega) \sim \mathcal{F}[x_{j0}(t)^3]$. In this ansatz, cross-terms, which describe the transfer of TH energy between both modes, as well as the linear response function at the TH frequency have been neglected since they are small and spectrally flat, respectively. Hence, in the oscillator model the sources of the nonlinearity are the displacements $x_{j0}(\omega)$ of the unperturbed solution. The expression for $x_{d1}(\omega)$ now allows to calculate the radiated TH from the dipole [108, 113, 115].

The results of the anharmonic coupled oscillator model are depicted in Fig. 4.12 in the center column. The TH radiated from the dipole (green) is shown together with the fitted linear extinction spectra (black). The model describes all features of the radiated TH polarized parallel to the dipole for all measured gap distances. In particular the peak position of the TH is as well found close to the low energy peak. Hence, the TH parallel to the dipole is completely described by the TH of the dipole mode. The TH from the mode of the quadrupole rods is predicted by the model to peak between the Fano resonance dip and the low energy peak (not shown). However, the oscillator model is apparently not capable to describe the “brightness” of the mode of the quadrupole rods and how efficient the mode radiates TH into the far-field. The spectral position however suggests that the

weak TH harmonic measured perpendicular to the dipole stems from the quadrupole rods. This matter will be discussed later in the manuscript.

To examine the microscopic source of the TH in more detail we also perform FEM simulations (Comsol Multiphysics) of the dolmen-type structures, whose results are shown in the right column of Fig. 4.12. In the simulations the structures are defined with the dimensions given in Fig. 4.10(c), are positioned on a substrate with a constant refractive index of $n = 1.5$, and for the optical properties of gold we use the data of Johnson and Christy [139]. For the TH spectra we calculate at each spatial coordinate inside the dolmen-type structures a local TH polarization $\mathbf{P}_{\text{THG,loc}} \sim \chi_{\text{Au}}^{(3)} \mathbf{E}_{\text{loc}}^3 \sim [\chi_{\text{Au}}^{(1)}]^3 \mathbf{E}_{\text{loc}}^3 \sim \mathbf{P}_{\text{loc}}^3$ from the complex polarization $\mathbf{P}_{\text{loc}}(\mathbf{r}, \omega)$. Here \mathbf{E}_{loc} is the complex local electric field and $\chi_{\text{Au}}^{(1)}$ and $\chi_{\text{Au}}^{(3)}$ are the first and third order susceptibilities of bare gold, respectively. After the second approximate sign, we used the classical expression of the third order susceptibility, which is proportional to the third power of the fundamental susceptibility [136] (field distributions of the TH polarization in the dolmen-type structures can be found in Fig. 4.13). Finally we integrate over the volume V of the gold structures:

$$\mathbf{E}_{\text{THG}}(\omega) \sim \omega_{\text{THG}} \int_V \mathbf{P}_{\text{loc}}(\mathbf{r}, \omega)^3 d\mathbf{r}^3 \quad (4.42)$$

In the simulation the sources of the optical nonlinearity are the local polarizations $\mathbf{P}_{\text{loc}}(\mathbf{r}, \omega)$ at each spatial coordinate \mathbf{r} in the gold structures. Since the polarization enters as a complex quantity the complete phase information is included. Thus, from the simulation we obtain the full polarization state of the complex TH electric field $\mathbf{E}_{\text{THG}}(\omega)$ radiated into the far-field. The TH spectra are then calculated as the intensity $I_{\text{THG}}(\omega)$ of the TH electric field amplitude $\mathbf{E}_{\text{THG}}(\omega)$ in the respective polarization direction. Just like the oscillator model, the simulation predicts the TH polarized parallel to the dipole to peak close to the low energy peak of the Fano resonance (green). The slight differences at the high

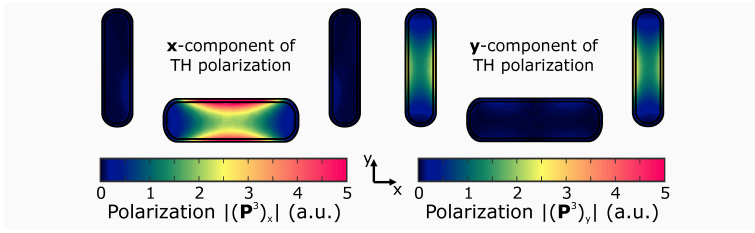


Figure 4.13: Simulated field distributions of the absolute value of the x -component (left) and the y -component (right) of the TH polarization in dolmen-type gold nanostructures with a gap distance of 50 nm, each at their corresponding spectral peak positions. Predominantly, the TH polarization which is oriented along the x -direction is located in the dipole rod, while the TH polarization which is oriented along the y -direction, is generated in the quadrupole rods. For the perfectly symmetric structure the TH in the quadrupole bars interferes destructively in the far-field, due to the antisymmetric charge oscillations.

energy peak, where the simulation shows a small peak instead of a little shoulder, mainly stems from the fact that the simulation is carried out in continuous wave excitation, which does not account for the finite spectral width of the 30 fs laser pulses. In the oscillator model, we accounted for the spectral width of about 45 nm (FWHM) of the laser pulses, which slightly blurs out the features in the TH response. Additionally, the simulation predicts zero TH signal polarized perpendicular to the dipole (orange) due to the symmetry of the structure. The small TH in this polarization direction which we observe in the experiment is most likely due to small structure imperfections.

To further examine the origin of the TH radiation polarized perpendicular to the dipole, we now shift the dipole of the structure with 50 nm gap distance in small steps from its center position closer to one of the quadrupole wires (SEM images in Fig. 4.14(a)). The introduced asymmetry leads to an unequal coupling between the dipole rod and the perpendicularly oriented rods. Hence, the two quadrupole rods are now excited with different strength and phase (due to the distance-dependent retarded coupling). Both effects render the previously dark mode of the quadrupole rods

with increased symmetry breaking more bright and dipole-like and hence lead to increased radiative damping.

The corresponding TH spectroscopy measurements are depicted in Fig. 4.14(a), where the measured TH signals polarized perpendicular to the dipole (orange) together with the measured linear extinction spectra (black) are shown, with increasing dipole offset from top to bottom. We find a monotonic increase of the TH emission with increasing dipole offset s . As before we fitted the linear extinction spectra with the coupled oscillator model and calculated subsequently the displacement $\chi_{q1}(\omega)$ describing the TH of the mode of the quadrupole rods, see Fig. 4.14(a) (orange lines). It is noteworthy that only in the fully symmetric case the plasmonic mode of the quadrupole rods is a pure quadrupolar mode. As soon as the symmetry is broken by displacing the dipole wire, the excited mode in the quadrupole rods χ_q will be a superposition of the dark quadrupolar mode and a dipole-like contribution. As mentioned before, the oscillator model does not include information about how efficient the mode of the quadrupole rods χ_q radiates TH light into the far-field. In contrast to the spectral behavior the absolute far-field TH strength is a parameter that cannot be predicted by the model. Therefore, the modeled TH spectra are scaled with respect to amplitude to the measured TH datapoints. Nevertheless, the spectral behavior and the peak position of the TH is very well predicted by our simple model.

Furthermore, we simulated the symmetry-broken dolmen-type structures with the FEM and extracted the maxima of the radiated TH intensities perpendicular to the dipole for different dipole offset s . The result is shown in Fig. 4.14(b) together with the maxima of the measured TH intensities and confirms the monotonic increase of the TH with increasing dipole offset s (see Fig. A2 in the appendix for the complete simulated TH spectra).

We conclude that for the symmetric structure the TH polarization of the mode of the quadrupole rods interferes destruc-

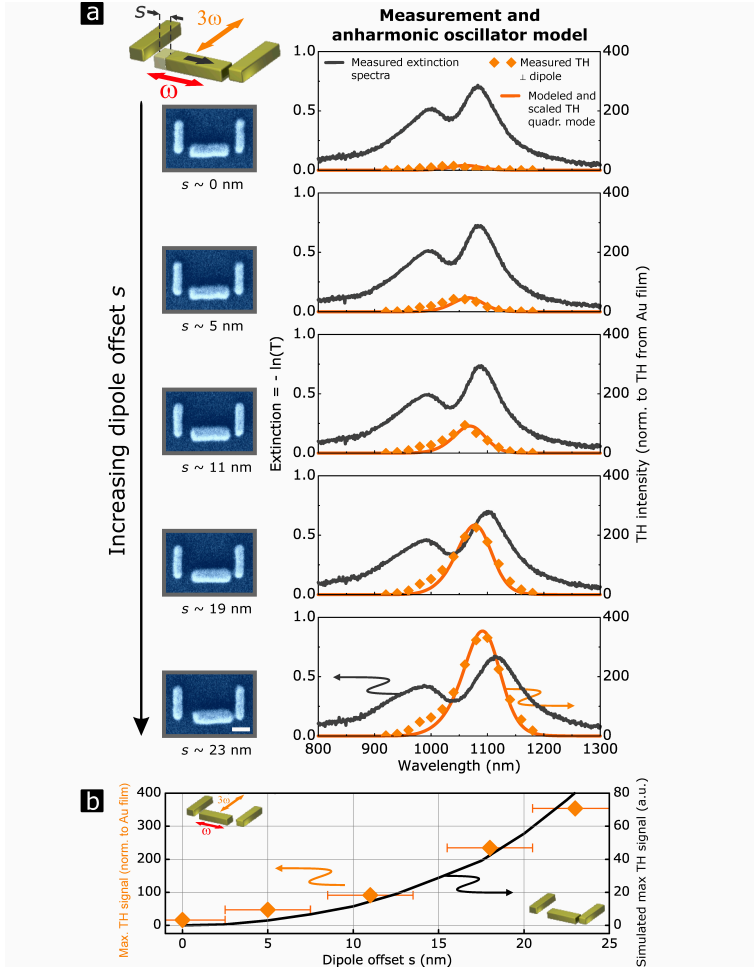


Figure 4.14: (a) Measured TH spectra polarized perpendicular to the dipole antenna for increasing dipole offset s together with corresponding linear extinction spectra from top to bottom. On the left SEM images are depicted, respectively. The scale bar is 100 nm. **(b)** Measured and simulated maximum TH efficiency perpendicular to the dipole antenna for increasing dipole offset s .

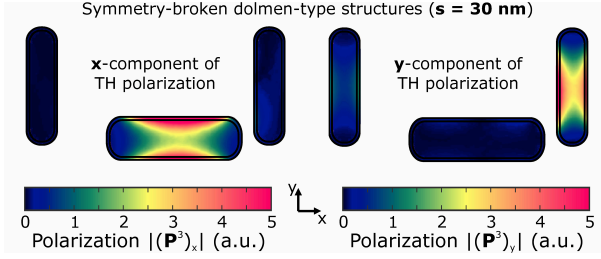


Figure 4.15: Simulated field distributions of the absolute value of the x-component (left) and the y-component (right) of the TH polarization in asymmetric dolmen-type gold nanostructures ($s = 30$ nm), each at their corresponding spectral peak positions.

tively in the far-field due to the out-of-phase oscillation in the two quadrupole wires. For increasing dipole offset s the unequal excitation of the quadrupole wires leads to reduced destructive interference and hence to efficient radiation of the TH light into the far-field.

The obtained results allow several conclusions on the TH response of plasmonic nanostructures. Our model and the simulations require a normalization of the experimental TH spectra to the off-resonant TH of a bare gold film [140]. This normalization accounts for a wavelength dependent TH response of the bare gold which is explicitly not included in our model and the simulation. We find that the TH of the bare gold changes in the considered wavelength range by about a factor of three when comparing it to the TH we obtain from a bare fused silica substrate (see Fig. A1 in the appendix). More importantly, we identify the source of the nonlinearity in the oscillator model and the simulation to be the displacement $x_{j0}(\omega)$ and the polarization $\mathbf{P}_{\text{loc}}(\mathbf{r}, \omega)$, respectively. Both are related in the Lorentz-Drude model via $\mathbf{P} = -en_e \cdot \mathbf{x}$, and do in fact describe the same physical quantity. We conclude that the source of the TH response in plasmonic nanostructures is most likely the bare gold nonlinearity, which is driven and enhanced by the resonant plasmonic polarization $\mathbf{P}_{\text{loc}}(\mathbf{r}, \omega)$.

At last, we ask whether plasmonic Fano resonances allow for enhanced TH generation in comparison to simple plasmonic dipole antennas. In our experiment the maximum TH light polarized parallel to the dipole increases slightly with decreasing coupling between the dipole and the quadrupole. This is as well confirmed by our oscillator model, which predicts the strongest TH response for a very small coupling coefficient κ , which is equivalent to an isolated dipole. We also observed in experiment that dipole antennas can be more efficient in terms of TH generation than the dolmen-type Fano structures (see also Fig. A3 in the appendix).

However, a further increase of the lifetime of the dark mode by a factor of two, which is a crucial parameter for the TH response, is predicted by the model to lead to the doubling of the TH intensity from the dipole mode compared to the TH from isolated dipole antennas. Simultaneously, the TH intensity of the dark mode should be enhanced by over half an order of magnitude. It might be possible to increase this lifetime by using improved structure geometries or by utilizing silver instead of gold for the quadrupole wires, since it exhibits a lower intrinsic damping. Beyond that, it could be promising to resonantly couple other systems, such as excitonic or molecular systems, which intrinsically exhibit quite long lifetimes, to plasmonic dipole antennas and create narrow Fano resonances [141]. This way one could facilitate the required lifetime reduction of the dark mode. This implies that plasmonic Fano resonances instead of simple plasmonic dipole antennas can give extra nonlinearity enhancement, however only for carefully designed structures.

In conclusion, we performed TH spectroscopy of plasmonic dolmen-type nanostructures, that exhibit plasmonic Fano resonances in their linear extinction spectrum. The TH light polarized parallel to the dipole was found to peak close to the low energy peak of the Fano resonance and originates from the dipole rod. The TH polarization of the subradiant mode interferes destructively in the far-field due to the out-of phase oscillation of

the two quadrupolar wires at the fundamental frequency. In fact, similar to this manuscript it was found in fishnet metamaterials that the TH angular radiation pattern can be explained by the constructive and destructive interference of TH sources originating from anti-symmetric charge oscillations [142]. Furthermore, the comparison of experimental TH spectra with an anharmonic oscillator model and FEM simulations shows strong indications for the TH response of plasmonic Fano structures to be the optical nonlinearity of the bare gold driven and enhanced by the resonant plasmonic polarization $\mathbf{P}_{\text{loc}}(\mathbf{r}, \omega)$.

4.3.2 *The Complex Coupling Coefficient in Coupled Plasmonic Systems*

In order to describe the linear and the TH response of the dolmen-type plasmonic Fano structures in the previous section within the framework of the coupled oscillator model, we needed to implement a complex coupling coefficient

$$\kappa = |\kappa| \cdot e^{i\Phi}, \quad (4.43)$$

to account for the retarded interaction between the plasmonic modes. Since we did not discuss the origin of this complex coupling coefficient in detail, here we further elaborate on this.

We fabricated another series of gold dolmen-type nanostructure arrays, with the same geometrical parameters as given in Fig. 4.10(c), however, for this new sample we varied the gap distance g over a broader range, namely from about 20 to 100 nm in steps of 10 nm. Furthermore, for comparison we as well fabricated a dipole antenna array, which lacks the quadrupole rods, but exhibits the same lattice constant as the dolmen-type nanostructures.

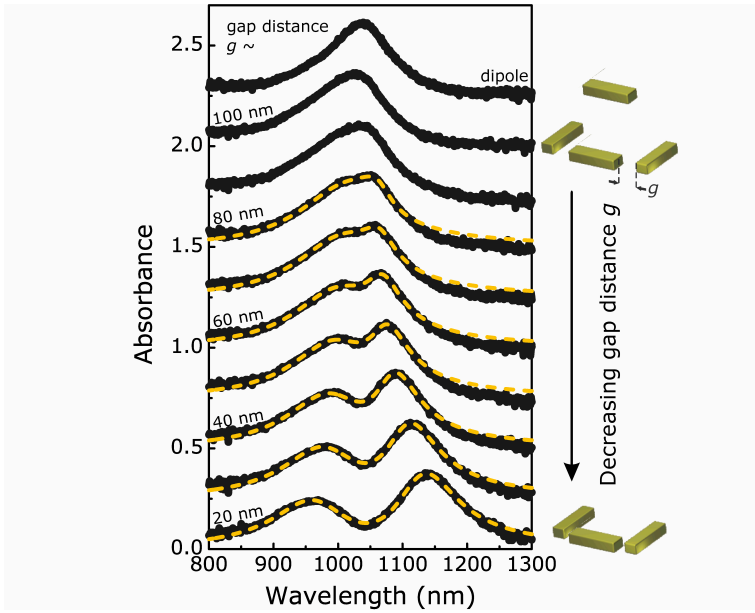


Figure 4.16: Measured absorbance spectra (black line) of plasmonic dolmen-type nanostructure arrays for different values of the gap distance g , decreasing from top to bottom from about 100 to about 20 nm. For comparison the topmost spectrum corresponds to the absorbance of a dipole antenna array. Furthermore, the yellow dashed lines correspond to fits of the absorbance spectra with equation (4.41) derived from the coupled oscillator model with a complex coupling coefficient $\kappa = |\kappa| \cdot \exp^{i\phi}$.

For excitation along the dipole of the dolmen-type structures we measured the transmittance spectra T , the reflectance spectra R and calculated via $T + R + A = 1$ the corresponding absorbance spectra A . The resulting absorbance spectra are depicted in Fig. 4.16 for decreasing gap distance g from top to bottom. For increasing coupling, i.e. decreasing gap distance, we observe as expected a more pronounced splitting of the Fano resonance peaks.

In order to determine the linear optical properties of the nanostructure arrays we fitted the linear optical absorbance spectra with equation (4.41) for the seven smallest gap distances of our

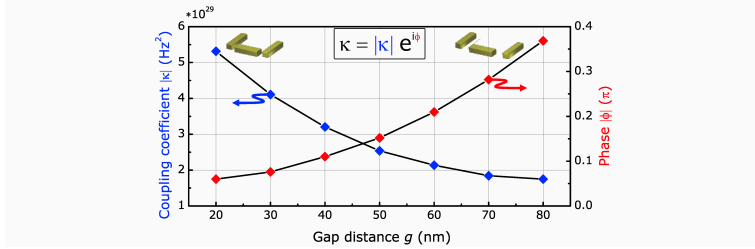


Figure 4.17: Absolute value $|\kappa|$ and phase ϕ of the complex coupling coefficient κ for different values of the gap distance g in plasmonic dolmen-type nanostructures, which have been determined by fitting of the measured absorbance spectra with equation (4.41).

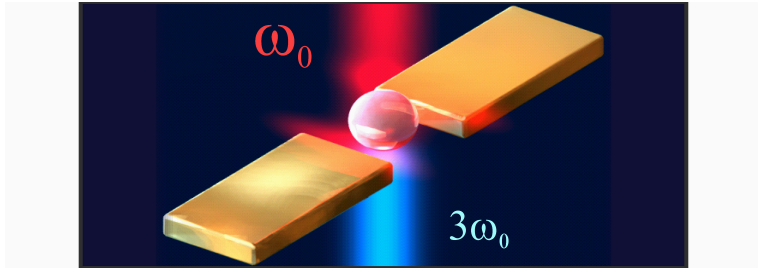
sample. For larger gap distances than about 80 nm the fitting of the absorbance spectra becomes highly ambiguous due to the weak coupling between the plasmonic modes. The six free parameters in the fitting are the two resonance frequencies ω_d and ω_q , the damping constants γ_d and γ_q , the coupling coefficient κ and an overall amplitude. We find that the absorbance spectra can not adequately be fitted by using an entirely real coupling coefficient κ , in particular in the case of the larger gap distances. However, by implementing a complex coupling coefficient $\kappa = |\kappa| \cdot e^{i\phi}$ [138] and therefore one more fitting parameter, which is the phase ϕ of this complex coupling coefficient, the absorbance spectra can be fitted very well. In Fig. 4.16 the fits of the absorbance spectra (yellow dashed) are shown together with the measured absorbance spectra.

In Fig. 4.17 we display the absolute value $|\kappa|$ as well as the phase $|\phi|$ of the complex coupling coefficient κ in dependence of the gap distance g , which we extracted from our fitting. As expected we find a monotonic decrease of the absolute value $|\kappa|$ of the coupling coefficient for increasing gap distance g . This circumstance is simply caused by a reduced near-field coupling for larger distances of the plasmonic nanorods. In addition to the absolute value we also show the absolute value of the phase $|\phi|$

of the complex coupling coefficient, which is found to increase monotonically with increasing gap distance g .

As mentioned at the beginning the reason for the increasing phase of the coupling coefficient for increasing gap distance is the retarded interaction between the gold nanorods. The effect of a force can spread maximally with the speed of light, which leads to a non-instantaneous coupling of the two plasmonic modes.

To summarize, the interaction between plasmonic nanoparticles which are separated by several tens of nanometers is non-instantaneous due to the retardation of light. This circumstance can be described in the oscillator model by the implementation of a complex coupling coefficient $\kappa = |\kappa| \cdot e^{i\phi}$.



4.4 DOUBLING THE EFFICIENCY OF THIRD HARMONIC GENERATION BY POSITIONING ITO NANOCRYSTALS INTO THE HOT-SPOT OF PLASMONIC GAP-ANTENNAS

The optical properties of nanoscale matter differ strongly from those of their bulk counterparts. The reasons can be manifold: While the mere reduction in size leads to a massively reduced light-matter interaction volume, resonant and confinement effects, such as Mie resonances [32] or surface plasmon polariton modes can significantly alter the optical properties. Let us consider as an example the nonlinear optical response of bulk crystals: When illuminated with an intense light field they can exhibit extremely high conversion efficiencies for second harmonic (SH) and third harmonic (TH) generation, respectively [16]. For a number of applications, such as optical bio-labels [143–146], as well as from a fundamental physics standpoint, it is very intriguing to study these effects in nanocrystals [147]. However, any attempt to study their nonlinear optical response will be largely hampered by the extremely small sample volume, that is, the small conversion volume and potentially by the limited electric field strength of the external light field [148].

Both challenges appear to be uniquely addressed by plasmonics [6, 149–151], another field of nanoscale light matter interaction. Plasmonic nanoantennas exhibit extremely large resonant light interaction cross sections, much larger than their geometrical size [149]. Moreover, due to their sub-wavelength dimen-

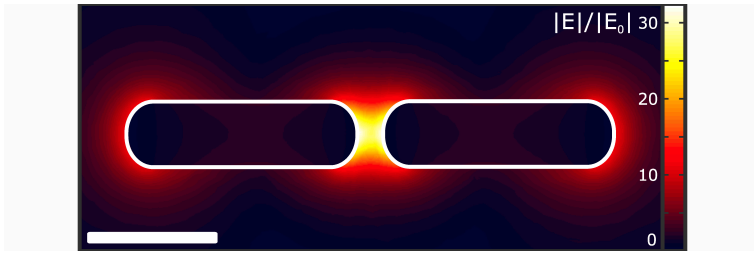


Figure 4.18: Simulation of the electric near-field enhancement $|E|/|E_0|$ inside and in the near surrounding of a plasmonic gap-antenna. The field distribution is shown for the plane symmetrically cutting the antenna and for resonant excitation. The scale bar corresponds to 100 nm.

sion they confine far-field radiation into sub-wavelength volumes, leading to significantly enhanced electric near-fields. It has been shown that purely plasmonic systems exhibit significant conversion efficiencies for SH generation [105, 152, 153] and TH generation [131, 154], as well as other nonlinear optical processes [155, 156], in particular when taking the small structure volume into account [106, 157, 158]. Consequently, researchers have envisioned the combination of well-known and highly efficient bulk nonlinear dielectrics with plasmonic nanoantennas for further enhancement and even more efficient nonlinear light sources at the nanoscale [114, 159–165].

In this Letter we realize and investigate exactly such a system. First, we demonstrate the fabrication of hybrid indium tin oxide (ITO) nanocrystal-incorporated plasmonic gap-antennas using a two step electron beam lithography process. The ITO nanocrystals possess a high nonlinear optical susceptibility $\chi^{(3)}$ [114, 166]. Second, we investigate the hybrid nanostructure arrays by means of third harmonic spectroscopy and observe in experiment and in simulation doubling of the third harmonic response of the hybrid system, when comparing to the TH response of an identical bare plasmonic gap-antenna array, without ITO nanocrystals. Third, we identify the origin of the third harmonic signal enhancement,

which is mainly related to changes in the linear optical properties and the lifetime of the plasmonic antenna resonances.

In our experiments and simulations we utilize arrays of dimer nanoantennas consisting of two identical gold rods separated by a small gap, cf. Fig. 4.18. Illuminating the nanostructure arrays with electromagnetic plane waves polarized along the long-axis of the gap-antennas excites the hybridized symmetric plasmonic mode, located in the near-infrared spectral region at about 1000 nm. To estimate the electric field enhancement $|\mathbf{E}|/|\mathbf{E}_0|$ associated with this plasmonic mode, we perform finite element simulations of the structures, where \mathbf{E} and \mathbf{E}_0 are defined as the local electric field amplitude and the incoming electric far-field amplitude, respectively. For the simulations we utilize a commercial software package (Comsol Multiphysics). Therein, the structures are defined on a substrate with a constant refractive index of $n = 1.5$ and for the optical properties of gold we use the data of Johnson and Christy [139]. Fig. 4.18 shows the electric field enhancement $|\mathbf{E}|/|\mathbf{E}_0|$ for resonant plane wave excitation of our plasmonic gap-antenna. As expected, the strongest electric field enhancement of about 20 to 30 is observed in the gap region of the dimer nanoantenna, which is commonly referred to as the antenna "hot-spot". This hot-spot is generally expected to be the major source of any nonlinear signal and is in particular the ideal position for a selective incorporation of a nonlinear dielectric [125, 167].

In order to experimentally study the proposed system we developed a process for the selective filling of the antenna gaps with different kind of nanoparticles. The fabrication of the hybrid nanostructure arrays works via a two-step electron beam exposure [44] and a subsequent so-called squeegee process [168, 169]. In a first step the nanoantennas as well as alignment marks are defined in a double layer Poly(methyl methacrylate) (PMMA) resist on a fused silica substrate (Suprasil, Heraeus), followed by the evaporation of a 2 nm Cr adhesion layer and a 40 nm gold layer and the subsequent lift-off of the resist. Afterward, the sam-

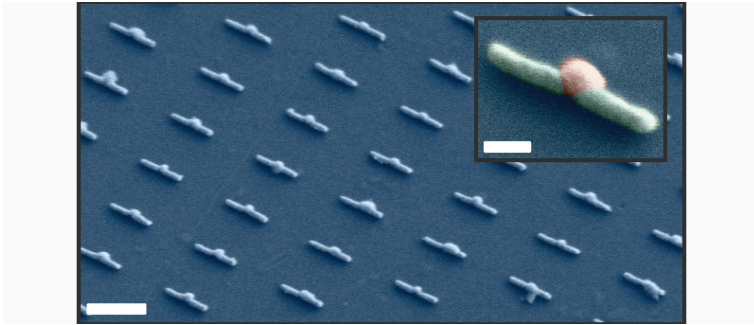


Figure 4.19: Colored scanning electron micrograph (SEM) of a hybrid ITO nanocrystal-incorporated plasmonic gap-antenna array. The inset shows an SEM of a single antenna element. The individual gap-antenna elements consist of two identical gold rods, with a height, a width and a length of about 40, 50 and 180 nm, respectively. The gap distance is about 20 nm. The scale bar is 500 nm in the overview and 100 nm in the inset, respectively.

ple is once again coated with a double layer of PMMA resist, and the alignment marks are used to selectively open resist apertures on top of the nanoantenna gaps. Subsequently, nanoparticles can be transferred into the apertures from a nanoparticle solution. In our case monodisperse ITO nanocrystals have been synthesized according to literature methods [170], resulting in a mean crystal diameter of 6 nm, suspended in hexane. A droplet of the concentrated nanocrystal-hexane solution is deposited onto the resist and swept across the sample surface by a cut piece of polydimethylsiloxane (PDMS). The particles are dragged along with the meniscus of the slowly evaporating hexane solution and deposited into the resist openings [169]. Once the hexane is nearly fully evaporated, the remaining nanocrystals are dragged to the rim of the substrate and away from the gold nanostructures in order to prevent clustering in the structured areas. Subsequently, the sample is placed top-down on additional glass slides in an acetone beaker to remove the PMMA resist mask and the excess nanocrystals. The final nanoantenna arrays have a size of $90 \times 90 \mu\text{m}^2$, with an excellent filling ratio of the antenna feed gaps, see scanning electron micrographs in Fig. 4.19. The following

measurements of the plasmonic nanoantenna arrays are intrinsically ensemble measurements and might therefore be influenced by inhomogeneous effects, in particular by size and shape variations within an antenna array. However, we find good agreement between measured and simulated far-field spectra, which underlines the excellent homogeneity of the fabricated nanostructure arrays.

First of all the incorporation of the high refractive index ITO nanocrystals into the hot-spot of the gold gap-antennas influences the plasmonic mode of the nanoantennas, since these are highly sensitive to changes in the dielectric environment. In particular, the resonance frequency ω_0 of the plasmonic mode shifts to lower frequencies due to the increase in the outer effective dielectric constant. Therefore, it is necessary to perform spectrally resolved nonlinear spectroscopy to ensure the resonant excitation of the antenna arrays and to determine the spectral position of highest conversion efficiency [108]. Hence, we focus sub-30 fs laser pulses polarized along the long antenna axis and tunable between 900 and 1200 nm with a 75 mm focal length achromatic lens on the nanostructure arrays. Subsequently, the generated TH signals radiated in forward direction, which are as well polarized along the antenna axis, are recollimated, focused into a grating spectrometer, and measured with an attached Peltier-cooled CCD camera. Finally, the measured TH spectra are spectrally integrated, yielding a scalar value describing the TH intensity. All TH measurements are normalized to a TH signal which is generated at the interface of the bare substrate. Thereby, we eliminate the influence of any wavelength dependent components, changing beam parameters, or the detector efficiency [171].

Fig. 4.20(a) depicts the spectroscopic results for one exemplary bare (green) and hybrid (orange) antenna array. The solid lines correspond to the measured linear extinction spectra of the antenna arrays, whereas the data points (diamonds) represent the normalized TH intensities. The linear extinction spectrum of the bare gap-antenna array (green) is characterized by a single

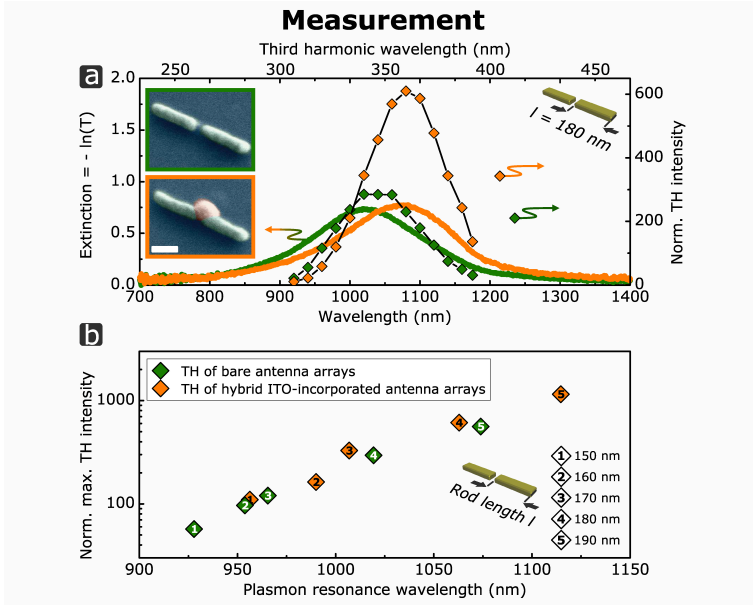


Figure 4.20: (a) Third harmonic spectroscopy of bare (green) and hybrid ITO nanocrystal-incorporated (orange) plasmonic gap-antenna arrays, with an antenna rod length l of about 180 nm. The solid lines correspond to the measured extinction spectra, while the datapoints are the measured TH intensities plotted over the fundamental excitation wavelength. The top axis shows the corresponding TH wavelength. (b) Maximum of the measured TH intensities of different bare (green) and ITO nanocrystal-incorporated (orange) gap-antenna arrays with different rod length l plotted over their corresponding plasmon resonance wavelength. Data points with identical labeling correspond to an equal antenna length l , which is given in the right corner of the graph.

Lorentzian peak associated with its plasmon resonance at around 1025 nm. As reported in earlier work [109, 113, 172], we find the peak of the TH conversion efficiency (green diamonds) close yet slightly red-shifted with respect to the peak of its far-field extinction spectrum. As mentioned above the incorporation of the ITO nanocrystals leads to a significant red-shift of the extinction peak by about 45 nm. The origin of the red-shift is the increase of the dielectric constant ϵ_m of the environment, which changes in the gap region, that is, the ITO volume from $\epsilon_{m,AIR} = 1$ of air to about $\epsilon_{m,ITO} \sim 2.9$ of the ITO [173]. Consequently, the peak of the TH conversion efficiency (orange diamonds) shifts together with the linear spectrum to longer wavelengths by about the same value. The maximum TH conversion efficiency is about a factor of two larger when compared to that of the bare gap-antenna arrays.

In order to further investigate the role of the ITO nanocrystals in the measured enhancement of the TH conversion efficiency, we tune the spectral characteristics of the gap-antennas by varying the length l of the two gold rods from about 150 to about 190 nm, in a step size of 10 nm. As before, we measured the TH spectra of the bare as well as the hybrid ITO nanocrystal-incorporated antenna arrays. The measured linear and TH signal spectra exhibit very similar behavior as the exemplary one shown in Fig. 4.20(a). For clarity, in Fig. 4.20(b) we only plot the maximum TH signal strength for each antenna array versus the spectral position of its plasmonic resonance (green: bare, orange: nanocrystal-incorporated). We observe a monotonic increase of the TH intensity radiated from all measured antenna arrays when plotted over their corresponding plasmon resonance wavelength. In particular, we find that the TH signal increases by about an order of magnitude in the considered wavelength range. Remarkably, the TH maxima of the hybrid nanocrystal-incorporated gap-antenna arrays and the bare antenna arrays follow the same trend, not only qualitatively but also quantitatively. The measured data suggests that only the spectral position of the plasmonic resonance

determines the maximum TH signal. In contrast, if there was a significant contribution of the ITO nanocrystals to the overall TH signal, the bare and the ITO nanocrystal-incorporated antenna arrays should form two distinct subsets in Fig. 4.20(b), with the latter having a higher overall TH signal. The observation that they form a single indistinguishable set is a strong indication that a contribution of the ITO nanocrystals to the overall TH intensity is not the main reason for the observed increased TH conversion efficiency. However, it is known that the linear optical properties of a plasmonic system have crucial influence on its nonlinear optical response. In particular, the spectral position of the plasmon resonance frequency ω_0 and the damping γ , that is, the quality factor Q or the lifetime τ of the resonator, are of crucial importance [108, 113, 126].

In order to determine the origin of the TH signal enhancement between hybrid ITO nanocrystal-incorporated and bare gap-antenna arrays we perform finite element simulations (Comsol Multiphysics) of the nanostructures, which were already used for the calculation of the absolute electric field enhancement in the gap-antennas in Fig. 4.18. The TH signal radiated from the hybrid plasmonic gap antennas is directly related to the TH polarization $\mathbf{P}_{\text{TH}}^{(3)} = \epsilon_0 \chi^{(3)}(\omega) \mathbf{E}^3$ in the gold and the ITO volume, respectively. However, quantitative and wavelength dependent literature values for the third order susceptibilities $\chi^{(3)}(\omega)$ for gold and ITO are hardly available. Hence, instead we consider the linear polarization $\mathbf{P}(\mathbf{r}, \omega)$ in the gold and the ITO volume, since the third power of the linear polarization is proportional to the TH polarization $\mathbf{P}_{\text{TH}}^{(3)} \propto \mathbf{P}(\mathbf{r}, \omega)^3$, and since this gives a quite good estimate for the different contributions to the TH response [136, 174].

In Fig. 4.21(a) we show the x-component of the cubed linear polarization $\mathbf{P}(\mathbf{r}, \omega)^3$ within a bare and a hybrid ITO nanocrystal-incorporated gold gap-antenna (each at the spectral peak position of their respective plasmonic resonances), since only the x-components (along the antenna axis) of the TH near-field polar-

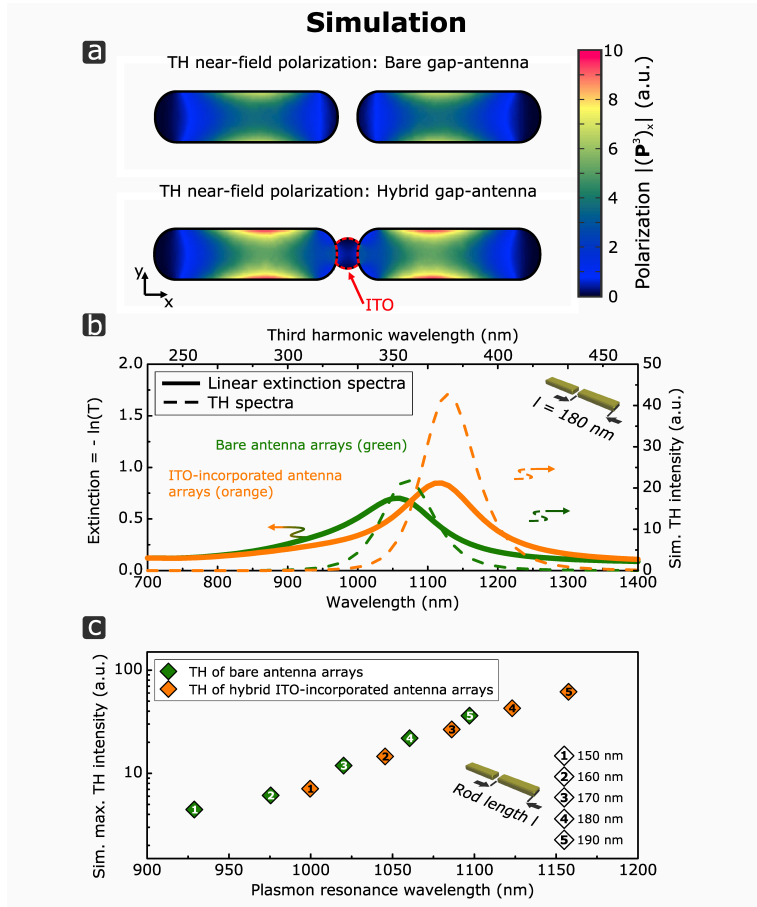


Figure 4.21: (a) Simulations of the x -component of the TH near-field polarization in a bare and a hybrid ITO nanocrystal-incorporated gold gap-antenna. The red-rimmed area indicates the ITO volume. (b) Simulated linear extinction spectra (solid lines) and simulated TH intensities (dashed) for bare (green) and ITO nanocrystal-incorporated (orange) gap-antennas plotted over the fundamental wavelength. The top axis shows the corresponding TH wavelength. (c) Maximum of the simulated TH intensities of different bare (green) and ITO-incorporated (orange) gap-antenna arrays with different gap-antenna length l .

izations contribute to the TH far-field amplitude polarized along the gap-antennas. Two important observations can be made:

1) In case of the bare gap-antenna the strongest TH polarization is observed in the region of highest plasmonic current density, namely close to the surface in the center region of the gold rods. In particular, no TH polarization is observed in the gap region, as there is no material present which could carry any nonlinear polarization. 2) In case of the ITO nanocrystal-incorporated gap-antenna we observe a distinct enhancement of the TH near-field polarization inside the gold volume. However, compared to the TH polarization in the gold we observe only a very weak TH polarization inside of the ITO volume. Of course, the TH near-field polarization in the ITO volume becomes significantly enhanced by the presence of the plasmonic antenna, however, *compared to the TH polarization in the gold volume this is only a minor contribution the overall TH response*. The strong difference of the TH polarizations in both materials is directly linked to their linear optical properties, namely to the weak linear polarizability of a dielectric material like ITO as compared to a metal such as gold.

This observation confirms what we already suspected: The overall TH response seems to be dominated by the TH polarization in the gold rather than by the optical nonlinearity of the ITO. However, since the simulated polarization maps cannot directly be measured we need to transfer this information into experimentally accessible quantities, which are the linear extinction spectra as well as the TH signal strength. Therefore, we calculate the TH signals radiated from the bare and the hybrid gap-antenna arrays by integrating the TH near-field polarizations over the volume V of the gold antennas. In particular, we neglect all TH polarizations in the ITO volume, since they will contribute only a minute TH signal to the overall TH intensity, due to the small TH polarization and also due to the small volume of the ITO as

compared to the gold. Hence, the TH electric field amplitude $E_{\text{TH}}(\omega)$ radiated into the far-field is given by [174]

$$\mathbf{E}_{\text{TH}}(\omega) \sim \omega_{\text{TH}} \int_V \mathbf{P}(\mathbf{r}, \omega)^3 d\mathbf{r}^3, \quad (4.44)$$

$$\text{where } \mathbf{P}(\mathbf{r}, \omega)^3 = (P_x^2 + P_y^2 + P_z^2) \cdot \mathbf{P}(\mathbf{r}, \omega), \quad (4.45)$$

ω_{TH} is the TH frequency, and P_x , P_y and P_z are the complex valued cartesian components of the linear polarization $\mathbf{P}(\mathbf{r}, \omega)$. Fig. 4.21(b) depicts the simulated linear (solid) and TH spectra (dashed) for a bare (green) and a hybrid (orange) gap-antenna array with a rod length l of 180 nm calculated via equation (4.44). For the TH spectra, similar to Fig. 4.21(a) we only evaluated the x-component of the TH electric field amplitude in equation (4.44), since this component corresponds to the measured TH polarization along the gap-antennas. Despite the fact that we have completely neglected the TH response of ITO (only taking into account its purely linear dielectric contribution) we find excellent agreement between the simulation results shown in Fig. 4.21(b) and the corresponding experimental spectra in Fig. 4.20(a). In particular, the linear resonance positions are reproduced, as is the red-shift between the maximum TH signal and the linear plasmon peak. Even more importantly, the enhancement by a factor of about two of the maximum TH signal by incorporation of the ITO nanocrystals is as well observed.

The simulations are also capable to capture the trend shown in Fig. 4.20(b): We simulated the linear spectra and the TH spectra for different rod lengths l , ranging from 150 to 190 nm and plotted in Fig. 4.21(c) the maximum TH intensity of each antenna array depending on their corresponding plasmon resonance wavelength. As in the experiment we observe a monotonic increase of the maximum TH intensity by about an order of magnitude over the whole considered wavelength range. In summary, the fact that all characteristic features of the experimental results are well reproduced while disregarding any optical nonlinearity of

the ITO nanocrystals is clear proof of a at best minute contribution of the ITO nanocrystals to the overall TH response.

One might ask why we observe an increase in the TH signal strength at all. More importantly, can one intuitively understand the physical processes involved? The origin of the TH enhancement has to be correlated to an increased near-field enhancement or equivalently to an increased dipole moment \mathbf{p} of the plasmonic oscillations in the gold gap-antennas. When the ITO nanocrystals are incorporated in the antenna gaps or the rods of the gap-antennas are elongated, the dielectric constant ϵ_m of the environment or the volume V of the gap-antennas is increased, respectively. Both partly enhance the dipole moment \mathbf{p} of the plasmonic resonance [6]. In a full electrodynamic solution several parameters, which influence the overall dipole moment \mathbf{p} in plasmonic antennas, vary simultaneously and cannot be completely disentangled.

However, we want to stress two important quantities of the plasmon resonance for the TH response, which are the plasmon resonance frequency ω_0 and the damping constant γ . It can be shown in terms of a harmonic oscillator model, which has proven to describe the nonlinear response of bare plasmonic nanoantennas quite well [108, 113], that the absolute value of the dipole moment $|\mathbf{p}|$ of the plasmon resonance at its peak position is in good approximation ($\gamma \ll \omega_0$) inversely proportional to these quantities: $|\mathbf{p}| \propto 1/(\omega_0\gamma)$. Since the TH intensity scales with the sixth power of the plasmonic dipole moment \mathbf{p} , the TH signal should critically depend on these quantities and increase with decreasing ω_0 and γ [113, 136].

If this reasoning is correct, we expect a monotonic decrease of the linewidth $\Delta\omega_{\text{FWHM}}$, which is proportional to the damping constant γ , for red-shifted antenna arrays, irrespective of whether the shift is induced due to the presence of the nanocrystals or due to an elongation of the gap-antenna length l . Hence, we extracted the linewidth $\Delta\omega_{\text{FWHM}}$ of the plasmonic resonances by fitting

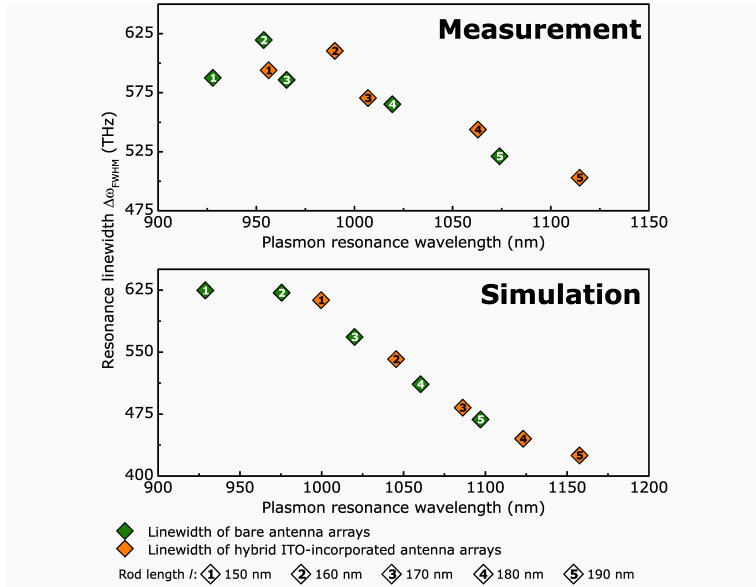


Figure 4.22: Linewidth $\Delta\omega_{FWHM}$ of plasmon resonances of measured (top) and simulated (bottom) linear spectra plotted over the plasmon resonance wavelength for bare (green) and ITO nanocrystal-incorporated (orange) gap-antenna arrays with different gap-antenna length l .

the measured and the simulated linear extinction spectra with a Lorentzian function and display them in dependence of the corresponding plasmon resonance wavelength in Fig. 4.22. In measurement and in simulation we observe a monotonic decrease of the resonance linewidth $\Delta\omega_{FWHM}$ with the plasmon resonance wavelength. Noteworthy, the linewidth $\Delta\omega_{FWHM}$ of the bare (green) and the hybrid (orange) gap-antenna arrays follow quantitatively the same behavior and the two sets are indistinguishable.

Most likely, the origin of the reduced resonance linewidth can be attributed to an increased spectral distance with respect to d-band interband absorption, which occurs for gold in the visible regime. At the same time an increase of radiative losses, which could be expected for the increased volume of the elongated rods

of the gap-antenna, seems to not play a major role for our structures [35].

Thus, for the bare and the hybrid nanostructure arrays the increase in the TH signal strength is mainly related to a decrease of the resonance frequency ω_0 and a decrease in the linewidth $\Delta\omega_{\text{FWHM}}$ or the damping constant γ , which lead to an enhanced dipole moment \mathbf{p} of the red-shifted plasmon resonances and therefore to increased generation of TH light.

To summarize, we developed a new method for selectively filling nanoparticles from solution into the hot-spot of plasmonic gap-antennas and studied the TH response of corresponding hybrid ITO nanocrystal-incorporated plasmonic gap-antenna arrays. We observed an enhancement of the TH signals radiated from the hybrid gap-antenna arrays by about a factor of two when comparing them to the TH signals of identical bare plasmonic gap-antenna arrays. A close study revealed that the enhanced TH signal strength is mainly related to changes in the linear optical properties of the respective antenna arrays. The incorporation of the ITO nanocrystals leads a red-shift of the plasmon resonance and therefore to a decrease of the resonance frequency ω_0 and the linewidth $\Delta\omega_{\text{FWHM}}$. Both decreasing quantities increase the dipole moment \mathbf{p} of the plasmon resonances and lead ultimately to the observed increase in the TH signal strength. Hence, the TH response of our plasmonic gap-antennas can be boosted by either increasing the gap-antenna length or by the deposition of dielectric material around the gold nanostructures, which red-shifts the plasmon resonance and therefore increases the TH signal strength. Furthermore, our TH signal is found to be nearly exclusively generated in the gold volume and not inside the ITO nanocrystals [175], which is directly related to the higher *linear* polarizability and the third-order susceptibility of gold when compared to that of ITO.

Despite the fact that we were not able to resolve an enhanced TH signal from the dielectric material itself, the overall concept

is still promising. We believe that other nonlinear materials with an even higher linear polarizability and also higher third-order susceptibility should give a distinct contribution to the overall TH response when incorporated into the hot-spot of plasmonic nanoantennas, which then also should allow for enhancing the TH response at a certain wavelength. An increase of the plasmon lifetime, e.g., by using more complex structures [117, 174, 176] or by the implementation of single crystalline metals [177] should even further boost the nonlinear optical response. Furthermore, in this work we utilized a third order nonlinear effect which can be observed in isotropic materials as it is not subject to symmetry restrictions, such as even order processes [53]. It has indeed been demonstrated that the use of SH generation in mixed systems composed of split ring resonators and crystalline gallium arsenide substrates allows for the disentanglement of contributions stemming from the gold structures itself as well as from the crystalline substrate [162, 178]. Similarly, one could incorporate non-inversion symmetric materials, such as lithium niobate, in the hot-spot of the nanoantennas and study the radiated SH rather than TH signal. The combined system presents a number of challenging aspects, for example the need for controlling the spatial orientation of the crystallographic axis of the nanocrystals relative to the nanoantennas, but also offers an intriguing and extensive parameter space for complex and highly nonlinear hybrid systems as nanoscale coherent light sources, for example to excite nanoantenna arrays coherently [179].

4.5 ULTRABROADBAND CHIRPED PULSE SECOND HARMONIC SPECTROSCOPY

One of the key technologies in optics and photonics is white light spectroscopy. It allows for measuring the linear optical response of a sample over a broad spectral range. Beyond optical information, the linear optical spectra allow for drawing conclusions on the structural composition of the sample under investigation, for example when using circular dichroism spectroscopy [180]. In addition, nonlinear optical spectroscopy, which originates from intense light-matter interaction, has proven to deliver additional information. Second harmonic (SH) generation spectroscopy for example enables studying the crystal structure of a non-inversion symmetric medium [181–183]. Furthermore, SH imaging microscopy can in some cases give superb contrast when compared to ordinary optical microscopy [143, 184, 185].

In contrast to linear optical spectroscopy with a broadband light source, SH spectroscopy often uses a narrow-band laser, and hence, the second order response is measured only over a narrow frequency range. However, just like the linear optical response, which is governed by the first order susceptibility $\chi^{(1)}(\omega)$, also the second-order susceptibility $\chi^{(2)}(\omega)$ in general is a frequency-dependent quantity, in particular, if the material exhibits linear optical resonances in the spectral range of interest [16]. Hence, it is desirable to have access to spectrally resolved values of the second-order susceptibility. In principle, ultrabroadband laser sources, which exhibit ultrashort pulse durations in the visible and the near-infrared, are available and deliver the bandwidth and the light intensities which should allow for measuring the second-order response over a broad spectral range [19–21, 186]. However, the retrieval of the frequency-dependent second-order susceptibility $\chi^{(2)}(\omega)$ is rendered highly ambiguous when an ultrabroadband laser source is focused on the sample due to frequency mixing, as explained in the following:

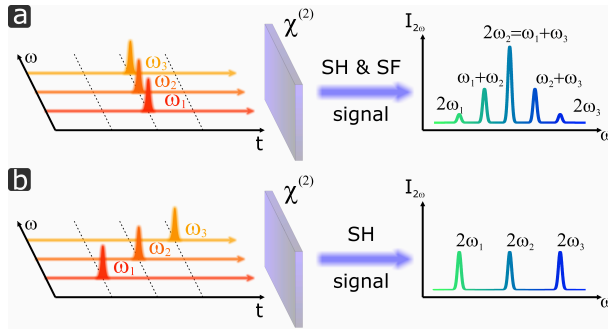


Figure 4.23: Schematic illustration for second harmonic (SH) and sum frequency (SF) generation for three different incoming frequencies travelling (a) at zero time delay or (b) consecutively in time.

Imagine for simplicity a laser source consisting of three different equally spaced frequency components overlapping in time as shown in Fig. 4.23(a). When focused onto a second-order nonlinear material, SH and sum frequency (SF) generation can be observed, which results in a nonlinear spectrum that exhibits five distinct intensity peaks. In particular, the central peak in the nonlinear spectrum is composed of the SH signal of the fundamental frequency ω_2 as well as of the SF signal of the fundamental frequencies ω_1 and ω_3 . For an unknown frequency-dependent second-order susceptibility it is impossible to determine the intensity ratio of both contributing effects to this central peak, which also renders the retrieval of the second-order susceptibility at the frequency ω_2 impossible.

Instead of using ultrabroadband laser sources researchers therefore have implemented widely tunable narrow-band lasers in order to avoid the SF mixing processes and to unambiguously measure the nonlinear response over a broad spectral range [126, 187–189]. However, tunable systems often require a highly complex setup and suffer from power variations and instabilities, which makes these experiments quite sophisticated and time-consuming.

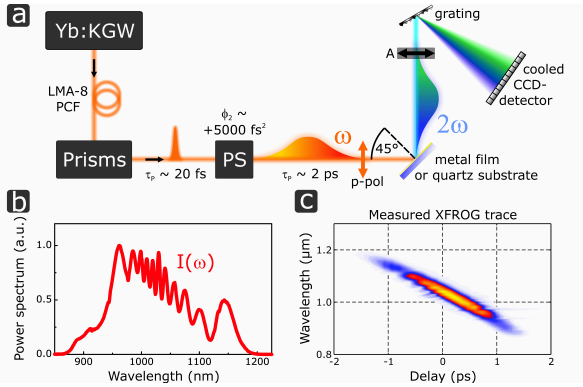


Figure 4.24: (a) Experimental setup for ultrabroadband chirped pulse SH spectroscopy (LMA: large mode area, PCF: photonic crystal fiber, PS: pulse shaper, A: analyzer). (b) Measured laser spectrum at the output of the pulse shaper. (c) Measured XFROG trace of the ultrabroadband strongly chirped laser pulses.

In this Letter we introduce a new method for measuring an entire nonlinear SH spectrum using a single *chirped* broadband laser source [190]. By introducing a large amount of dispersion we suppress SF mixing processes, since the different frequency components lack temporal overlap. Therefore, neighbouring frequencies perform SH generation only individually, which is schematically depicted in Fig. 4.23(b). We demonstrate this method by measuring the optical SH response of various metal films in the wavelength range of about 900 to 1150 nm.

In order to demonstrate this SH measurement technique, which we term ultrabroadband chirped pulse (UCP) SH spectroscopy, we utilize a setup capable to produce ultrabroadband strongly chirped laser pulses as well as more narrow-band tunable ultrashort laser pulses. Thereby, we are able to directly compare UCP and classical SH spectroscopy, where a narrow-band laser is shifted step-wise in wavelength in order to measure a SH spectrum. The experimental setup is schematically depicted in Fig. 4.24(a). We use a homebuilt high-power Yb:KGW solitary mode-locked oscillator at a repetition rate of about 44 MHz emitting

175 fs laser pulses with an average power of about 2.4 W and a central wavelength of 1027 nm [81]. These pulses are coupled into a large mode area (LMA) photonic crystal fiber (PCF) for spectral broadening mainly by self phase modulation. Subsequently, the laser pulses are sent into a prism sequence, which allows to compress the laser pulses down to a pulse duration of about 20 fs [191]. Furthermore, for amplitude and phase modulation we propagate the laser pulses through a 4f pulse shaper (PS), which includes a dual-mask liquid crystal spatial light modulator [94]. Fig. 4.24(b) shows a measured laser spectrum $I(\omega)$ at the output of the pulse shaper. For classical SH spectroscopy amplitude shaping using the spatial light modulator is utilized to generate narrow-band Fourier-limited Gaussian-like 30 fs laser pulses tunable from 900 to 1150 nm [107]. In case of UCP-SH spectroscopy we use the 4f setup in order to generate a group delay dispersion (GDD) ϕ_2 of up to 5365 fs². The GDD ϕ_2 is defined by the second derivative of the spectral phase $\phi(\omega)$ [192]:

$$\phi_2 = \frac{\partial^2 \phi(\omega)}{\partial \omega^2} \quad (4.46)$$

Fig. 4.24(c) shows a measured XFROG trace of the ultrabroadband strongly chirped laser pulses, which we obtained via a SH cross-correlation with the Yb:KGW oscillator pulses [85]. Due to the large dispersion value ($\phi_2 = 5365 \text{ fs}^2$) the laser pulses exhibit a pulse duration on the order of 2 ps. In particular, the different frequency components travel consecutively in time, which leads to the aforementioned suppression of SF mixing.

Finally, the output of the pulse shaper is focused by a 75 mm focal length achromatic lens on a sample surface with an angle of incidence of 45° in p-polarization. The generated SH in reflection is recollimated by a fused silica lens, analyzed by a polarizer also oriented along p-polarization, and the SH signals are measured with a Peltier-cooled CCD camera attached to a spectrometer.

In order to show that SF mixing processes indeed become suppressed by introducing a large amount of dispersion we perform SH generation on a quartz crystal substrate in reflection with different values of GDD ϕ_2 and with the broadband laser spectrum shown in Fig. 4.24(b). The quartz crystal does not exhibit optical resonances in the spectral range of the fundamental laser light as well as the SH light. Hence we can assume a spectrally flat second-order susceptibility $\chi^{(2)}(\omega)$ [16]. For a flat second-order response the generated SH and SF signals are simply proportional to the complex electric field $E(t)$ of the laser pulses in the time domain squared [92]. In order to mathematically determine the SH spectrum $I^{(2)}(\omega)$ we have to perform a Fourier transform of the second-order electric field amplitude $E^{(2)}(t) \propto E(t)^2$. Hence, in the frequency domain the SH spectrum $I^{(2)}(\omega)$ is given by a convolution:

$$I^{(2)}(\omega) \propto \left| \int_{-\infty}^{\infty} d\omega' E(\omega') E(\omega - \omega') \right|^2 \quad (4.47)$$

Here, $E(\omega) = |E(\omega)| \cdot e^{i\phi(\omega)}$ is the complex electric field of the laser pulses in the frequency domain. Measured and simulated SH spectra are depicted in Fig. 4.25 for increasing values of GDD ϕ_2 from bottom to top. For Fourier-limited laser pulses ($\phi_2 = 0 \text{ fs}^2$) the SH spectrum constitutes a single broadband Gaussian-like intensity peak. Although our fundamental laser spectrum is strongly modulated, the SH spectrum exhibits a spectral Gaussian shape due to the SF mixing between all the frequency components. For increasing GDD in measurement and in simulation the SF generation becomes strongly suppressed. This means that as ϕ_2 increases the SH spectrum converges to the fundamental laser spectrum $I(\omega)$ squared. Then equation (4.47) simplifies to:

$$\phi_2 \rightarrow \infty \quad \Rightarrow \quad I^{(2)}(2\omega) \propto I(\omega)^2 \propto |E(\omega)|^4 \quad (4.48)$$

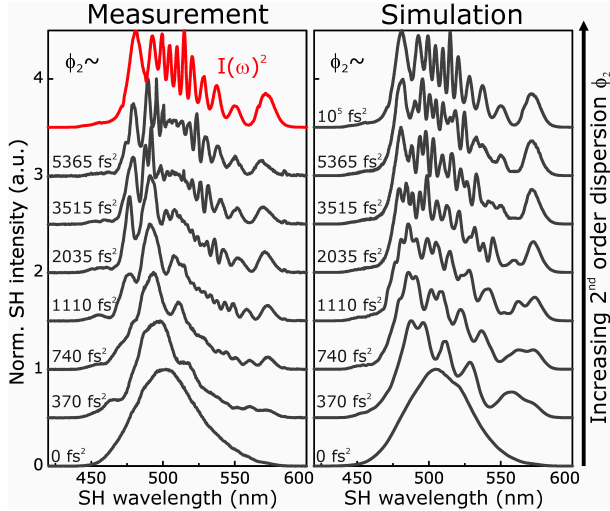


Figure 4.25: Measured (left) and simulated (right) SH spectra generated on a quartz surface with the laser spectrum shown in Fig. 4.24(b) for different values of ϕ_2 , increasing from bottom to top. The increase of dispersion suppresses SF mixing and as a result the SH spectra converge to the laser spectrum squared. The topmost red spectrum in the measurement column does not represent a SH spectrum, but corresponds to the measured laser spectrum from Fig. 4.24(b) squared, plotted over the SH wavelength for comparison.

The maximum value of GDD ϕ_2 which we are currently able to generate with the 4f setup is about 5365 fs^2 . Unfortunately, for this dispersion value SF mixing is not entirely suppressed yet, but it is strongly reduced. This circumstance slightly limits the spectral resolution of UCP-SH spectroscopy, which can be estimated from the phase difference $\Delta\phi = \frac{1}{2}\phi_2\Delta\omega^2$ between frequency components separated by $\Delta\omega$. If the phase difference $\Delta\phi$ between two frequencies approaches π these components interfere destructively and as a consequence SF generation will be suppressed. Using this condition the spectral resolution can be approximated by $\Delta\lambda = \lambda_0^2/\sqrt{2\pi c^2\phi_2}$, where λ_0 is the central wavelength and c is the speed of light. For $\lambda_0 = 1000 \text{ nm}$ and $\phi_2 = 5365 \text{ fs}^2$ we obtain a value of about $\Delta\lambda \sim 18 \text{ nm}$, which is sufficient for UCP-SH spectroscopy of metal films. When increasing the dispersion to even higher values the SH spectrum indeed converges to the laser spectrum $I(\omega)$ squared, which is shown in Fig. 4.25 in red for comparison.

4.5.1 *Measuring the Frequency-Dependent Second-Order Response of Different Metal Films*

In order to demonstrate UCP-SH spectroscopy and to measure the second-order response of metals over a broad spectral range we evaporated 100 nm thick films of gold, copper, silver and aluminum on various quartz substrates by electron beam evaporation. During the evaporation process a small area of the quartz surface was covered so that a part of the substrates remain blank. Subsequently, we measured the SH spectra of the metal films using the maximum available GDD of 5365 fs^2 . Furthermore, the SH spectra from the metal films are divided by a SH spectrum generated at the interface of the blank quartz surface measured with the same maximum dispersion value. Thereby, we account for the spectral shape of the laser source and the influence of any

wavelength-dependent components, very similar to linear optical white light spectroscopy.

The experimental results of these measurements are depicted in Fig. 4.26. The blue datapoints correspond to the SH spectra measured via UCP-SH spectroscopy. These SH spectra exhibit quite high variance at the spectral positions where the reference SH signal from the quartz substrate is close to zero, see Fig. 4.25. Hence, for UCP-SH spectroscopy it is desirable to have an ultrabroadband laser spectrum available which is as smooth and flat as possible. As mentioned above, we as well performed classical SH spectroscopy shown in Fig. 4.26 by the red diamonds for comparison. Therefore, we utilized narrow-band Gaussian-shaped 30 fs laser pulses and tuned these over the entire spectral range in steps of 20 nm. For all SH spectra of the metal films we observe an excellent agreement between UCP and classical SH spectroscopy. In particular, in the SH response of the gold film we find a pronounced peak in the SH generation efficiency close to a SH wavelength of about 500 nm. This peak in the SH spectrum of gold is most likely related to the onset of interband transitions, which occur for gold at around this spectral range [193], see Fig. A4 for ellipsometric data of the metal films. For copper we observe a minimum in the SH spectrum at a SH wavelength of about 530 nm, but an increase towards longer wavelength. The excitation of interband transitions in copper sets in already slightly below 600 nm [139, 194]. Therefore, the SH spectrum of copper indicates a peak at the long-wavelength side of the SH spectrum, however, our spectral range is too limited to entirely resolve this peak position. For silver and aluminum in our spectral window neither at the fundamental wavelength nor at the SH wavelength a resonance occurs. Hence, their SH response should be dominated by a free electron nonlinearity, which is underlined by the fact that we observe very similar SH spectra for aluminum and silver in amplitude and the spectral behavior. Furthermore, the SH spectra show a monotonic increase of the SH generation efficiency towards higher frequencies. These findings

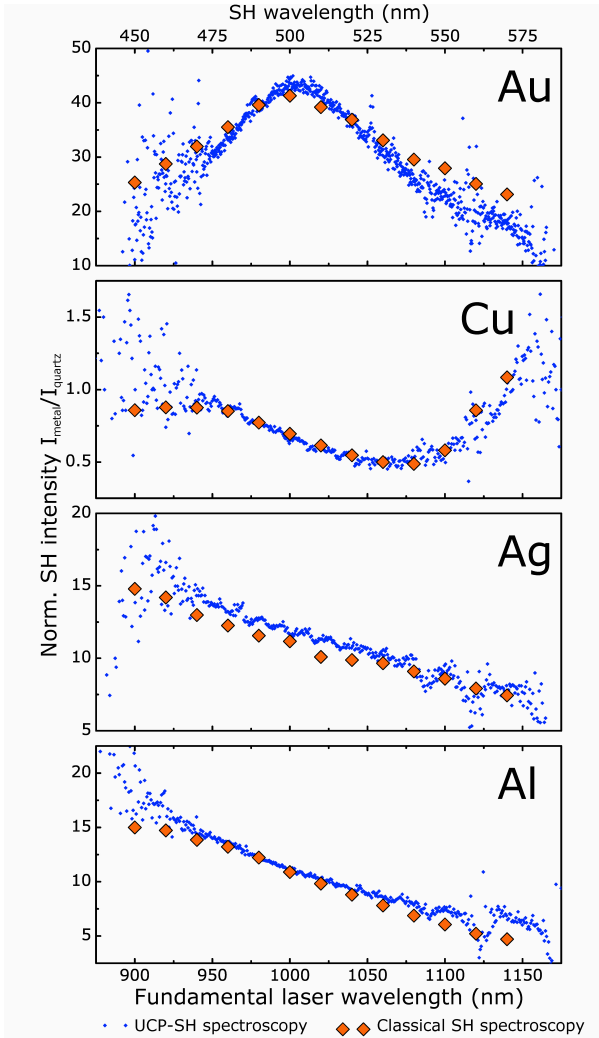


Figure 4.26: SH spectroscopy of 100 nm thick bare metal films plotted over the fundamental laser wavelength. The top axis shows the SH wavelength. The small blue datapoints are measured using UCP-SH spectroscopy. The red datapoints were obtained using classical SH spectroscopy.

are consistent with previous studies of the SH response of metal films [187, 188, 195].

In conclusion, we introduced a spectroscopic SH measurement technique, called ultrabroadband chirped pulse (UCP) second harmonic (SH) spectroscopy, for measuring the frequency-dependent second harmonic response over a broad spectral range. We demonstrated this method by measuring the SH response of metal films in the near-infrared from 900 to 1150 nm. We find the SH spectra of UCP and classical SH spectroscopy to be in excellent agreement. Interband transitions in the metals seem to influence the nonlinear optical SH spectra of the metal films. We believe that in the future UCP-SH spectroscopy might be implemented by propagating broadband ultrashort laser pulses through highly dispersive glasses, which could provide the required dispersion in a straightforward and simple fashion. Furthermore, UCP-SH spectroscopy might be utilized for measuring the spectrally-resolved nonlinear response of semiconductors or plasmonic metamaterials, or for measuring the phase matching bandwidth of nonlinear optical crystals for frequency conversion.

We gratefully acknowledge financial support from the Baden-Württemberg Stiftung (Kompetenznetz Funktionelle Nanostrukturen), from the DFG (SPP1391, ultrafast nanooptics), from the BMBF (13N10146), and the ERC (Complexplas). We thank M. Ubl for the evaporation of the metal films and S. De Zuani for the measurement of ellipsometric data of the metal films.

CONCLUSION AND OUTLOOK

In this thesis the ultrafast nonlinear optical response of complex plasmonic nanostructures has been studied and investigated, experimentally as well as theoretically.

In order to perform nonlinear optical spectroscopy experiments an entire new laser setup was built up from the scratch. This experimental setup consists of an high-power Yb:KGW solitary mode-locked oscillator [63, 81], of a nonlinear photonic crystal fiber for spectral broadening, of a prism sequence for pulse compression and a 4f Fourier transform pulse shaper for amplitude and phase modulation. Altogether this setup allows for the generation of widely tunable ultrashort laser pulses, which constitute an ideal light source for nonlinear optical experiments on plasmonic nanostructures [107].

In the nonlinear optical experiments we predominantly investigated the second and third harmonic (TH) response of complex plasmonic nanostructure arrays. In particular, in TH spectroscopy experiments of gold rod-type nanoantenna arrays we found that the fundamental plasmon resonance in metal nanoantennas drives and enhances the nonlinear light generation. The TH generation efficiency peaks at the same spectral position as the plasmonic near-field, which is slightly red-shifted with respect to the plasmonic far-field, due to the damped nature of the plasmonic oscillators [109, 113, 172].

Experiments on two orthogonally coupled plasmonic oscillators revealed that a classical anharmonic coupled oscillator model is capable to describe and predict all features of the linear and

the nonlinear TH response of such complex plasmonic nanostructure arrays. Therefore, this model paved the way for designing complex plasmonic structures, which allow for further enhanced conversion efficiencies in nonlinear optical effects.

In order to tailor and boost the nonlinear optical response of plasmonic nanostructures we investigated the linear and the TH response of dolmen-type plasmonic nanostructure arrays, which exhibit plasmonic Fano resonances. The Fano resonance is the result of the coupling or the interference of bright and dark modes and the higher lifetime of the latter can lead to longer stored energy in the entire nanostructure system. Therefore, enhanced nonlinear light generation can be possible, however, only for systems where the difference in the lifetimes of the two modes is high enough, so that energy can efficiently be transferred back to the bright mode, where the TH is generated. In our particular purely gold dolmen-type nanostructures the difference in the lifetimes is on the order of two, which unfortunately did not yet lead to further enhanced TH generation when compared to the TH generation of isolated bright dipole antennas. However, a factor of four to five between the lifetimes indeed should allow for further enhanced conversion efficiencies in nonlinear optical effects, which could be achieved by coupling other systems with intrinsically long lifetimes to the bright dipole antennas. Furthermore, we found that the TH near-field polarization, which is generated in the dark mode, interferes destructively in the far-field due to the anti-symmetric charge oscillations of the dark mode at the fundamental laser wavelength [174].

Beyond that, we investigated the enhancement of TH generation in dielectric materials boosted by the intense electric near-field of plasmonic nanoantennas. Therefore, we incorporated nonlinear indium tin oxide (ITO) nanocrystals into the hot-spot of plasmonic gap-antennas and studied the TH response of corresponding hybrid ITO nanocrystal-incorporated plasmonic gap-antenna arrays. We observed an enhancement of the TH signals radiated from the hybrid gap-antenna arrays by about a factor

of two when comparing them to the TH signals of identical bare plasmonic gap-antenna arrays. A close study revealed that the enhanced TH signal strength is mainly related to changes in the linear optical properties of the respective antenna arrays. Furthermore, the TH signal is found to be nearly exclusively generated in the gold volume and not inside the ITO nanocrystals, which is directly related to the higher *linear* polarizability and the higher third-order susceptibility of gold when compared to that of ITO [196].

Finally, we developed a new SH measurement technique for measuring the SH response over a broad spectral range, in principle by a single laser shot, utilizing ultrabroadband strongly chirped laser pulses. Thereby, we were able to measure the spectrally-resolved SH response of various metal films in the near-infrared.

The above experiments showed that the origin of the TH response in plasmonic nanostructures is predominantly located in the metal rather than in any dielectric environment [114, 131]. Furthermore, in our spectral range it is most likely not a nonlinear oscillation of the localized surface plasmon which leads to the TH generation, but it is the bare metal nonlinearity, which is driven and enhanced by the plasmonic near-field polarization.

While the origin for TH generation in plasmonic nanostructures is therefore known quite well, for other nonlinear optical processes like for example second harmonic (SH) generation this is still under discussion. In principle SH generation should be forbidden for dipole nanoantennas, due to the symmetry of the nanostructures [16, 127]. However, in section 4.1 we observed a distinct SH signal from inversion symmetric plasmonic dipole nanoantennas, although it is much weaker than the radiated TH. An explanation for the generated SH signals could be the surface of the metal nanostructures, which locally breaks the inversion symmetry and therefore allows for the generation of SH light [55]. Furthermore, non-inversion symmetric plasmonic nanos-

structures like for example split ring resonators have been shown to exhibit a quite high SH response [45, 126, 162, 171, 197], which indicates that the spatial plasmonic field distribution can influence and contribute to the overall SH signal. Also chiral plasmonic nanostructures are believed to feature a high second order response, due to their inherent broken inversion symmetry [198–200].

In the future, the combination of doubly resonant plasmonic nanostructures might further boost the nonlinear signal generation [118]. The main idea is that the structures become resonant not only at the fundamental laser wavelength but also at the wavelength of the nonlinear signal [116, 117]. In particular, this concept could be promising for nonlinear optical effects where the nonlinear signal is located in the near or far infrared, where plasmonics perform superb and are not hampered by absorption losses in the metals like in the visible. Therefore, nonlinear four wave mixing or difference frequency generation enhanced by plasmonic nanostructures might be worth studying in detail.

Finally, the combination of plasmonic nanostructures with other nonlinear optical materials is still very promising. The strong electric near-fields of plasmonic nanoantennas might boost the efficiency of nonlinear effects in nanoscale volumes. Promising materials for such experiments are probably highly nonlinear materials like semiconductors or polymers [16].

APPENDIX

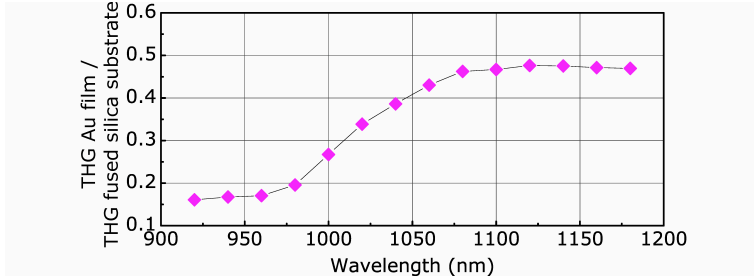


Figure A1: Measured TH intensities of a 20 nm thick plain gold film divided by the measured TH intensities of a fused silica substrate as a function of the excitation wavelength.

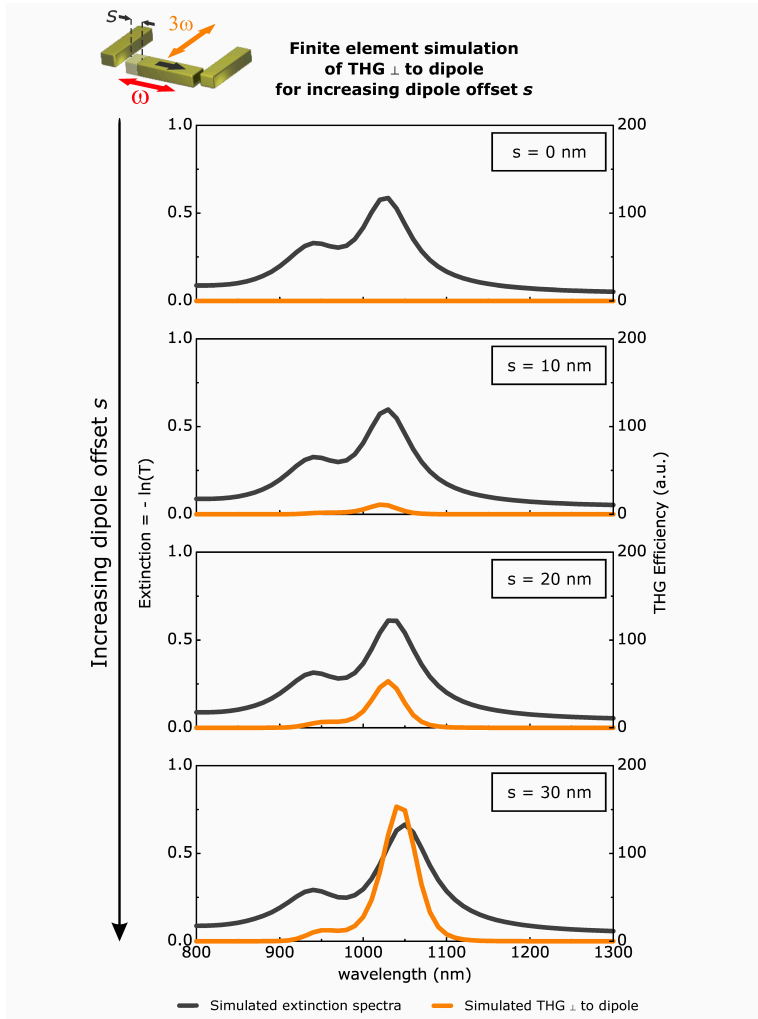


Figure A2: Simulated TH spectra polarized perpendicular to the dipole antenna for increasing dipole offset s from top to bottom.

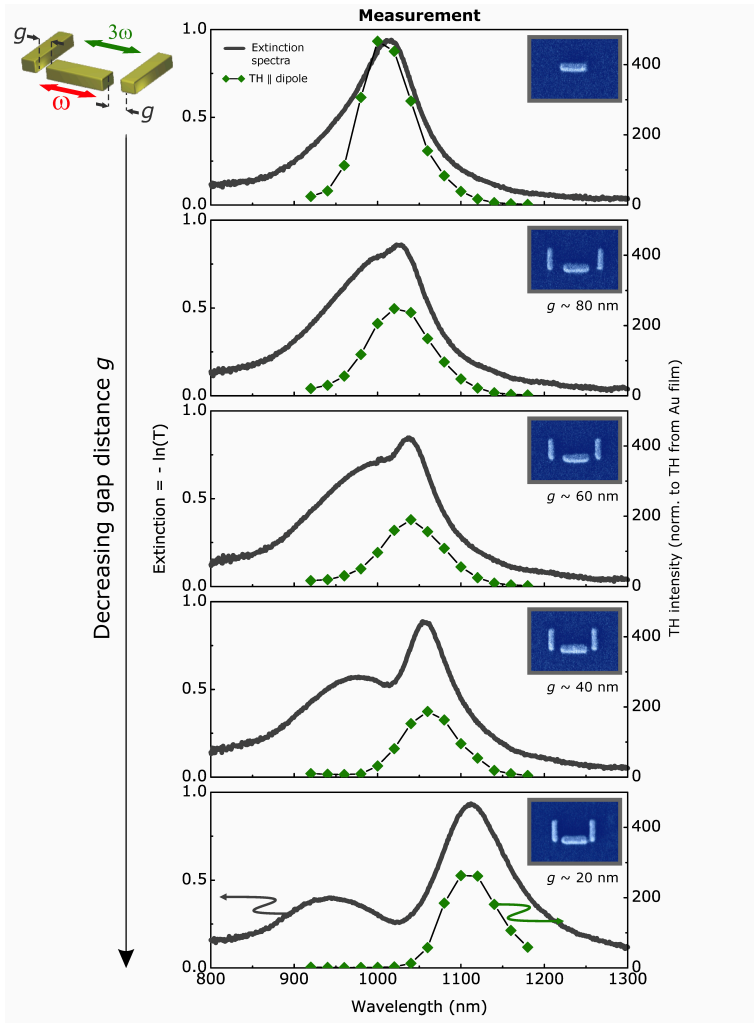


Figure A3: Measured TH spectra plotted together with their corresponding linear extinction spectra for decreasing gap distance g from top to bottom from a second dolmen-type nanostructure sample. The geometrical parameters are identical to the sample from section 4.3, but here the gap distance g has been tuned over a larger range. Furthermore, for comparison we also fabricated and measured a pure dipole antenna array on the same sample. It can be clearly seen that the plasmonic dipole antenna is most efficient for TH generation. For decreasing gap distance the maximum TH intensity decreases monotonically. For the smallest gap distance the Fano resonance already evolves into two hybridized normal modes. Here, the lower energy mode becomes more dipole like again and hence the TH efficiency increases slightly, but still remains below the TH intensity of the dipole antenna.

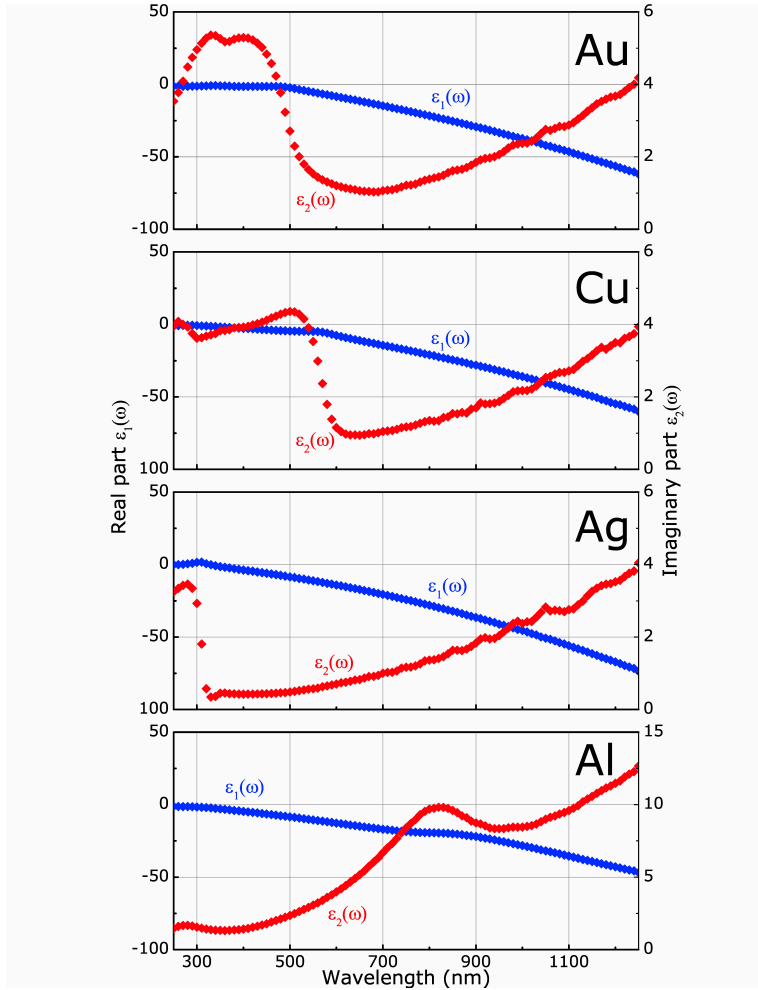


Figure A4: Measured dielectric constants by ellipsometry of 100 nm thick bare metal films of the metals gold, copper, silver and aluminum [201].

ACRONYMS

BBO	beta barium borate
CCD	charge coupled device
CW	continuous wave
DFG	difference frequency generation
DM	dichroic mirror
ESM	endlessly single mode
FEM	finite element method
FROG	frequency resolved optical gating
FWHM	full width half maximum
FWM	four wave mixing
GD	group delay
GDD	group delay dispersion
GNLSE	generalized nonlinear schrödinger equation
GTI	Gires Tournois interferometer
IAC	interferometric autocorrelation
ITO	indium tin oxide
LC	liquid crystal

- LCD** liquid crystal display
- LD** laser diode
- LMA** large mode area
- LSPR** localized surface plasmon resonance
- MIIPS** multiphoton intrapulse interference phase scan
- OA** optical axis
- OC** output coupler
- OR** optical rectification
- OPA** optical parametric amplifier
- OPO** optical parametric oscillator
- PCF** photonic crystal fiber
- PMMA** Poly(methyl methacrylate)
- PS-IFROG** pulse shaper assisted interferometric frequency resolved optical gating
- SEM** scanning electron micrograph
- SESAM** semiconductor saturable absorber mirror
- SFG** sum frequency generation
- SH** second harmonic
- SHG** second harmonic generation
- SLM** spatial light modulator
- SMF** single mode fiber

SPIDER spectral phase interferometry for direct electric field reconstruction

SPM self phase modulation

SRR split ring resonator

TBP time bandwidth product

TH third harmonic

THG third harmonic generation

UCP Ultrabroadband chirped pulse

XFROG cross-correlation frequency resolved optical gating

ZDW zero dispersion wavelength

BIBLIOGRAPHY

- [1] R. Fettiplace and C. M. Hackney, "The sensory and motor roles of auditory hair cells," *Nat. Rev. Neurosci.* **7**, 19 (2006).
- [2] W. Demtröder, *Experimentalphysik2: Elektrizität und Optik* (Springer, 2009), 5th edn.
- [3] W. Demtröder, *Experimentalphysik3: Atome, Moleküle und Festkörper* (Springer, 2010), 4th edn.
- [4] H. Haken and H. C. Wolf, *Molekülphysik und Quantenchemie* (Springer, 2006), 5th edn.
- [5] W. Demtröder, *Experimentalphysik4: Kern-, Teilchen- und Astrophysik* (Springer, 2005), 2th edn.
- [6] S. A. Maier, *Plasmonics: Fundamentals and Applications* (Springer, 2007).
- [7] C. F. Bohren and D. R. Huffman, *Absorption and Scattering of Light by Small Particles* (Wiley-Interscience Publication, 1998).
- [8] U. Kreibig and M. Vollmer, *Optical Properties of Metal Clusters* (Springer, 1995).
- [9] L. Novotny and B. Hecht, *Principles of Nano-Optics* (Cambridge University Press, 2006).
- [10] S. A. Maier, "Plasmonic field enhancement and SERS in the effective mode volume picture," *Opt. Express* **14**, 1957 (2006).

- [11] J. A. Schuller, E. S. Barnard, W. Cai, Y. C. Jun, J. S. White, and M. L. Brongersma, "Plasmonics for extreme light concentration and manipulation," *Nat. Mater.* **9**, 193 (2010).
- [12] N. Liu, M. L. Tang, M. Hentschel, H. Giessen, and A. P. Alivisatos, "Nanoantenna-enhanced gas sensing in a single tailored nanofocus," *Nat. Mater.* **10**, 631 (2011).
- [13] L.-W. Nien, S.-C. Lin, B.-K. Chao, M.-J. Chen, J.-H. Li, and C.-H. Hsueh, "Giant Electric Field Enhancement and Localized Surface Plasmon Resonance by Optimizing Contour Bowtie Nanoantennas," *J. Phys. Chem. C* **117**, 25 004 (2013).
- [14] W. L. Barnes, A. Dereux, and T. W. Ebbesen, "Surface plasmon subwavelength optics," *Nature* **424**, 824 (2003).
- [15] T. H. Maiman, "Stimulated Optical Radiation in Ruby," *Nature* **187**, 493 (1960).
- [16] R. W. Boyd, *Nonlinear Optics* (Academic Press, Elsevier, 2008), 3rd edn.
- [17] G. P. Agrawal, *Nonlinear Fiber Optics* (Academic Press, 2007), 4th edn.
- [18] P. A. Franken, A. E. Hill, C. W. Peters, and G. Weinrich, "Generation of Optical Harmonics," *Phys. Rev. Lett.* **7**, 118 (1961).
- [19] G. Krauss, S. Lohss, T. Hanke, A. Sell, S. Eggert, R. Huber, and A. Leitenstorfer, "Synthesis of a single cycle of light with compact erbium-doped fibre technology," *Nature Photon.* **4**, 33 (2010).
- [20] S. Rausch, T. Binhammer, A. Harth, J. Kim, R. Ell, F. X. Kärtner, and U. Morgner, "Controlled waveforms on the single-cycle scale from a femtosecond oscillator," *Opt. Express* **16**, 9739 (2008).

- [21] E. Goulielmakis, M. Schultze, M. Hofstetter, V. S. Yakovlev, J. Gagnon, M. Uiberacker, A. L. Aquila, E. M. Gullikson, D. T. Attwood, R. Kienberger, F. Krausz, and U. K. and, "Single-Cycle Nonlinear Optics," *Science* **320**, 1614 (2008).
- [22] K. Zhao, Q. Zhang, M. Chini, Y. Wu, X. Wang, and Z. Chang, "Tailoring a 67 attosecond pulse through advantageous phase-mismatch," *Opt. Express* **37**, 3891 (2012).
- [23] www.nobelprize.org/nobelprizes/chemistry/laureates/1999.
- [24] I. N. Bronstein, K. A. Semendjajew, G. Musiol, and H. Mühlig, *Taschenbuch der Mathematik* (Wissenschaftlicher Verlag Harri Deutsch GmbH, 2005).
- [25] C. Cohen-Tannoudji, B. Diu, and F. Laloë, *Quantenmechanik 2* (Walter de Gruyter, 1999), 2nd edn.
- [26] W. Nolting, *Grundkurs Theoretische Physik 3: Elektrodynamik* (Springer, 2007), 8th edn.
- [27] R. Taubert, *From Near-Field to Far-Field: Plasmonic Coupling in Three-Dimensional Nanostructures*, Ph.D. thesis (2012).
- [28] P. B. Johnson and R. W. Christy, "Optical Constants of the Noble Metals," *Phys. Rev. B* **6**, 4370 (1972).
- [29] C. Sönnichsen, *Plasmons in metal nanostructures*, Ph.D. thesis (2001).
- [30] M. I. Stockman, "Nanoplasmonics: past, present, and glimpse into future," *Opt. Express* **19**, 22 029 (2011).
- [31] K. L. Kelly, E. Coronado, L. L. Zhao, and G. C. Schatz, "The Optical Properties of Metal Nanoparticles: The Influence of Size, Shape, and Dielectric Environment," *J. Phys. Chem. B* **107**, 668 (2003).
- [32] G. Mie, "Beiträge zur Optik trüber Medien, speziell kolloidaler Metalllösungen," *Annalen der Physik* **330**, 377 (1908).

- [33] J. D. Jackson, *Classical Electrodynamics* (John Wiley and Sons, Inc., 1999), 3rd edn.
- [34] L. Novotny, "Effective Wavelength Scaling for Optical Antennas," *Phys. Rev. Lett.* **98**, 266 802 (2007).
- [35] C. Sönnichsen, T. Franzl, T. Wilk, G. von Plessen, J. Feldmann, O. Wilson, and P. Mulvaney, "Drastic reduction of plasmon damping in gold nanorods," *Phys. Rev. Lett.* **88**, 077 402 (2002).
- [36] E. Prodan, C. Radloff, N. J. Halas, and P. Nordlander, "A Hybridization Model for the Plasmon Response of Complex Nanostructures," *Science* **302**, 419 (2003).
- [37] P. Nordlander and C. Oubre, "Plasmon Hybridization in Nanoparticle Dimers," *Nano Lett.* **4**, 899 (2004).
- [38] W. Rechberger, A. Hohenau, A. Leitner, J. R. Krenn, B. Lamprecht, and F. R. Aussenegg, "Optical properties of two interacting gold nanoparticles," *Opt. Comm.* **220**, 137 (2003).
- [39] N. Liu and H. Giessen, "Coupling Effects in Optical Metamaterials," *Angewandte Chemie* **49**, 9838 (2010).
- [40] D. R. Smith, J. B. Pendry, and M. C. K. Wiltshire, "Metamaterials and Negative Refractive Index," *Science* **305**, 788 (2004).
- [41] A. Sihvola, "Metamaterials in electromagnetics," *ScienceDirect* **1**, 2 (2007).
- [42] C. Rockstuhl, F. Lederer, C. Etrich, T. Zentgraf, J. Kuhl, and H. Giessen, "On the reinterpretation of resonances in split-ring-resonators at normal incidence," *Opt. Express* **14**, 8827 (2006).
- [43] M. Husnik, M. Klein, N. Feth, M. König, J. Niegemann, K. Busch, S. Linden, and M. Wegener, "Absolute extinction cross-section of individual magnetic split-ring resonators," *Nature Photon.* **2**, 614 (2008).

- [44] N. Liu, H. Guo, L. Fu, S. Kaiser, H. Schweizer, and H. Giessen, "Three-dimensional photonic metamaterials at optical frequencies," *Nat. Mater.* **7**, 31 (2008).
- [45] H. L. Na Liu and, S. Zhu, and H. Giessen, "Stereometamaterials," *Nature Photon.* **3**, 157 (2009).
- [46] S. Linden, C. Enkrich, M. Wegener, T. K. J. Zhou, and C. M. Soukoulis, "Magnetic Response of Metamaterials at 100 Terahertz," *Science* **306**, 1351 (2004).
- [47] D. R. Smith, W. J. Padilla, D. C. Vier, S. C. Nemat-Nasser, and S. Schultz, "Composite Medium with Simultaneously Negative Permeability and Permittivity," *Phys. Rev. Lett.* **84**, 4184 (1999).
- [48] J. Valentine, S. Zhang, T. Zentgraf, E. Ulin-Avila, D. A. Genov, G. Bartal, and X. Zhang, "Three-dimensional optical metamaterial with a negative refractive index," *Nature* **445**, 376 (2008).
- [49] J. B. Pendry, "Negative Refraction Makes a Perfect Lens," *Phys. Rev. Lett.* **85**, 3966 (2000).
- [50] R. A. Shelby, D. R. Smith, and S. Schultz, "Experimental Verification of a Negative Index of Refraction," *Science* **292**, 77 (2001).
- [51] V. M. Shalaev, "Optical negative-index metamaterials," *Nat. Photon.* **1**, 41 (2007).
- [52] C. M. Soukoulis, S. Linden, and M. Wegener, "Negative Refractive Index at Optical Wavelengths," *Science* **315**, 47 (2007).
- [53] R. R. Birss, *Symmetry and Magnetism* (North-Holland Publishing Co., Amsterdam, 1966).
- [54] J.-P. Negel, R. Hegenbarth, A. Steinmann, B. Metzger, F. Hoos, and H. Giessen, "Compact and cost-effective

- scheme for THz generation via optical rectification in GaP and GaAs using novel fs laser oscillators," *Appl. Phys. B* **103**, 45 (2011).
- [55] J. E. Sipe, D. J. Moss, and H. M. van Driel, "Phenomenological theory of optical second- and third-harmonic generation from cubic centrosymmetric crystals," *Phys. Rev. B* **35**, 1129 (1987).
- [56] R. Fischer and L. A. Kulevskii, "Optical parametric oscillators," *Sov. J. Quantum Electron.* **7**, 135 (1997).
- [57] M. H. Dunn and M. Ebrahimzadeh, "Parametric Generation of Tunable Light from Continuous-Wave to Femtosecond Pulses," *Science* **286**, 1513 (1999).
- [58] D. T. Reid, J. Sun, T. P. Lamour, and T. I. FERREIRO, "Advances in ultrafast optical parametric oscillators," *Laser Phys. Lett.* (2011).
- [59] R. Hegenbarth, A. Steinmann, G. Toth, J. Hebling, and H. Giessen, "Two-color femtosecond optical parametric oscillator with 1.7 W output pumped by a 7.4 W Yb:KGW laser," *J. Opt. Soc. Am. B* **28**, 1344 (2011).
- [60] G. Cerullo and S. D. Silvestri, "Ultrafast optical parametric amplifiers," *Rev. Sci. Instrum.* **74**, 1 (2003).
- [61] M. Bradler, C. Homann, and E. Riedle, "Broadband difference frequency mixing between visible and near-infrared pulses for few-cycle pulse generation with stable carrier-envelope phase," *Appl. Phys. B* **113**, 19 (2013).
- [62] J. Krauth, A. Steinmann, R. Hegenbarth, M. Conforti, and H. Giessen, "Broadly tunable femtosecond near- and mid-IR source by direct pumping of an OPA with a 7.4 W Yb:KGW oscillator," *Opt. Express* **21**, 11 516 (2013).
- [63] F. Hoos, T. P. Meyrath, S. Li, B. Braun, and H. Giessen, "Femtosecond 5-W Yb:KGW slab laser oscillator pumped

- by a single broad-area diode and its application as supercontinuum source," *Appl. Phys. B* **96**, 5 (2009).
- [64] A. Steinmann, B. Metzger, R. Hegenbarth, and H. Giessen, "Compact 7.4 W femtosecond oscillator for white-light generation and nonlinear microscopy," Talk CThAA5S, CLEO/QELS, Baltimore (USA) (2011).
- [65] U. K. et al., "Semiconductor saturable absorber mirrors (SESAMs) for femtosecond to nanosecond pulse generation in solid-state lasers," *IEEE J. Sel. Top. Quantum Electron.* **2**, 435 (1996).
- [66] P. Crump, G. Blume, K. Paschke, R. Staske, A. Pietrzak, U. Zeimer, S. Einfeldt, A. Ginolas, F. Bugge, K. Häusler, P. Ressel, H. Wenzel, and G. Erbert, "20 W continuous wave reliable operation of 980nm broad-area single emitter diode lasers with an aperture of 96 μm ," *Proc. SPIE* **7198**, 719814 (2009).
- [67] F. Gires and P. Tournois, "Interferometre utilisable pour la compression d'impulsions lumineuses modulées en fréquence," *C. R. Acad. Sci. Paris* **258**, 6112 (1964).
- [68] G. P. Agrawal, *Fiber-optic communication systems* (John Wiley and Sons, Inc., New York, 2002), 3rd edn.
- [69] D. Meschede, *Optik, Licht und Laser* (Vieweg + Teubner, Wiesbaden, 2008), 3th edn.
- [70] P. Russell, "Photonic Crystal Fibers," *Science* **299**, 358 (2003).
- [71] J. M. Dudley, "Supercontinuum generation in photonic crystal fiber," *Rev. Mod. Phys.* **78**, 1135 (2006).
- [72] T. A. Birks and Y. W. Li, "The Shape of Fiber Tapers," *Journal of Lightwave Technol.* **10**, 432 (1992).
- [73] "<http://www.nktpotonics.com/files/files/LMA-8.pdf>," .

- [74] S. Pricking and H. Giessen, "Tapering fibers with complex shape," *Opt. Express* **18**, 3426 (2010).
- [75] S. Pricking and H. Giessen, "Tailoring the soliton and supercontinuum dynamics by engineering the profile of tapered fibers," *Opt. Express* **18**, 20 151 (2010).
- [76] A. Stiebeiner, R. Garcia-Fernandez, and A. Rauschenbeutel, "Design and optimization of broadband tapered optical fibers with a nanofiber waist," *Opt. Express* **18** (2010).
- [77] "<http://www.focenter.com/Fiber%20Optic%20Center%5Ccorning%5Cdatasheets%5Csmf-28.pdf>," .
- [78] S. Pricking, *Messung der Gruppengeschwindigkeitsdispersion von gezogenen Fasern*, Master's thesis (2004).
- [79] B. Metzger, *Breitbandige und durchstimmbare ultrakurze Hochleistungslaserpulse*, Master's thesis (2010).
- [80] S. Pricking, *Soliton Dynamics and Supercontinuum Generation in complex-shaped Tapered Fibers and liquid-filled Photonic Crystal Fibers*, Ph.D. thesis (2011).
- [81] B. Metzger, A. Steinmann, F. Hoos, S. Pricking, and H. Giessen, "Compact laser source for high-power white-light and widely tunable sub 65 fs laser pulses," *Opt. Lett.* **35**, 3961 (2010).
- [82] "Pictures by B. Metzger, 4th Physics Institute and Research Center SCoPE, University of Stuttgart, Germany," .
- [83] J.-C. Diels and W. Rudolph, *Ultrashort Laser Pulse Phenomena: Fundamentals, Techniques, and Applications on a Femtosecond Time Scale* (Academic Press, Elsevier, 2006), 2nd edn.
- [84] A. M. Heidt, J. Rothhardt, A. Hartung, H. Bartelt, E. G. Rohwer, J. Limpert, and A. Tünnerman, "High quality sub-two cycle pulses from compression of supercontinuum generated in all-normal dispersion photonic crystal fiber," *Opt. Express* **19**, 13 873 (2011).

- [85] S. Linden, H. Giessen, and J. Kuhl, "XFROG - A new method for amplitude and phase characterization of weak ultrashort pulses," *Phys. stat. sol. (b)* **206**, 119 (1998).
- [86] R. Trebino, K. W. DeLong, D. N. Fittinghoff, J. N. Sweetser, M. A. Krumbügel, and B. A. Richman, "Measuring Ultrashort Laser Pulses in the Time-Frequency Domain Using Frequency-Resolved Optical Gating," *Rev. Sci. Instrum.* **68**, 3277 (1997).
- [87] B. Schenkel, R. Paschotta, and U. Keller, "Pulse compression with supercontinuum generation in microstructure fiber," *J. Opt. Soc. Am. B* **22**, 687 (2005).
- [88] S. C. Buchter, M. Kaivola, H. Ludvigsen, and K. P. Hansen, "Miniature supercontinuum laser sources," Conference on Lasers and Electro-Optics/International Quantum Electronics Conference and Photonic Applications Systems Technologies, Technical Digest (CD) (OSA), paper CTuP58 (2004).
- [89] B. v. V. J. Möhring, T. Buckup and M. Motzkus, "Parametrically amplified ultrashort pulses from a shaped photonic crystal fiber supercontinuum," *Opt. Lett.* **33**, 186 (2008).
- [90] T. Südmeyer, F. Brunner, E. Innerhofer, R. Paschotta, K. Furusawa, J. C. Baggett, T. M. Monro, D. J. Richardson, and U. Keller, "Nonlinear femtosecond pulse compression at high average power levels by use of a large-mode-area holey fiber," *Opt. Lett.* **28**, 1951 (2003).
- [91] R. L. Fork, O. E. Martinez, and J. P. Gordon, "Negative dispersion using pairs of prisms," *Opt. Lett.* **9**, 150 (1984).
- [92] R. Trebino, *Frequency-Resolved Optical Gating: The Measurement of Ultrashort Laser Pulses* (Kluwer Academic Publishers, 2000).

- [93] A. M. Weiner, J. P. Heritage, and E. M. Kirschner, "High-resolution femtosecond pulse shaping," *J. Opt. Soc. Am. B* **5**, 1563 (1988).
- [94] A. M. Weiner, "Femtosecond pulse shaping using spatial light modulators," *Rev. Sci. Instrum.* **71**, 1929 (2000).
- [95] B. v. Vacano, W. Wohlleben, and M. Motzkus, "Actively shaped supercontinuum from a photonic crystal fiber for nonlinear coherent microspectroscopy," *Opt. Lett.* **31**, 413 (2006).
- [96] *SLM-S640d Technical Documentation* (Jenoptik Optical Systems, Jena, Germany, 2010).
- [97] G. Stobrawa, M. Hacker, T. Feurer, D. Zeidler, M. Motzkus, and F. Reichel, "A new high-resolution femtosecond pulse shaper," *Appl. Phys. B* **72**, 627 (2001).
- [98] T. Baumert, T. Brixner, V. Seyfried, M. Strehle, and G. Gerber, "Femtosecond pulse shaping by an evolutionary algorithm with feedback," *Appl. Phys. B* **65**, 779 (1997).
- [99] V. V. Lozovoy, I. Pastirk, and M. Dantus, "Multiphoton intrapulse interference. IV. Ultrashort laser pulse spectral phase characterization and compensation," *Opt. Lett.* **29**, 775 (2004).
- [100] B. Xu, J. M. Gunn, J. M. D. Cruz, V. V. Lozovoy, and M. Dantus, "Quantitative investigation of the multiphoton intrapulse interference phase scan method for simultaneous phase measurement and compensation of femtosecond laser pulses," *J. Opt. Soc. Am. B* **23**, 750 (2006).
- [101] B. Xu, Y. Coello, V. V. Lozovoy, D. A. Harris, and M. Dantus, "Pulse Shaping of octave spanning femtosecond laser pulses," *Opt. Express* **14**, 10 939 (2006).
- [102] C. Iaconis and I. A. Walmsley, "Spectral phase interferometry for direct electric field reconstruction of ultrashort optical pulses," *Opt. Lett.* **23**, 792 (1998).

- [103] N. Forget, V. Crozatier, and T. Oksenhendler, "Pulse-measurement techniques using a single amplitude and phase spectral shaper," *J. Opt. Soc. Am. B* **27**, 742 (2010).
- [104] G. Stibenz and G. Steinmeyer, "Interferometric frequency-resolved optical gating," *Opt. Express* **13**, 2617 (2005).
- [105] M. W. Klein, C. Enkrich, M. Wegener, and S. Linden, "Second-Harmonic Generation from Magnetic Metamaterials," *Science* **313**, 502 (2006).
- [106] M. Kauranen and A. V. Zayats, "Nonlinear plasmonics," *Nat. Photon.* **6**, 737 (2012).
- [107] B. Metzger, A. Steinmann, and H. Giessen, "High-power widely tunable sub-20 fs Gaussian laser pulses for ultrafast nonlinear spectroscopy," *Opt. Express* **19**, 24 354 (2011).
- [108] M. Hentschel, T. Utikal, H. Giessen, and M. Lippitz, "Quantitative Modelling of the Third Harmonic Emission Spectrum of Plasmonic Nanoantennas," *Nano. Lett.* **12**, 3778 (2012).
- [109] J. Zuloaga and P. Nordlander, "On the redshift of the plasmonic near-field with respect to the far-field spectrum," *Nano Lett.* **11**, 1280 (2011).
- [110] M. W. Klein, T. Tritschler, M. Wegener, and S. Linden, "Lineshape of harmonic generation by metallic nanoparticles and metallic photonic crystal slabs," *Phys. Rev. B* **72**, 115 113 (2005).
- [111] R. P. Feynman, R. B. Leighton, and M. Sands, *The Feynman Lectures on Physics, vol. 1* (Addison-Wesley, 1997, 2007), formula 30.19.
- [112] B. Lamprecht, J. Krenn, A. Leitner, and F. Aussenegg, "Particle-plasmon decay-time determination by measuring the optical near-field's autocorrelation: influence of inhomogeneous line broadening," *Appl. Phys. B* **69**, 223 (1999).

- [113] B. Metzger, M. Hentschel, M. Lippitz, and H. Giessen, "Third-harmonic spectroscopy and modeling of the non-linear response of plasmonic nanoantennas," *Opt. Lett.* **37**, 4741 (2012).
- [114] T. Utikal, T. Zentgraf, T. Paul, C. Rockstuhl, F. Lederer, M. Lippitz, and H. Giessen, "Towards the origin of the non-linear response in hybrid plasmonic systems," *Phys. Rev. Lett.* **106**, 133 901 (2011).
- [115] R. Feynman, R. B. Leighton, and M. Sands, *Feynman Lectures on Physics Volume 1* (Addison-Wesley, 1977), formula 30.19.
- [116] K. Thyagarajan, S. Rivier, A. Lovera, and O. J. F. Martin, "Enhanced second-harmonic generation from double resonant plasmonic antennae," *Opt. Express* **20**, 12 860 (2012).
- [117] H. Aouani, M. Navarro-Cia, M. Rahmani, T. P. H. Sidiropoulos, M. Hong, R. F. Oulton, and S. A. Maier, "Multiresonant Broadband Optical Antennas As Efficient Tunable Nanosources of Second Harmonic Light," *Nano Lett.* **12**, 4997 (2012).
- [118] H. Harutyunyan, G. Volpe, R. Quidant, and L. Novotny, "Enhancing the Nonlinear Optical Response Using Multi-frequency Gold-Nanowire Antennas," *Phys. Rev. Lett.* **108**, 217 403 (2012).
- [119] M. Navarro-Cia and S. A. Maier, "Broad-Band Near-Infrared Plasmonic Nanoantennas for Higher Harmonic Generation," *ACS Nano* **6**, 3537 (2012).
- [120] K. Thyagarajan, J. Butet, and O. J. F. Martin, "Augmenting Second Harmonic Generation Using Fano Resonances in Plasmonic Systems," *Nano Lett.* **13**, 1847 (2013).
- [121] M. Abb, Y. Wang, P. Albella, C. H. de Groot, J. Aizpuru, and O. L. Muskens, "Nonlinear Control of High-Order

- Modes in Single Asymmetric Nanoantennas," *ACS Nano* **6**, 6462 (2012).
- [122] R. Zhang, Y. Zhang, Z. C. Dong, S. Jiang, C. Zhang, L. G. Chen, L. Zhang, Y. Liao, J. Aizpurua, Y. Luo, J. L. Yang, and J. G. Hou, "Chemical mapping of a single molecule by plasmon-enhanced Raman scattering," *Nature* **498**, 82 (2013).
- [123] B. Luk'yanchuk, N. I. Zheludev, S. A. Maier, N. J. Halas, P. Nordlander, H. Giessen, and C. T. Chong, "The Fano resonance in plasmonic nanostructures and metamaterials," *Nat. Mater.* **9**, 707 (2010).
- [124] M. I. Stockman, "Dark-hot resonances," *Nature* **467**, 541 (2010).
- [125] T. Hanke, J. Cesar, V. Knittel, A. Trügler, U. Hohenester, A. Leitenstorfer, and R. Bratschitsch, "Tailoring spatiotemporal light confinement in single plasmonic nanoantennas," *Nano Lett.* **12**, 992 (2012).
- [126] S. Linden, F. B. P. Niesler, J. Förstner, Y. Grynko, T. Meier, and M. Wegener, "Collective Effects in Second-Harmonic Generation from Split-Ring-Resonator Arrays," *Phys. Rev. Lett.* **109**, 1 (2012).
- [127] R. Czaplicki, H. Husu, R. Siikanen, J. Mäkitalo, M. Kauranen, J. Laukkanen, J. Lehtolahti, and M. Kuittinen, "Enhancement of Second-Harmonic Generation from Metal Nanoparticles by Passive Elements," *Phys. Rev. Lett.* **110**, 093 902 (2013).
- [128] E. Kim, F. Wang, W. Wu, Z. Yu, and Y. R. Shen, "Contribution of the electric quadrupole resonance in optical metamaterials," *Phys. Rev. B* **78**, 113 102 (2008).
- [129] S. Kujala, B. K. Canfield, M. Kauranen, Y. Svirko, and J. Turunen, "Multipole Interference in the Second-Harmonic

- Optical Radiation from Gold Nanoparticles," *Phys. Rev. Lett.* **98**, 167 403 (2007).
- [130] M. W. Klein, M. Wegener, N. Feth, and S. Linden, "Experiments on second- and third-harmonic generation from magnetic metamaterials," *Opt. Express* **15**, 5238 (2007).
- [131] M. Lippitz, M. A. van Dijk, and M. Orrit, "Third-Harmonic Generation from Single Gold Nanoparticles," *Nano Lett.* **5**, 799 (2005).
- [132] B. Gallinet and O. J. F. Martin, "Relation between near-field and far-field properties of plasmonic Fano resonances," *Opt. Express* **19**, 22 167 (2011).
- [133] S. Zhang, D. A. Genov, Y. Wang, M. Liu, and X. Zhang, "Plasmon-induced transparency in metamaterials," *Phys. Rev. Lett.* **101**, 047 401 (2008).
- [134] N. Liu, L. Langguth, T. Weiss, J. Kästel, M. Fleischhauer, T. Pfau, and H. Giessen, "Plasmonic analogue of electromagnetically induced transparency at the Drude damping limit," *Nat. Mater.* **8**, 758 (2009).
- [135] N. Liu, T. Weiss, M. Mesch, L. Langguth, U. Eigenthaler, M. Hirscher, C. Sönnichsen, and H. Giessen, "Planar Metamaterial Analogue of Electromagnetically Induced Transparency for Plasmonic Sensing," *Nano. Lett.* **10**, 1103 (2010).
- [136] R. W. Boyd, *Nonlinear Optics* (Academic Press, Elsevier, 2008), 3rd edn.
- [137] T. Utikal, T. Zentgraf, J. Kuhl, and H. Giessen, "Dynamics and dephasing of plasmon polaritons in metallic photonic crystal superlattices: Time- and frequency-resolved nonlinear autocorrelation measurements and simulation," *Phys. Rev. B* **76**, 245 107 (2007).

- [138] R. Taubert, M. Hentschel, J. Kästel, and H. Giessen, "Classical Analogue of Electromagnetically Induced Absorption in Plasmonics," *Nano Lett.* **12**, 1367 (2012).
- [139] P. B. Johnson and R. W. Christy, "Optical Constants of the Noble Metals," *Phys. Rev. B* **6**, 4370 (1972).
- [140] N. Bloembergen, W. K. Burns, and M. Matsuoka, "Reflected third harmonic generated by picosecond laser pulses," *Opt. Commun.* **1**, 195 (1969).
- [141] A. E. Schlather, N. Large, A. S. Urban, P. Nordlander, and N. J. Halas, "Near-Field Mediated Plexcitonic Coupling and Giant Rabi Splitting in Individual Metallic Dimers," *Nano Lett.* **13**, 3281 (2013).
- [142] J. Reinhold, M. R. Shcherbakov, A. Chipouline, V. I. Panov, C. Helgert, T. Paul, C. Rockstuhl, F. Lederer, E.-B. Kley, A. Tünnermann, A. A. Fedyanin, and T. Pertsch, "Contribution of the magnetic resonance to the third harmonic generation from a fishnet metamaterial," *Phys. Rev. B* **86**, 115401 (2012).
- [143] P. J. Campagnola and L. M. Loew, "Second-harmonic imaging microscopy for visualizing biomolecular arrays in cells, tissues and organisms," *Nat. Biotechnol.* **21**, 1356 (2003).
- [144] Y. Nakayama, P. J. Pauzauskie, A. Radenovic, R. M. Onorato, R. J. Saykally, J. Liphardt, and P. Yang, "Tunable nanowire nonlinear optical probe," *Nature* **447**, 1098 (2007).
- [145] C.-L. Hsieh, R. Grange, Y. Pu, and D. Psaltis, "Three-dimensional harmonic holographic microscopy using nanoparticles as probes for cell imaging," *Opt. Express* **17**, 2880 (2009).
- [146] A. P. Alivisatos, "The use of nanocrystals in biological detection," *Nat. Biotechnol.* **22**, 47 (2004).
- [147] A. P. Alivisatos, "Semiconductor Clusters, Nanocrystals, and Quantum Dots," *Science* **271**, 933 (2007).

- [148] B. Knabe, K. Buse, W. Assenmacher, and W. Mader, "Spontaneous polarization in ultrasmall lithium niobate nanocrystals revealed by second harmonic generation," *Phys. Rev. B* **86**, 195 428 (2012).
- [149] L. Novotny and N. van Hulst, "Antennas for light," *Nat. Photon.* **5**, 83 (2011).
- [150] N. J. Halas, S. Lal, W.-S. Chang, S. Link, and P. Nordlander, "Plasmons in strongly coupled metallic nanostructures," *Chemical Reviews* **111**, 3913 (2011).
- [151] V. Giannini, A. I. Fernández-Domínguez, S. C. Heck, and S. A. Maier, "Plasmonic Nanoantennas: Fundamentals and Their Use in Controlling the Radiative Properties of Nanoemitters," *Chemical Reviews* **111**, 3888 (2011).
- [152] Y. Zhang, N. K. Grady, C. Ayala-Orozco, and N. J. Halas, "Three-dimensional nanostructures as highly efficient generators of second harmonic light," *Nano Lett.* **11**, 5519 (2011).
- [153] B. K. Canfield, H. Husu, J. Laukkanen, B. Bai, M. Kuitinen, J. Turunen, and M. Kauranen, "Local field asymmetry drives second-harmonic generation in non-centrosymmetric nanodimers," *Nano Lett.* **7**, 1251 (2007).
- [154] T. Hanke, G. Krauss, D. Träutlein, B. Wild, R. Bratschitsch, and A. Leitenstorfer, "Efficient Nonlinear Light Emission of Single Gold Optical Antennas Driven by Few-Cycle Near-Infrared Pulses," *Phys. Rev. Lett.* **103**, 257 404 (2009).
- [155] M. Danckwerts and L. Novotny, "Optical Frequency Mixing at Coupled Gold Nanoparticles," *Phys. Rev. Lett.* **98**, 026 104 (2007).
- [156] P. Biagioni, D. Brida, J.-S. Huang, J. Kern, L. Duò, B. Hecht, M. Finazzi, and G. Cerullo, "Dynamics of four-photon photoluminescence in gold nanoantennas," *Nano Lett.* **12**, 2941 (2012).

- [157] J. B. Khurgin and G. Sun, "Plasmonic enhancement of the third order nonlinear optical phenomena: Figures of merit," *Opt. Express* **21**, 1062 (2013).
- [158] M. B. Raschke, S. Berweger, and J. M. Atkin, *Plasmonics: Theory and Applications* (Springer, 2014), chap. Ultrafast and Nonlinear Plasmon Dynamics.
- [159] S. Kim, J. Jin, Y.-J. Park, Y. Kim, and S.-W. Kim, "High-harmonic generation by resonant plasmon field enhancement," *Nature* **453**, 757 (2008).
- [160] M. Siviş, M. Duwe, B. Abel, and C. Ropers, "Nanostructure-enhanced atomic line emission," *Nature* **485**, E1 (2012).
- [161] N. Pfullmann, C. Waltermann, M. Noack, S. Rausch, T. Nagy, C. Reinhardt, M. Kovačev, V. Knittel, R. Bratschitsch, D. Akemeier, A. Hütten, L. Leitenstorfer, and U. Morgner, "Bow-tie nano-antenna assisted generation of extreme ultraviolet radiation," *New Journal of Physics* **15**, 093027 (2013).
- [162] F. B. P. Niesler, N. Feth, S. Linden, J. Niegemann, J. Gieseler, K. Busch, and M. Wegener, "Second-harmonic generation from split-ring resonators on a GaAs substrate," *Opt. Lett.* **34**, 1997 (2009).
- [163] P. Chen, C. Argyropoulos, and A. Alu, "Enhanced Nonlinearities Using Plasmonic Nanoantennas," *Nanophotonics* **1**, 221 (2012).
- [164] P.-Y. Chen and A. Alù, "Optical nanoantenna arrays loaded with nonlinear materials," *Phys. Rev. B* **82**, 235405 (2010).
- [165] M. Abb, P. Albella, J. Aizpurua, and O. L. Muskens, "All-optical control of a single plasmonic nanoantenna-ITO hybrid," *Nano Lett.* **11**, 2457 (2011).

- [166] N. Ueda, H. Kawazoe, Y. Watanabe, M. Takata, M. Yamane, and K. Kubodera, "Third order nonlinear optical susceptibilities of amorphous SnO_{2-x} thin films," *Appl. Phys. Lett.* **59**, 502 (1991).
- [167] P. Mühlischlegel, H.-J. Eisler, O. J. F. Martin, B. Hecht, and D. W. Pohl, "Resonant optical antennas," *Science* **308**, 1607 (2005).
- [168] C. T. Black, C. B. Murray, and R. L. Sandstrom, "Embedded Nanoparticle Films and Method for Their Formation in Selective Areas on a Surface," (2013).
- [169] M. Saboktakin, X. Ye, U. K. Chettiar, N. Engheta, C. B. Murray, and C. R. Kagan, "Plasmonic Enhancement of Nanophosphor Upconversion Luminescence in Au Nanohole Arrays," *ACS Nano* **7**, 7186 (2013).
- [170] S. Choi, K. M. Nam, B. K. Park, W. S. Seo, and J. T. Park, "Preparation and Optical Properties of Colloidal, Monodisperse, and Highly Crystalline ITO Nanoparticles," *Chem. Mater.* **20**, 2609 (2008).
- [171] F. B. P. Niesler, N. Feth, S. Linden, and M. Wegener, "Second-harmonic optical spectroscopy on splitting-resonator arrays," *Opt. Lett.* **36**, 1533 (2011).
- [172] P. Alonso-González, P. Albella, F. Neubrech, C. Huck, J. Chen, F. Golmar, F. Casanova, L. E. Hueso, A. Pucci, J. Aizpurua, and R. Hillenbrand, "Experimental Verification of the Spectral Shift between Near- and Far-Field Peak Intensities of Plasmonic Infrared Nanoantennas," *Phys. Rev. Lett.* **110**, 203902 (2013).
- [173] <http://refractiveindex.info>.
- [174] B. Metzger, T. Schumacher, M. Hentschel, M. Lippitz, and H. Giessen, "Third Harmonic Mechanism in Complex Plasmonic Fano Structures," *ACS Photonics* (2014).

- [175] H. Aouani, M. Rahmani, M. Navarro-Cía, and S. A. Maier, "Third-harmonic-upconversion enhancement from a single semiconductor nanoparticle coupled to a plasmonic antenna," *Nat. Nanotechnol.* **9**, 290 (2014).
- [176] Y. Zhang, F. Wen, Y.-R. Zhen, P. Nordlander, and N. J. Halas, "Coherent Fano resonances in a plasmonic nanocluster enhance optical four-wave mixing," *P. Natl. Acad. Sci. USA* **110**, 9215 (2013).
- [177] J.-C. Tinguely, I. Sow, C. Leiner, J. Grand, A. Hohenau, N. Felidj, J. Aubard, and J. R. Krenn, "Gold Nanoparticles for Plasmonic Biosensing: The Role of Metal Crystallinity and Nanoscale Roughness," *BioNanoScience* **1**, 128 (2011).
- [178] M. Gentile, M. Hentschel, R. Taubert, H. Guo, H. Giessen, and M. Fiebig, "Investigation of the nonlinear optical properties of metamaterials by second harmonic generation," *Appl. Phys. B* **105**, 149 (2011).
- [179] D. Dregely, R. Taubert, J. Dorfmueller, R. Vogelgesang, K. Kern, and H. Giessen, "3D optical Yagi-Uda nanoantenna-array," *Nat. Comm.* **2**, 267 (2011).
- [180] N. J. Greenfield, "Using circular dichroism spectra to estimate protein secondary structure," *Nat. Prot.* **1**, 2876 (2007).
- [181] J. I. Dadap and T. F. Heinz, "Second-Harmonic Spectroscopy," *Encyclopedia of Modern Optics*, Elsevier **5**, 134 (2004).
- [182] R. V. Pisarev, "Optical second-harmonic generation in magnetic garnet thin films," *J. Phys. C* **5**, 8621 (1993).
- [183] V. V. Pavlov, R. V. Pisarev, A. Kirilyuk, and T. Rasing, "Observation of a Transversal Nonlinear Magneto-Optical Effect in Thin Magnetic Garnet Films," *Phys. Rev. Lett.* **78**, 2004 (1997).

- [184] K. Klass, G. Mette, J. Gdde, M. Drr, and U. Hfer, "Second-harmonic microscopy for fluence-dependent investigation of laser-induced surface reactions," *Phys. Rev. B* **83**, 125 116 (2011).
- [185] I. Freund, M. Deutsch, and A. Sprecher, "Connective tissue polarity. Optical second-harmonic microscopy, crossed-beam summation, and small-angle scattering in rat-tail tendon," *Biophys. J.* **50**, 693 (1986).
- [186] D. Brida, S. Bonora, C. Manzoni, M. Marangoni, P. Villoresi, S. D. Silvestri, and G. Cerullo, "Generation of 8.5-fs pulses at 1.3 μm for ultrabroadband pump-probe spectroscopy," *Opt. Express* **17**, 12 510 (2009).
- [187] C. Matranga and P. Guyot-Sionnest, "Absolute intensity measurements of the optical second-harmonic response of metals from 0.9 to 2.5 eV," *J. Chem. Phys.* **115**, 9503 (2001).
- [188] E. K. L. Wong and G. L. Richmond, "Examination of the surface second harmonic response from noble metal surfaces at infrared wavelengths," *J. Chem. Phys.* **99**, 5500 (1993).
- [189] I. Snger, D. R. Yakovlev, B. Kaminski, R. V. Pisarev, V. V. Pavlov, and M. Bayer, "Orbital quantization of electronic states in a magnetic field as the origin of second-harmonic generation in diamagnetic semiconductors," *Phys. Rev. B* **74**, 165 208 (2006).
- [190] B. Metzger, L. Gui, and H. Giessen, "Ultrabroadband chirped pulse second-harmonic spectroscopy: measuring the frequency-dependent second-order response of different metal films," *Opt. Lett.* **39**, 5293 (2014).
- [191] T. Sdmeyer, F. Brunner, E. Innerhofer, R. Paschotta, K. Furusawa, J. C. Baggett, T. M. Monro, D. J. Richardson, and U. Keller, "Nonlinear femtosecond pulse compression at high average power levels by use of a large-mode-area holey fiber," *Opt. Lett.* **28**, 1951 (2003).

- [192] J.-C. Diels and W. Rudolph, *Ultrashort Laser Pulse Phenomena* (Academic, 2005).
- [193] R. L. Olmon, B. Slovick, T. W. Johnson, D. Shelton, S.-H. Oh, G. D. Boreman, and M. B. Raschke, "Optical dielectric function of gold," *Phys. Rev. B* **86**, 235 147 (2012).
- [194] G. Petrocelli, S. Martellucci, and R. Francini, "Wavelength Dependence of Second-Harmonic Generation at the Copper Surface," *Appl. Phys. A* **56**, 263 (1993).
- [195] C. M. Li, L. E. Urbach, and H. L. Dai, "Second-harmonic generation from a Ag(111) surface at the interband transition region: Role of the dielectric function," *Phys. Rev. B* **49**, 2104 (1994).
- [196] B. Metzger, M. Hentschel, T. Schumacher, M. Lippitz, X. Ye, C. B. Murray, B. Knabe, K. Buse, and H. Giessen, "Doubling the Efficiency of Third Harmonic Generation by Positioning ITO Nanocrystals into the Hot-Spot of Plasmonic Gap-Antennas," *Nano Lett.* (2014).
- [197] H. Husu, R. Siikanen, J. Mäkitalo, J. Lehtolahti, J. Laukkanen, M. Kuittinen, and M. Kauranen, "Metamaterials with Tailored Nonlinear Optical Response," *Nano Lett.* **12**, 673 (2012).
- [198] M. Hentschel, M. Schäferling, T. Weiss, N. Liu, and H. Giessen, "Three-Dimensional Chiral Plasmonic Oligomers," *Nano. Lett.* **12**, 2542 (2012).
- [199] X. Yin, M. Schäferling, B. Metzger, and H. Giessen, "Interpreting Chiral Nanophotonic Spectra: The Plasmonic Born-Kuhn Model," *Nano. Lett.* **13**, 6238 (2013).
- [200] M. J. Huttunen, G. Bautista, M. Decker, S. Linden, M. Wegener, and M. Kauranen, "Nonlinear chiral imaging of subwavelength-sized twisted-cross gold nanodimers," *Opt. Mater. Express* **1**, 46 (2011).

- [201] "Measured by S. De Zuani, 1st Physics Insitute, University of Stuttgart, Germany," .

ACKNOWLEDGEMENTS

Writing a thesis in physics is impossible without the help of many people. For all those who supported me during these years I am very grateful and I want to thank them here:

- Prof. Dr. Harald Giessen for hosting me in his great institute and for providing a fascinating research topic, which excited me over all the years of this thesis.
- Prof. Dr. Peter Michler for kindly agreeing to take over the position of the co-advisor.
- Prof Dr. Günter Wunner for chairing the examination committee.
- Prof. Dr. Heinz Schweizer and Prof. Dr. Markus Lippitz for stimulating discussions.
- Dr. Sebastian Pricking, Dr. Felix Hoos and Dr. Tobias Utikal for their support in particular in the first year of my thesis.
- Dr. Andy Steinmann, Dr. Robin Hegenbarth and Tobias Steinle for sharing their know how on lasers.
- Dr. Mario Hentschel for great teamwork, for introducing me to plasmonics, for many great and insightful discussions about linear and nonlinear plasmonics.
- Dr. Richard Taubert and Dominik Flöss for great discussions about harmonic oscillators.

- Dr. Thorsten Schumacher for his simulations on nonlinear plasmonics.
- Dr. Marius Vieweg for being a great office neighbour during the first years.
- Dr. Daniel Dregely and Dr. Jessie Chin for an ingenious trip through western USA.
- Timo Gissibl and Martin Mesch for having me sometimes as office neighbour.
- Martin Mesch und Martin Schäferling for all kind of support regarding technical computer stuff.
- Sven Hein for his support on Pov-Ray visualization.
- Dr. Frank Neubrech for discussions about plasmonics.
- Xinghui Yin for letting me contribute to her work on chiral plasmonics.
- Dr. Lili Gui for great teamwork on chirped pulse second harmonic spectroscopy experiments.
- Jaco Fuchs for the first nonlinear plasmonics experiments using a homebuilt OPA.
- Dr. Christine von Rekowski for all administrative affairs.
- Monika Ubl, Michael Kube and Ramon Walter for all technical stuff.
- Stefano De Zuani for the measurement of ellipsometric data.
- Ralf Kamella for being very helpful in all kind of mechanical construction issues.

- Finally the entire 4th Physics Institute for a great working atmosphere.
- Meinen Eltern Lisa und Erwin, sowie meiner Schwester Susie.
- Meiner Freundin Melanie und Ihrer Familie.

CURRICULUM VITAE

Personal data

Name Bernd Metzger
Day of birth 06.02.1984
Place of birth Stuttgart (Germany)
Citizenship german
Adress Mozartstr. 34
70734 Fellbach
Mail b.metzger@physik.
uni-stuttgart.de



Curriculum vitae

1990 - 1994 Primary school: Luginslandschule
1994 - 2003 Secondary school:
Wirtemberg-Gymnasium in Stuttgart
2003 - 2004 Military service:
Gebirgsartilleriebataillon 225
Allgäu-Kaserne Füssen
2004 - 2010 Studies of physics:
University of Stuttgart
Elective subjects: *Astronomy and astrophysics,
theory of general relativity*
2009 - 2010 Diploma thesis: *High-power broadband
and tunable ultrashort laser pulses.*
Academic advisor: Prof. Dr. Harald Giessen
2010 - 2014 Ph.D. thesis: *Ultrafast Nonlinear Plasmonics:
From Dipole Nanoantennas to Hybrid Complex
Plasmonic Structures.*
Academic advisor: Prof. Dr. Harald Giessen

COLOPHON

This thesis was typeset using the typographical look-and-feel classicthesis developed by André Miede. The style was inspired by Robert Bringhurst's seminal book on typography "*The Elements of Typographic Style*". classicthesis is available for L^AT_EX via CTAN.